OPTIMIZATION OF LIGHTWEIGHT 3D-PRINTED UAV STRUCTURES USING GENERATIVE DESIGN AND MATERIAL ALTERNATIVES FOR ENHANCING PAYLOAD CAPACITY

A Thesis

by

DARREN ESPINOZA

Submitted in Partial Fulfillment of the

Requirements for the Degree of

MASTER OF SCIENCE IN ENGINEERING

Major Subject: Mechanical Engineering

The University of Texas Rio Grande Valley
August 2026

OPTIMIZATION OF LIGHTWEIGHT 3D-PRINTED UAV STRUCTURES USING GENERATIVE DESIGN AND MATERIAL ALTERNATIVES FOR ENHANCING PAYLOAD CAPACITY

A Thesis
by
DARREN ESPINOZA

COMMITTEE MEMBERS

Dr. Constantine Tarawneh
Chair of Committee

Dr. Farid Ahmed
Committee Member

Dr. Jinwoo An
Committee Member

Dr. Arturo Fuentes
Committee Member

August 2026

ABSTRACT

Espinoza, Darren, Optimization of Lightweight 3D-Printed UAV Structures Using Generative Design and Material Alternatives for Enhancing Payload Capacity. Master of Science in Engineering (MSE), August 2026, 118 pp., 27 tables, 62 figures, 47 references.

The research presented in this thesis examines the use of generative design and additive manufacturing as a method for producing lightweight components for a close-range infrastructure inspection hexacopter. Commercial thermoplastic and carbon-fiber-reinforced filaments were characterized through tensile, compression, and torsion testing under selected manufacturing conditions. PAHT-CF exhibited the most favorable strength and stiffness at low infill (20%) and was selected for structural evaluation. Generative design and finite element analysis were used to develop and evaluate arms and landing gear while considering mass, stress, displacement, and factor of safety. Experimental arm-deflection measurements supported the trends predicted by the numerical models, and propulsion testing identified motor-propeller configurations capable of producing a thrust-to-weight ratio of 2.53 for an assembled UAV. Flight testing demonstrated successful takeoff and hovering using generatively designed PETG arms.

DEDICATION

I dedicate this thesis to my mother, Silvana Espinoza, whose patience and support have carried me from childhood through adulthood, and to my father, Juan Espinoza, who has been both a father and a best friend.

ACKNOWLEDGEMENTS

I would like to thank those at the UTCRS and CREST who I would call friends and have gotten to know through my time at the University of Texas Rio Grande Valley.

I would like to acknowledge funding provided by the National Science Foundation CREST Center for Multidisciplinary Research Excellence in Cyber-Physical Infrastructure Systems under NSF Award No. 2112650

I would also like to acknowledge several people who have helped me solve issues related to this project, such as Dr. Robert Jones, Dr. Gasser Ali, and Mr. Marcos Villarreal

Lastly, to Dr. Constantine Tarawneh, I would like to acknowledge that you do have everyone's future in mind without much benefit to yourself. I do not believe there is another faculty member out there who goes beyond their own time to help people out. I am also grateful to Dr. Jazmin Ley and Joseph Montalvo for the help provided during my master's at UTRGV.

DISCLAIMER

The contents of this thesis reflect the views of the authors who are responsible for the facts and the accuracy of the information presented herein. This document is disseminated under the sponsorship of the National Science Foundation, in the interest of information exchange. The National Science Foundation assumes no liability for the contents or use thereof.

TABLE OF CONTENTS

LIST OF TABLES

LIST OF FIGURES

Page

CHAPTER I

INTRODUCTION & BACKGROUND

1.1 Introduction to Unmanned Aerial Vehicles

Public infrastructure, including roads, bridges, and pipelines, is critical to public welfare and economic stability. Figure 1 illustrates bridge cracking, a form of structural degradation that can reduce structural integrity and lead to fracture when crack-tip stresses exceed the fracture resistance of the material [1]. Conventional inspection methods may require personnel to access elevated or hazardous areas, increasing cost, labor requirements, and inspection time. These limitations create a need for safer, more efficient inspection systems.

Drones, or unmanned aerial vehicles (UAVs), operate without an onboard human pilot and are widely used for applications such as military surveillance, reconnaissance, and combat operations [2]. UAVs are generally classified as fixed-wing, rotary-wing, or hybrid vertical-takeoff-and-landing (VTOL) aircraft. Multirotor UAVs, such as quadcopters and hexacopters, are common rotary-wing configurations. Each configuration has distinct advantages and limitations in terms of payload capacity, flight time, hovering capability, stability, and cost [3]. Therefore, selecting an appropriate UAV configuration depends on the specific operational requirements of the application. Their ability to provide stable

, close-range aerial access to difficult-to-reach areas makes UAVs particularly suitable for bridge crack inspection, enabling efficient visual data collection while reducing the need for direct human access.

UAVs can operate at different altitudes and carry application-specific sensors, reducing workload, operating costs, and task duration in numerous industries [4]. Reported applications include pest control [5], fire suppression [6], forest monitoring [7], and air-conditioning dust inspection [8]. Multirotor UAVs are particularly suitable for infrastructure inspection because they can take off vertically, hover near structures, and maneuver at low speeds [3].

Figure 1: Bridge crack illustrating structural degradation - [9]

For example, a fixed-wing UAV, depicted in Figure 2, resembles a conventional airplane and generates lift through the forward motion of air over its rigid wings [3]. Compared with multirotor UAVs, fixed-wing UAVs generally offer longer flight times, higher flight speeds, and lower energy consumption during forward flight. Their relatively simple airframes can also accommodate substantial payloads. However, fixed-wing UAVs cannot hover and typically require a runway, launcher, or suitable open area for takeoff and landing [3]. These characteristics make them less suitable for close-range bridge crack inspection, where the UAV must maintain a stable position near the structure to capture detailed images.

Figure 2: Fixed-wing UAV [10]

VTOL UAVs combine the capabilities of fixed-wing and rotary-wing aircraft. They can take off and land vertically, hover when necessary, and transition to fixed-wing flight for more efficient forward travel [3]. This configuration provides the maneuverability and hovering capability of rotary-wing UAVs while offering improved flight endurance and energy efficiency during forward flight. However, VTOL UAVs generally require more complex mechanical components and advanced flight-control systems to manage the transition between flight modes [3]. They are also less commercially available than conventional fixed-wing and multirotor UAVs [3]. Since this research focuses on developing a simple and customizable UAV platform for close-range bridge inspection, the added complexity of a VTOL configuration was considered unnecessary. Therefore, a VTOL UAV was not selected for this work.

Multirotor UAVs generate lift through multiple motor-driven propellers, enabling vertical takeoff and landing, hovering, and precise maneuvering [3]. These capabilities allow them to operate close to structures without a runway, making them well suited for bridge crack inspection. They are also commercially available and can be customized to carry application-specific sensors and equipment. Although their relatively high energy consumption results in shorter flight times than fixed-wing UAVs [3], their maneuverability and adaptability make them the most appropriate configuration for this research.

1.2 Multirotor Configuration

The structural performance of a multirotor UAV is strongly influenced by its frame, which supports the propulsion system, electronic components, and payload while maintaining adequate strength and stiffness at minimal weight. In a review by Aswin et.al. [11], five quadcopter frame designs were modeled in CATIA and evaluated through structural and vibration analyses in ANSYS Workbench. The materials investigated included glass-fiber-reinforced polymer (GFRP), carbon-fiber-reinforced polymer (CFRP), Kevlar-fiber-reinforced polymer, and aluminum alloy. The results indicated that GFRP provided favorable structural performance and identified the "+" and "X" arrangements as suitable configurations for lightweight UAV frames [11]. The "+" and "X" configurations describe the frame orientation relative to the direction of forward flight, with one arm pointing forward in the "+" arrangement and the forward direction positioned between two adjacent arms in the "X" arrangement. These findings demonstrate that both frame geometry and material selection are important considerations in multirotor UAV design.

In addition to frame design, the number of rotors influences the payload capacity, stability, redundancy, and power requirements of a multirotor UAV. Figure 3 depicts a quadcopter, which uses four motor-driven propellers to generate lift and control aircraft motion. Quadcopters are widely used because of their relatively low cost, mechanical simplicity, commercial availability, and favorable thrust-to-weight ratio [3]. Their four-rotor configuration provides sufficient lifting capability for many small-scale inspection and monitoring applications. However, quadcopters generally offer lower payload capacity and less propulsion redundancy than multirotor configurations with additional rotors. In particular, a single motor failure can significantly affect controllability and potentially result in loss of the aircraft.

Figure 3: A quadcopter unmanned aerial vehicle [3]

A hexacopter, illustrated in Figure 4, uses six motor-driven propellers and provides several advantages for payload-intensive applications. Compared with a quadcopter, the additional rotors can increase payload capacity, stability, and propulsion redundancy [12]. Under appropriate operating conditions and control strategies, a hexacopter may also retain sufficient controllability to perform an emergency landing following certain motor-failure scenarios [13]. These benefits come at the expense of increased power consumption and additional motors, electronic speed controllers, and structural components [12].

The UAV developed in this research is intended to carry three inspection sensors and their supporting equipment, with an estimated combined mass of approximately 1.5–2 kg. Consequently, a hexacopter configuration was selected to provide the required payload capacity while maintaining stability, hovering capability, and precise maneuverability necessary for close-range infrastructure inspection. Although a quadcopter offers greater mechanical simplicity, the increased lifting capability and redundancy of the hexacopter make it better suited to the payload and operational requirements of the proposed system.

Figure 4: A hexacopter unmanned aerial vehicle [3]

The selection of a hexacopter introduces an important structural design challenge: the frame must support the additional propulsion components and inspection payload without imposing excessive weight on the aircraft. At the same time, the proposed UAV is intended to be customizable so that its structure can be adapted to different sensors, payload arrangements, and inspection requirements. These considerations motivate investigating additive manufacturing (AM) as an alternative approach for producing lightweight, application-specific UAV structures.

AM offers considerable design freedom and enables complex geometries to be manufactured without many of the constraints associated with conventional manufacturing processes. This capability is particularly relevant to UAV structures, where reducing mass while maintaining adequate mechanical performance can improve payload capacity and overall flight performance. Previous studies have applied generative design to carbon-fiber-reinforced quadcopter frames [14] and investigated continuous-carbon-fiber-reinforced Onyx for customized UAV structures [15]. However, these studies have primarily focused on quadcopters and provide limited experimental evaluation of commercially available 3D-printed materials for payload-carrying hexacopter structures. Furthermore, continuous-fiber printing systems can introduce additional manufacturing costs [16]. Therefore, this thesis investigates commercially available 3D-printing materials through mechanical testing and uses the experimentally measured properties to support the generative design and additive manufacture of a lightweight, customizable hexacopter structure.

1.3 Additive Manufacturing (AM) Background

Additive manufacturing (AM) originated from rapid prototyping technologies developed during the 1980s to produce three-dimensional models and prototype components layer by layer from computer-aided design (CAD) data [17]. One of the earliest demonstrations was presented by Hideo Kodama in the article "Three-Dimensional Data Display by Automatic Preparation of a Three-Dimensional Model" [18]. This work was followed by several major developments in AM technology, including stereolithography by Chuck Hull in 1987, selective laser sintering (SLS) patented by Carl Deckard in 1988, and fused deposition modeling (FDM) developed by Scott Crump in 1989 [18]. These early technologies were primarily used to produce models and prototypes for design visualization and evaluation rather than final components [17]. Nevertheless, rapid prototyping was adopted in several professional fields because of its ability to reduce product-development time and cost [17].

Stereolithography was developed by 3D Systems and became the first widely available AM process [17]. The process uses ultraviolet (UV) radiation to selectively cure a photosensitive polymer, forming a component one layer at a time [17]. While stereolithography can produce detailed polymer components, limitations include overcuring of unsupported or overhanging features, the need for manual post-processing, and potential warping caused by build-platform positioning errors [17].

Selective laser sintering (SLS) similarly fabricates components layer by layer but uses a laser to selectively fuse powdered material. During fabrication, a thin layer of powder is distributed across the build platform, and the laser heats selected regions to form each cross-section of the component [17]. SLS can process a range of materials, including polymers, metals, ceramics, and composite powders [17]. Unlike stereolithography, the process generally does not require separate support structures because the surrounding unsintered powder supports the component during fabrication. However, SLS requires carefully controlled operating temperatures and may require an inert-gas environment. Additional limitations include relatively rough surface finishes and reduced dimensional accuracy, particularly for larger components [17].

Another widely used AM process is fused deposition modeling (FDM), also known as fused filament fabrication (FFF). FFF is a material-extrusion process, illustrated in Figure 5, in which thermoplastic material is heated and deposited along a predefined path to construct a component layer by layer [19]. Compared with other AM processes, FFF is widely accessible because of its relatively low equipment and material costs, broad commercial availability, and ability to manufacture functional polymer components [16] [19]. These characteristics make FFF particularly attractive for applications requiring lightweight, customizable components, such as UAV structures.

As illustrated in Figure 5, motor-driven rollers feed thermoplastic filament into a heated print head, where the material is softened or melted before being extruded through a nozzle. The nozzle follows a toolpath generated from the CAD model to form the component, with support material added beneath overhanging features when necessary.

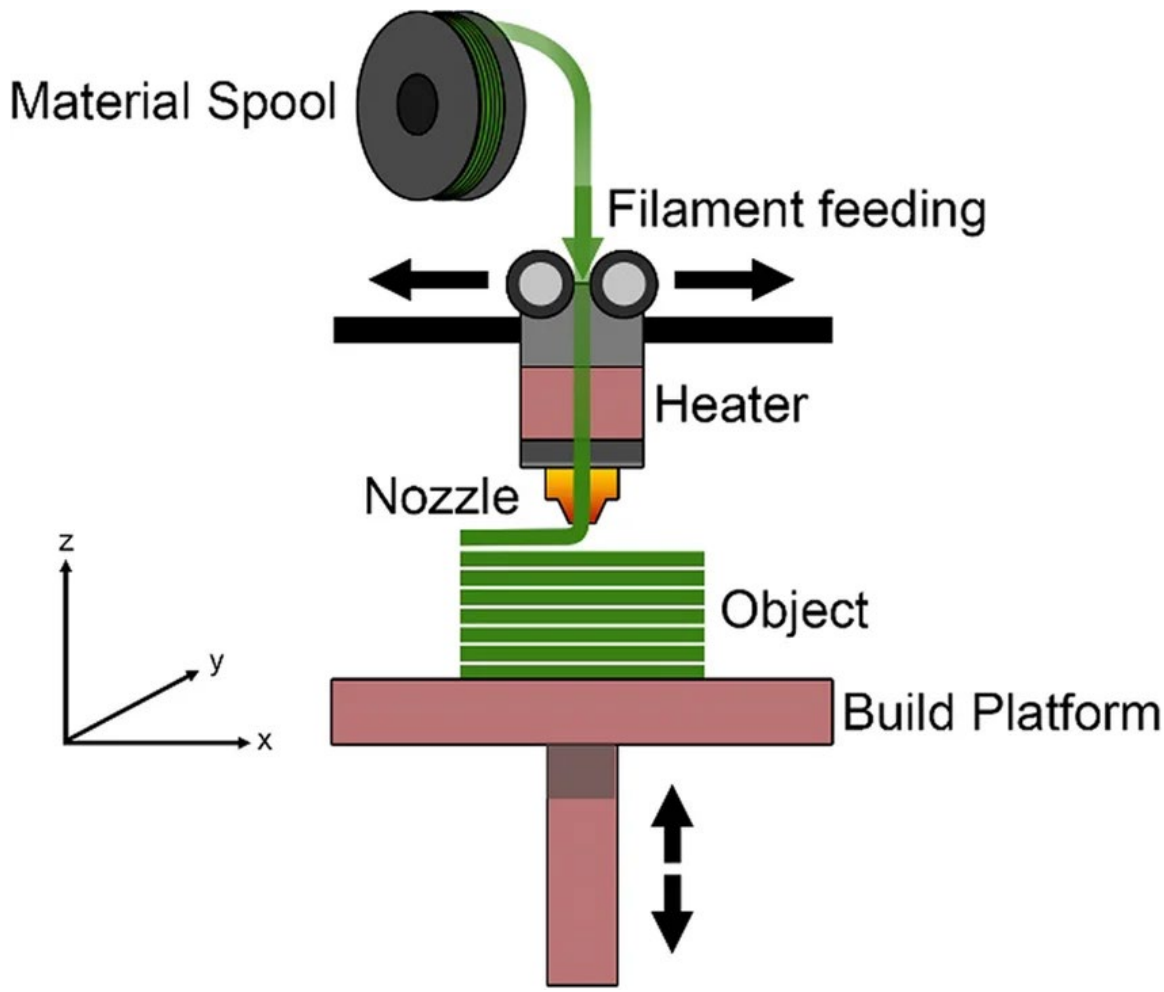

Figure 5: Fused deposition modelling (FDM) - [20]

1.4 Additive Manufacturing for UAV Structural Design

The low density, relatively low processing cost, and manufacturing flexibility of polymers make them well suited for additive manufacturing [19]. These characteristics are particularly advantageous for UAV structures, where minimizing component mass is important for maintaining payload capacity and flight performance. However, the relatively low strength and stiffness of unreinforced polymers can limit their use in load-bearing applications. To improve their mechanical performance, polymer composites incorporate reinforcements such as short fibers or particles into the polymer matrix [16] [21]. The resulting reinforced filaments can provide improved tensile strength and stiffness while retaining the manufacturing flexibility and low density desirable for lightweight UAV structures.

In addition to material selection, additive manufacturing provides opportunities to reduce structural mass through the fabrication of complex geometries that may be difficult or costly to produce using conventional manufacturing methods [22]. For example, lattice and cellular structures can be incorporated to reduce material usage while maintaining structural performance. Another approach is generative design, which uses specified design constraints, loads, and performance requirements to generate material-efficient geometries. The design freedom offered by additive manufacturing makes it well suited for producing these optimized geometries and allows UAV components to be customized for specific payloads and operational requirements, as illustrated by the customizable quadcopter in Figure 6 [22]. Consequently, combining generative design with additive manufacturing provides a potential method for reducing UAV structural mass while maintaining the required mechanical performance [23].

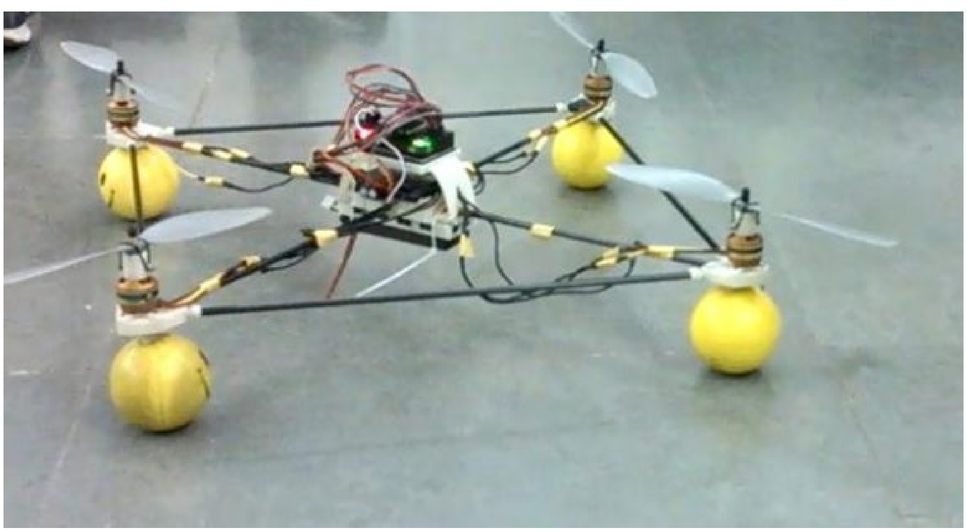

Figure 6: Customizable quadcopter [22]

Previous studies have demonstrated the feasibility of using additively manufactured polymers for UAV frames. Çaşka et al. [24] performed finite element analysis (FEA) on quadcopter chassis designs manufactured from polylactic acid (PLA) and acrylonitrile butadiene styrene (ABS), as shown in Figure 7. The calculated stresses were substantially below the reported yield strengths of both materials, indicating that the chassis were not expected to fail under the modeled loading conditions [24]. The study demonstrated the potential for common FFF materials to meet the structural requirements of lightweight UAV frames.

Generative design has also been investigated as a method for further improving the structural efficiency of additively manufactured UAV frames. Balayan et al. [14] evaluated PLA, ABS, and Nylon 6/6 for a generatively designed agricultural quadcopter chassis. The optimized ABS and Nylon 6/6 designs achieved calculated thrust-to-weight ratios of 1.49 and 1.48, respectively, compared with 1.39 for the reference DJI F450 configuration [14]. The study also reported an approximately 50% reduction in chassis mass and a 6.75% improvement in thrust-to-weight ratio relative to the reference design [14]. These results demonstrate the potential of integrating material selection, generative design, and additive manufacturing to reduce UAV structural mass while maintaining the performance required for flight.

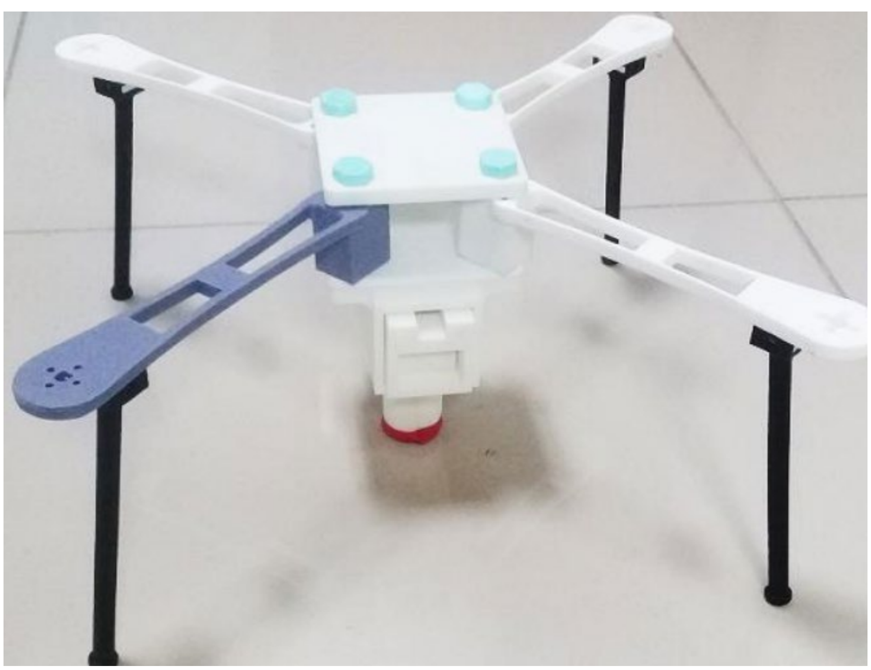

Figure 7:Fully 3D-printed drone model [24]

While previous studies demonstrate the feasibility of additively manufactured and generatively designed UAV structures, much of the existing work has focused on quadcopter configurations and a limited selection of polymer materials. The payload requirements of the hexacopter developed in this research create a need to evaluate materials and structural designs specifically for a larger, payload-carrying platform. Therefore, this research experimentally evaluates commercially available FFF materials and uses their measured mechanical properties to support the generative design of a lightweight, customizable hexacopter frame.

1.5 Research Gap and Objectives

Previous research has demonstrated the potential of additive manufacturing and generative design to reduce UAV-frame mass while maintaining structural performance. However, existing studies have primarily focused on quadcopters, micro-UAVs, and platforms with relatively limited payload requirements. Consequently, less attention has been given to additively manufactured structures for larger multirotor configurations designed to carry multiple inspection sensors and supporting equipment.

For close-range infrastructure inspection, the hexacopter developed in this research must maintain stable flight and hovering capability while carrying an estimated payload of approximately 1.5–2 kg and achieving a thrust-to-weight ratio of 1.75–3.0. Meeting these requirements requires sufficient propulsion and structural capacity while limiting the overall aircraft mass. The frame must therefore provide adequate strength and stiffness at minimal weight to preserve payload capacity and flight performance. In addition, because the mechanical properties of additively manufactured polymers are influenced by material and manufacturing conditions, experimentally measured properties are needed to accurately evaluate and optimize the structure.

The objective of this research is to develop and evaluate a lightweight, customizable hexacopter frame using additive manufacturing and generative design. Material characterization, propulsion testing, structural analysis, and experimental validation are combined to support the design process. The resulting frame is evaluated based on its structural performance, manufacturability, and ability to meet the requirements of a payload-carrying UAV for close-range infrastructure inspection.

The remainder of this thesis is organized as follows. Chapter II reviews generative design, topology optimization, and material-validation considerations relevant to additively manufactured UAV structures. Chapter III describes the material characterization, propulsion testing, generative design, finite element analysis, and manufacturing methods. Chapter IV presents and discusses the experimental, numerical, and flight-test results. Finally, Chapter V summarizes the principal conclusions, limitations, and recommendations for future work.

CHAPTER II

STRUCTURAL OPTIMIZATION AND MATERIAL CHARACTERIZATION

2.1 Generative Design for Structural Design Optimization

Generative design (GD) is an iterative computer-aided design process that uses algorithms and computational optimization to generate multiple design solutions. The designer defines the design space, preserved geometry, loads, constraints, materials, manufacturing methods, and performance requirements. These requirements may include limits on stress, displacement, vibration, thermal performance, mass, and factor of safety (FOS). The resulting design outcomes can then be evaluated and compared to identify solutions that best satisfy the specified requirements [25] [26].

GD has been applied to UAV frames to reduce structural mass while maintaining acceptable mechanical performance. Sharma et al. [25] generated 172 quadcopter-frame outcomes and selected two designs for further evaluation based on mass, stress, displacement, and FOS. The final selected design had a mass of 239.9 g (8.5 oz), compared with 282.0 g (10.0 oz) for the conventional DJI F450 frame, representing an approximately 14.9% reduction in mass. Maximum stress decreased from 21.33 MPa (3.09 ksi) to 12.83 MPa (1.86 ksi), while maximum displacement decreased from 4.02 mm (0.158 in) to 0.309 mm (0.012 in). Although the minimum FOS decreased from 3.3 to 1.5, it remained above the required value of 1.2 [25]. These results demonstrate that GD can remove material from a UAV frame while satisfying predefined structural requirements.

Similarly, Bright et al. [26] applied GD to a quadcopter frame and compared two generated designs with a conventional DJI Flame Wheel F450 frame using structural simulation. The design space incorporated preserved motor and central mounting regions, along with obstacle geometry to maintain clearance for UAV components. A force of 10 N (2.25 lb_f) was applied at each motor location, while the central mounting regions were constrained. One generated frame reduced the mass from 330 g (11.6 oz) to 267 g (9.4 oz) while also achieving lower maximum displacement and a higher FOS than the conventional frame [26]. Figure 8 compares the conventional DJI F450 frame with the improved generatively designed frame evaluated in the study.

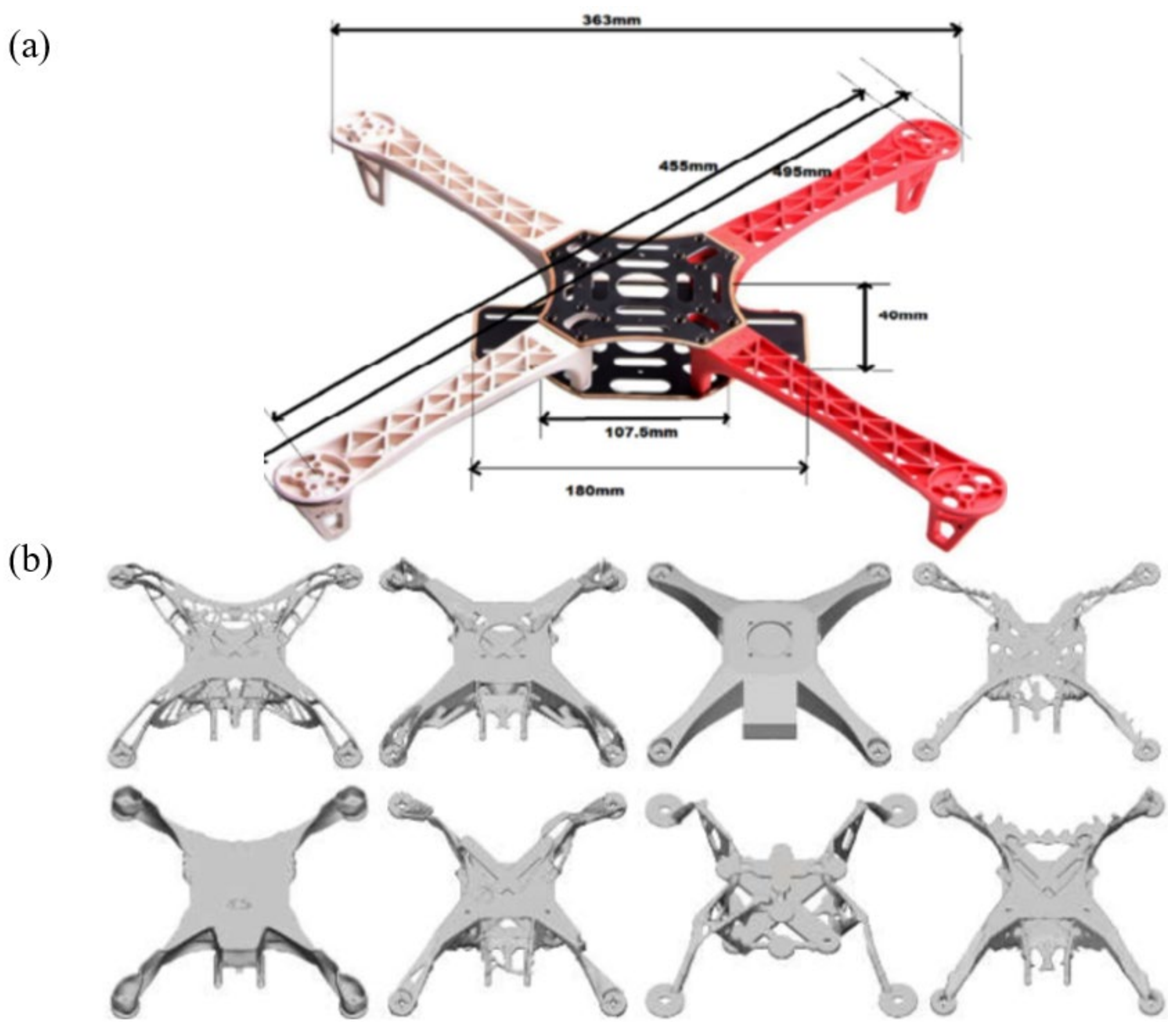

Figure 8: (a) Conventional DJI F450 frame and (b) generatively designed frame [22]

The application of GD is not limited to UAV structures. Aman [27] used the method to generate multiple design alternatives for a sheet-metal lifting bracket. Candidate designs were evaluated based on mass, manufacturing cost, maximum stress, displacement, FOS, material, and manufacturing method. An aluminum 5052 bracket was ultimately selected, post-processed, and evaluated through structural simulation to verify that it satisfied the required FOS [27]. This study demonstrates how GD enables multiple candidate solutions to be evaluated against both structural and manufacturing requirements rather than relying on a single manually developed geometry.

A key advantage of GD is the ability to incorporate manufacturing constraints directly into the design process. Generated geometries can be developed for additive manufacturing, 2.5-axis milling, three-axis milling, five-axis milling, two-axis cutting, and die casting [27]. Additive manufacturing is particularly compatible with GD because it can produce complex, material-efficient geometries that may be difficult to manufacture using conventional processes. Collectively, these studies show that GD can reduce structural mass while accounting for mechanical performance and manufacturing requirements, making it well suited for developing lightweight, additively manufactured UAV structures.

2.2 Topology Optimization for Structural Design Optimization

Topology optimization is a computational design method that determines an efficient distribution of material within a defined design space based on applied loads, boundary conditions, and structural requirements [14] [28]. One commonly used approach is the Solid Isotropic Material with Penalization (SIMP) method, in which the design space is divided into finite elements and each element is assigned a relative material density between 0 and 1. A value approaching 1 represents solid material, while a value approaching 0 represents a region where material can be removed. Intermediate densities are penalized during the optimization process, resulting in a design consisting primarily of solid and void regions [14].

Several studies have applied topology optimization to reduce the mass of UAV frames while maintaining structural performance. Balayan et al. [14] used the SIMP method to optimize the chassis of a DJI F450 agricultural quadcopter, achieving an approximately 50% reduction in chassis mass. The optimized design also produced a 6.06% increase in power-to-weight ratio, a 6.75% increase in thrust-to-weight ratio, an improvement of at least 11.8% in FOS, and a stress reduction of at least 70% [14]. These results demonstrate the potential of topology optimization to improve UAV structural efficiency through targeted material removal.

However, mass reduction alone does not ensure improved structural performance. Bay and Eryildiz [28] applied topology optimization to a drone frame with a target mass reduction of 30%, reducing the mass from 708.6 g (25.0 oz) to 545.1 g (19.2 oz), which corresponds to a mass reduction of approximately 23.1%. In Direction 1 of the simulation coordinate system, stress and displacement decreased by 22.4% and 7.8%, respectively. In contrast, stress in Direction 3 increased by 334.7% following optimization [28]. This substantial increase demonstrates that removing material can introduce localized regions of high stress and highlights the importance of evaluating optimized structures under multiple loading conditions.

Topology optimization has also been combined with additive manufacturing to produce lightweight UAV structures. Yap et al. [29] measured the mechanical properties of PA12 through ultrasonic and tensile testing and incorporated the experimentally determined properties into the numerical analysis of the micro-UAV shown in Figure 9. Following optimization, the frame was additively manufactured and mechanically tested, with the experimental force-displacement response showing agreement with the finite element analysis [29]. Additive manufacturing also enabled fabrication of the frame as a single component. According to the study, producing a comparable geometry using subtractive manufacturing would have required approximately five individual components joined using fasteners or adhesives [29]. This work demonstrates the compatibility of topology optimization and additive manufacturing for producing lightweight, integrated UAV structures.

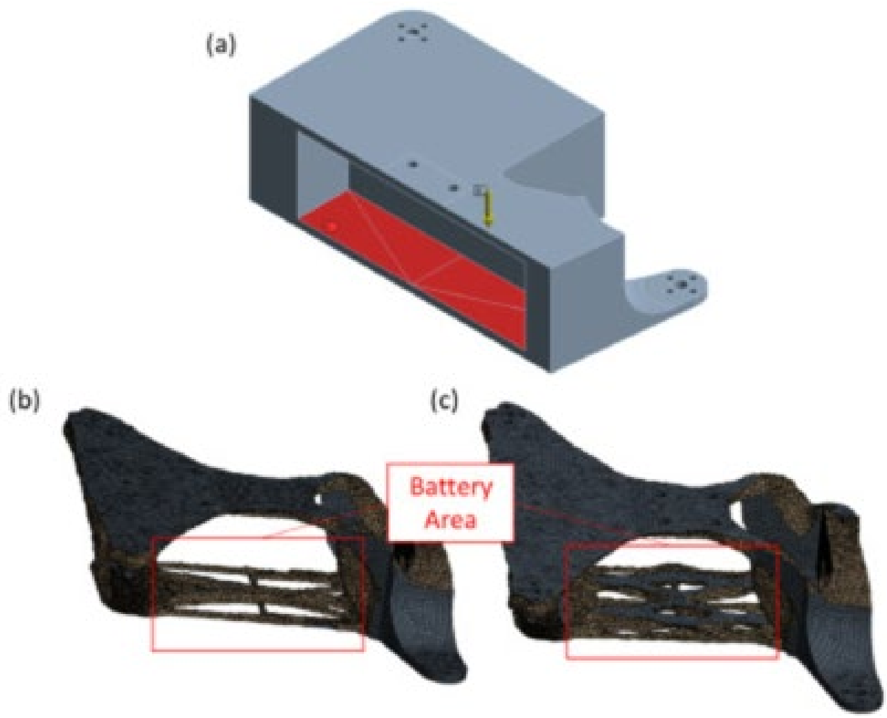

Figure 9: Topology-optimized micro-UAV [26]

Topology optimization can also be applied selectively to individual structural components rather than an entire UAV frame. Natarajan et al. [30] used the SIMP method to optimize three components of a multimodal flying and walking robot: the brushless DC motor mount, femur, and tibia. The masses of these components were reduced by 31.6%, 54.4%, and 36.1%, respectively. Finite element analysis was subsequently used to evaluate stress, displacement, and FOS under the specified loading conditions [30]. These results demonstrate the potential for targeted optimization of individual components where mass reduction can provide the greatest benefit.

Additional studies have demonstrated similar reductions in UAV structural mass. Al-Haddad et al. [31] combined topology optimization and additive manufacturing to redesign a PLA quadcopter frame, reducing its mass from 797 g (28.1 oz) to 400 g (14.1 oz), or approximately by 49.8%. Although the FOS decreased from 21.1 to 18.4 following material removal, it remained well above the required structural limit. The optimized frame was also evaluated using static structural and impact analyses before manufacturing [31]. Similarly, Sayyed et al. [32] reported an approximately 30% reduction in drone mass while maintaining the ability to carry a payload of up to 0.30 kg (0.66 lb). Their multi-objective approach distributed material according to the specified design requirements, reducing material use and associated manufacturing costs [32].

Collectively, these studies demonstrate that topology optimization can substantially reduce the mass of UAV frames and individual structural components. However, successful optimization requires more than achieving a target mass reduction. Optimized designs must also be evaluated for stress, displacement, structural safety, loading direction, and manufacturability [28] – [31]. Integrating experimentally determined material properties with additive manufacturing can further improve the reliability and manufacturability of optimized UAV structures, particularly when complex geometries are required.

2.3 Mechanical Behavior and Processing of FFF Materials

A key consideration when evaluating 3D-printed materials for structural applications is whether their mechanical behavior can be represented as isotropic or anisotropic. Isotropic materials exhibit the same mechanical properties in all directions, whereas anisotropic materials exhibit direction-dependent properties. This distinction is particularly important for FFF UAV structures because assuming isotropic behavior may not accurately represent the response of a printed component under service loading.

Chen et al. [33] explained that FFF components are generally anisotropic because material is extruded along defined paths and deposited in successive layers. Polymer chains tend to align with the extrusion direction, while bonding between adjacent layers depends on thermal diffusion and adhesion. As a result, interlayer strength is commonly lower than intralayer strength, causing mechanical properties to vary with print and loading directions [33]. This directional behavior can influence tensile, compressive, shear, and bending performance. Testing specimens manufactured in different orientations can therefore provide direction-dependent properties for material selection and finite element analysis.

In addition to print orientation, FFF mechanical performance is influenced by processing parameters such as layer height, nozzle diameter, infill density and pattern, printing speed, raster direction, extrusion temperature, and bed temperature [34]. Layer height affects surface quality, dimensional accuracy, and manufacturing time, while nozzle diameter influences deposited line width, material flow, and the range of usable layer heights. Wu [35], for example, selected a layer height of 0.14 mm (0.0055 in) for PLA specimens as a balance between printing time and the quality requirements of the study. A 0.40 mm (0.016 in) nozzle is also commonly used in desktop FFF systems because it provides a practical balance between printing speed and dimensional accuracy [34]. However, appropriate printing parameters depend on the material, equipment, component geometry, and performance requirements.

Infill density and pattern further influence component mass and mechanical response. Pop et al. [36] compared grid, line, and triangular infill patterns in PAHT-CF15 specimens manufactured at 50% infill density. Although the three patterns produced similar overall tensile and flexural behavior, the line pattern produced the highest average tensile strength of 59.4 MPa (8.6 ksi), while the triangular pattern produced the highest average flexural strength of 108.2 MPa (15.7 ksi) [36]. These results indicate that the influence of infill pattern should be evaluated within the specific material, geometry, and loading conditions of an application.

Processing conditions are especially important for short-carbon-fiber-reinforced polymers. Condruz et al. [16] found that raster orientation influenced the tensile and flexural properties of the evaluated materials, with the 90°/0° orientation generally producing the highest strength. PAHT-CF15 exhibited the strongest overall mechanical performance among the materials considered; however, microscopy revealed porosity and printing defects that could affect load transfer and mechanical behavior [16]. These findings show that adding carbon fiber does not automatically eliminate the weaknesses associated with FFF manufacturing. The way the material is deposited and the quality of the printed structure must also be considered. Similarly, Haque et al. [37] investigated the effects of material selection and several printing parameters on PLA, ABS, PLA-CF, PETG, and PAHT-CF specimens. Nozzle diameter was identified as the most influential printing parameter under the conditions investigated, and PAHT-CF exhibited the best overall tensile, compressive, and flexural performance among the tested materials [37]. Together, these studies identify PAHT-CF as a promising candidate for lightweight structural applications while emphasizing the importance of controlling its manufacturing conditions.

Post-processing provides another method for modifying the mechanical behavior of FFF materials. Annealing is a heat treatment in which a printed component is heated for a specified period and subsequently cooled. The process can increase crystallinity, relieve residual stresses, and improve bonding within the printed structure, potentially increasing strength, stiffness, hardness, and dimensional stability. However, the response depends on the material and treatment conditions, and excessive temperature or exposure can produce shrinkage, expansion, or warping [38] [39].

The effects of annealing have been investigated for several FFF polymers. Szust and Adamsk [40] reported that annealing PLA at 60°C (140°F) for one hour increased tensile strength by approximately 24%, although deformation and anisotropic behavior remained. Wijnbergen et al. [41] similarly observed increased tensile strength in longitudinally printed Tough PLA specimens but not in transversely printed specimens, indicating that annealing does not necessarily overcome weak interlayer bonding. Valvez et al. [38] reported flexural-strength increases of up to 10.2% for PETG and 31.8% for PETG-CF, along with improvements in flexural modulus, hardness, impact strength, and creep resistance. However, higher temperatures and longer exposure times resulted in greater dimensional changes [38] [42]. Yu et al. [39] likewise reported increased crystallinity, flexural strength, and stiffness in semicrystalline PLA, accompanied by longitudinal shrinkage and thickness expansion. These studies demonstrate that the potential mechanical benefits of annealing must be balanced against its effects on component dimensions.

The reviewed literature supports PAHT-CF as a candidate material for lightweight UAV structures but also identifies areas requiring further investigation. Previous studies have primarily characterized its tensile, compressive, and flexural behavior under specific printing conditions, while annealing studies have largely focused on PLA, PETG, and PETG-based composites. Consequently, these findings cannot be directly extended to annealed PAHT-CF or to loading conditions relevant to the proposed UAV structure. In particular, UAV arms may experience torsion in addition to tension, compression, and bending. The present study therefore compares annealed and unannealed PAHT-CF through tensile, compression, and torsion testing to characterize its strength, stiffness, and shear response while evaluating dimensional changes associated with heat treatment. The resulting experimentally determined properties provide the material basis for the structural analysis and generative design procedures described in Chapter III.

CHAPTER III

EXPERIMENTAL SETUP AND METHODOLOGY

The research presented in this thesis combined experimental material characterization with finite element analysis (FEA), generative design, propulsion testing, and component manufacturing. Figure 10 summarizes the five phases of the workflow methodology. The process began with preliminary material screening and expanded mechanical characterization. Experimentally determined material properties were then used to analyze the UAV arms and landing gear, and the selected designs were subsequently manufactured and evaluated.

Tensile, compression, and torsion tests provided elastic modulus, strength, apparent compression Poisson's ratio, and apparent torsional shear modulus values. These results supported material comparison and supplied the properties used in the numerical models. Because the printed specimens contained internal infill and direction-dependent layer interfaces, the measured values represented the tested printed configurations rather than fully dense, isotropic bulk polymers.

The selected motor, propeller, electronic speed controller, and battery configuration were tested to determine thrust and current. The measured maximum thrust established the motor load used in the arm analyses. Selected arm designs were then manufactured and evaluated with the laser deflection-measurement system. This sequence connected material testing and numerical design with component-level experimental verification.

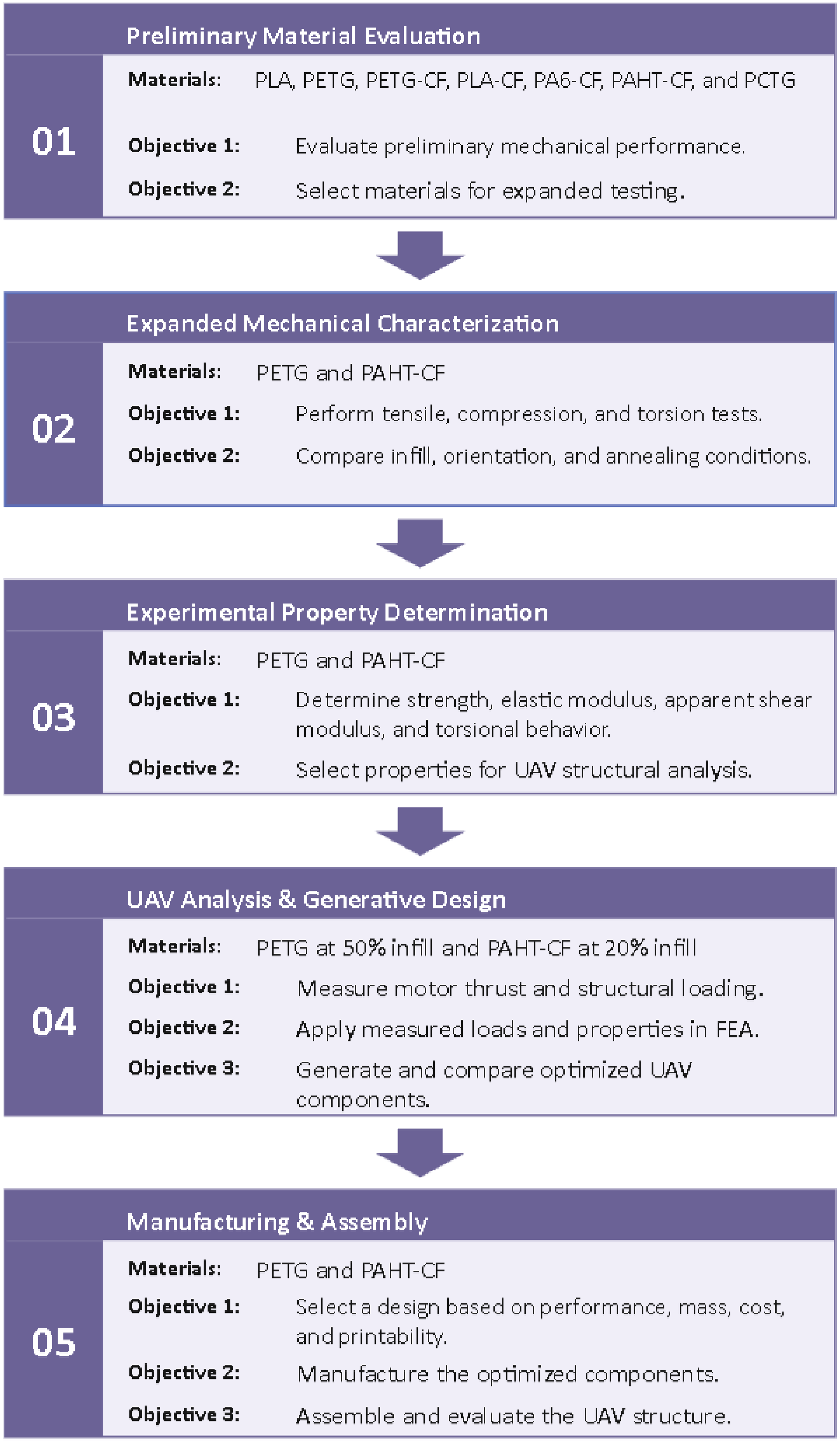

Figure 10: Design and optimization development workflow

3.1 Materials and Specimen Manufacturing

3.1.1 Materials Evaluated

Seven commercially available thermoplastic filaments were evaluated in this study: (1) polylactic acid (PLA), (2) glycol-modified polyethylene terephthalate (PETG), (3) carbon-fiber-reinforced polylactic acid (PLA-CF), (4) carbon-fiber-reinforced glycol-modified polyethylene terephthalate (PETG-CF), (5) carbon-fiber-reinforced polyamide 6 (PA6-CF), (6) high-temperature carbon-fiber-reinforced polyamide (PAHT-CF), and (7) glycol-modified polycyclohexylenedimethylene terephthalate (PCTG). The materials and their respective manufacturers are summarized in Table 1.

Table 1: Materials evaluated

Material	Manufacturer	Reinforcement
PLA	ELEGOO	Unreinforced Polymer
PETG	OVERTURE	Unreinforced Polymer
PLA-CF	Bambu Lab	Carbon-Fiber-Reinforced
PETG-CF	Bambu Lab	Carbon-Fiber-Reinforced
PA6-CF	Bambu Lab	Carbon-Fiber-Reinforced
PAHT-CF	Bambu Lab	Carbon-Fiber-Reinforced
PCTG	3DXTECH	Unreinforced Polymer

ELEGOO manufactured the PLA filament, OVERTURE the PETG, 3DXTECH the PCTG, and Bambu Lab the four carbon-fiber-reinforced filaments. The selected materials included both unreinforced thermoplastics and short-carbon-fiber-reinforced filaments, providing a range of materials for evaluating mechanical performance and suitability for lightweight UAV structural components.

PLA and PETG were selected as commonly used unreinforced AM-FFF materials to provide baseline performance for comparison with the reinforced materials, while PCTG was included as an additional engineering copolyester. PLA-CF and PETG-CF were evaluated to investigate the influence of short-carbon-fiber reinforcement on their respective polymer systems. PA6-CF and PAHT-CF were included as reinforced polyamides intended for more demanding structural applications. The materials were evaluated using the experimental plan described in the following sections, with the extent of testing determined by their preliminary performance and relevance to the proposed UAV structure. Initial testing was used to identify promising materials for further characterization through tensile, compression, and torsion testing, as well as evaluation of infill density, print orientation, and annealing conditions. To ensure consistent comparison across these evaluations, specimens were manufactured using controlled printing parameters and test-specific geometries, as described in the following section.

3.1.2 Specimen Manufacturing

All experimental specimens were manufactured using a Bambu Lab X1 Carbon fused-filament-fabrication printer. The specimen geometries were prepared and sliced for fabrication using Bambu Studio. Standard material-specific printing profiles were retained for parameters such as nozzle temperature, build-plate temperature, cooling, and printing speed. Selected manufacturing parameters, including nozzle diameter, layer height, wall loops, shell layers, infill density, print orientation, and annealing condition, were controlled according to the objectives of each experiment, as illustrated in the developmental workflow in Figure 10. The general manufacturing parameters used in this study are summarized in Table 2.

Carbon-fiber-reinforced filaments were printed using a 0.60 mm (0.024 in) nozzle and a 0.24 mm (0.0094 in) layer height, while unreinforced filaments were printed using a 0.40 mm (0.016 in) nozzle and a 0.16 mm (0.0063 in) layer height, as summarized in Table 2. The larger nozzle was selected to promote reliable extrusion of the fiber-filled materials. Therefore, comparisons between reinforced and unreinforced materials reflect their performance under the selected manufacturing conditions rather than the effect of fiber reinforcement alone.

Table 2: General printing parameters for specimens

Printing Parameter	PLA	PETG	PCTG	PLA-CF	PETG-CF	PA6-CF	PAHT-CF
Nozzle diameter, mm (in)	0.40 (0.016)	0.40 (0.016)	0.40 (0.016)	0.60 (0.024)	0.60 (0.024)	0.60 (0.024)	0.60 (0.024)
Layer height, mm (in)	0.16 (0.0063)	0.16 (0.0063)	0.16 (0.0063)	0.24 (0.0094)	0.24 (0.0094)	0.24 (0.0094)	0.24 (0.0094)
Wall loops	4	4	4	4	4	4	4
Top shell layers	3	3	3	3	3	3	3
Bottom shell layers	3	3	3	3	3	3	3
Infill pattern	Rectilinear	Rectilinear	Rectilinear	Rectilinear	Rectilinear	Rectilinear	Rectilinear
Primary infill densities	20, 40, 60, 80%	20, 40, 60, 80%	20, 40, 60, 80%	20, 40, 60, 80%	20, 40, 60, 80%	20, 40, 60, 80%	20, 40, 60, 80%
Additional infill densities*	10, 90, 100%	10, 90, 100%	10, 90, 100%	10, 90, 100%	10, 90, 100%	10, 90, 100%	10, 90, 100%
Drying condition	—	—	—	—	—	70°C, 16 h	70°C, 16 h
Final dryer RH	—	—	—	—	—	12–15%	12–15%

*Additional infill densities were used only in selected experiments.

Infill density and print orientation were varied according to the objectives of each experimental stage. Primary infill densities of 20%, 40%, 60%, and 80% were evaluated, with 10%, 90%, and 100% included in selected experiments. Initial results were used to identify conditions that provided a favorable balance between mechanical performance and specimen mass, and subsequent testing focused on the most promising conditions. As a result, not every material was evaluated at every infill density.

Print orientation was selected according to specimen geometry and loading condition. Tensile specimens were manufactured flat, on-edge, and vertically, while cylindrical specimens were printed horizontally, vertically, and, in selected experiments, at 45° or 60° relative to the build plate. Selected specimens were also annealed to evaluate the effects of thermal post-processing. Because these variables were investigated at different stages of the experimental program, not every material was tested using every combination of infill density, print orientation, and annealing condition.

3.2 Material Mechanical Property Characterization

3.2.1 Tensile Testing Procedure (ASTM-D638)

Uniaxial tensile testing was conducted to determine the elastic modulus, ultimate tensile strength, and engineering stress–strain response of the investigated materials [43]. Tensile specimens were modeled in Fusion 360 according to the ASTM D638 Type I geometry, a standardized specimen configuration used to characterize the tensile properties of reinforced and unreinforced polymers. The nominal specimen dimensions are summarized in Table 3 and the technical drawing is provided in Appendix B.

Table 3: Dimensions of ASTM D638 specimens

Dimension	Symbol	Nominal value mm (in)
Overall length, minimum	L_0	165.0 (6.50)
Grip-section width	W_0	19.0 (0.748)
Reduced-section length	L	57.0 (2.24)
Reduced-section width	W	13.0 (0.512)
Gauge length	G	50.0 (1.97)
Distance between grips	D	115.0 (4.53)
Fillet radius	R	76.0 (2.99)
Specimen thickness	T	3.2 (0.126)

The same nominal geometry was used for all materials and manufacturing conditions to provide a consistent basis for comparison. Each specimen had a nominal thickness of 3.2 mm (0.126 in), a reduced-section width of 13 mm (0.512 in), and a gauge length of 50 mm (1.97 in). The infill densities and other manufacturing conditions varied according to the material and experimental stage, as summarized in Table 2.

Tensile testing was performed using an Instron 5966 dual-column tabletop universal testing machine with a 30 kN (6,744 lb_f) force capacity, as shown in Figure 11. Before testing, the width and thickness of each specimen were measured within the reduced section and entered into the testing software to determine the initial cross-sectional area. The specimen was then secured between the tensile grips and aligned with the loading axis to minimize bending and off-axis loading. The initial grip separation was set to 115 mm (4.53 in).

Each specimen was loaded in uniaxial tension at a constant crosshead speed of 5 mm/min (0.197 in/min) until failure or the specified test-ending condition was reached. Following each test, the fractured specimen was removed, and the testing system was returned to its initial position before the next specimen was installed. Three to five replicate specimens were tested for each selected condition to assess repeatability and account for specimen-to-specimen variation. The Instron testing software recorded load and extension throughout each test and generated the corresponding engineering stress–strain response. The raw data were exported for subsequent analysis and comparison among the selected experimental conditions.

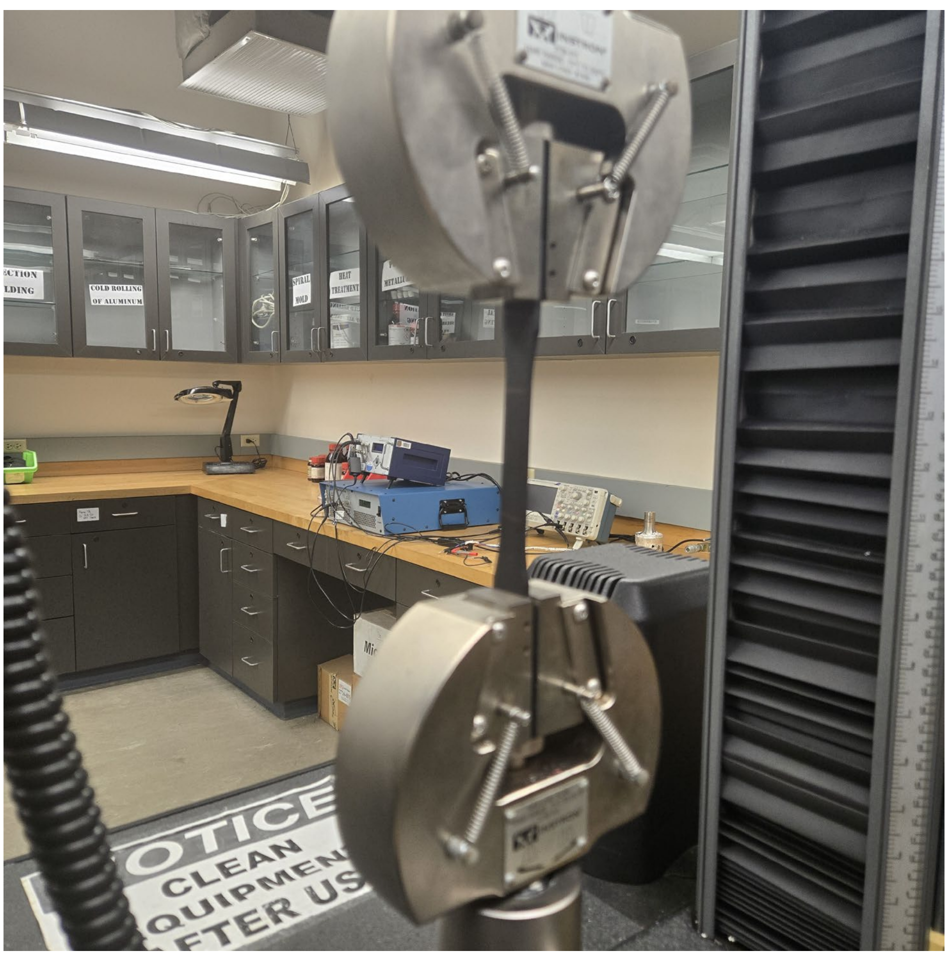

Figure 11: Instron tensile testing setup

3.2.2 Compression Testing Experiments (ASTM-D695)

Compression testing was performed to characterize the compressive stress–strain response of the additively manufactured materials and determine their apparent Poisson's ratios. The resulting properties were used to compare material performance under the selected manufacturing conditions and provide experimentally determined input data for the finite element analysis of the generatively designed UAV components [43].

Compression specimens were manufactured as right circular cylinders with a nominal diameter of 25.4 mm (1.00 in) and length of 50.8 mm (2.00 in). Appendix B shows a technical drawing of the specimen. The same nominal geometry was used for all selected materials and manufacturing conditions to provide a consistent basis for comparison.

The compression-testing procedure was based on ASTM D695; however, the specimen diameter differed from the preferred cylindrical geometry specified by the standard. Therefore, the testing procedure was not considered fully compliant. Table 4 compares the applicable ASTM D695 specimen specifications with the dimensions and testing conditions used in this study.

Compression testing was performed using an Instron 68FM-300 dual-column floor universal testing machine equipped with compression plates with a load capacity of 300 kN (67,440 lb_f), as shown in Figure 12. Before testing, the initial diameter and length of each specimen were measured using a dial caliper, and the measured diameter was used to calculate the initial cross-sectional area. Each specimen was centered between the compression plates to promote uniform axial loading and minimize eccentric or off-axis loading.

Table 4: Compression experiment specifications

Parameter	ASTM D695-15 Specification	Experimental Condition
Specimen shape	Right cylinder or rectangular prism	Right circular cylinder
Preferred cylinder for compressive strength	12.7 mm (0.500 in) diameter × 25.4 mm (1.00 in) length	25.4 mm (1.00 in) diameter × 50.8 mm (2.00 in) length
Preferred cylinder for modulus or offset yield	12.7 mm (0.500 in) diameter × 50.8 mm (2.00 in) length	25.4 mm (1.00 in) diameter × 50.8 mm (2.00 in) length
Length-to-diameter ratio	2:1 for preferred strength cylinder; 4:1 for preferred modulus cylinder	2:1
Crosshead speed	1.3 ± 0.3 mm/min (0.051 ± 0.012 in/min)	1.6 mm/min (0.0630 in/min)
Dimensional measurements	Initial specimen dimensions measured before testing	Initial and final diameter and length measured using a dial caliper
Number of specimens	At least five specimens generally recommended	Three to five specimens per selected condition

The specimens were compressed at a constant crosshead speed of 1.6 mm/min (0.0630 in/min) until the selected test-ending condition was reached. Applied load and crosshead displacement were recorded throughout each test and used to determine the compressive stress–strain response. Three to five replicate specimens were tested for each selected material and manufacturing condition to assess repeatability and account for specimen-to-specimen variation. Table 2 summarizes the material, infill density, print orientation, annealing condition, and number of specimens evaluated for each test condition.

Figure 12: Compression testing at Civil Engineering Laboratory

The apparent Poisson's ratio, ν_{eff}, was estimated from the measured lateral and axial strains according to $\nu_{eff} = -\varepsilon_{lateral}/\varepsilon_{axial}$ where the lateral strain was calculated as $\varepsilon_{\mathrm{lateral}} = (D_f - D_0)/D_0$ and the axial strain was calculated as $\varepsilon_{\mathrm{axial}} = (L_f - L_0)/L_0$. Here D_0 and L_0 represent the initial specimen diameter and length, respectively, while D_f and L_f represent the corresponding dimensions after compression. During the testing, the specimen diameter increased while its length decreased, resulting in positive lateral strain and negative axial strain.

Because the final dimensions were measured manually after unloading rather than continuously within the elastic region, the calculated values do not represent a conventional elastic Poisson's ratio. Instead, they were treated as apparent compressive Poisson's ratios representing the dimensional response of the specimens under the selected testing conditions. The calculated values may therefore include contributions from permanent deformation.

3.2.1 Torsion Experimental Testing (ASTM-E143-20)

Torsion testing was performed to determine the shear modulus of the 3D-printed materials for use in the finite element analysis of the generatively designed UAV components in Fusion 360. The testing procedure was based on ASTM E143-20 and the torsion-testing method described in [44]. The torsion specimens had an overall length of 142 mm (5.59 in), a reduced-section diameter of 6.1 mm (0.24 in), and a reduced-section length of 78 mm (3.07 in). The grip-section width was 13.2 mm (0.52 in), and the transition section measured 6.35 mm (0.25 in). A gauge length of 50 mm (1.97 in) was used to measure the angle of twist for the shear-modulus calculation. Specimens with infill densities of 20% and 40% were evaluated to investigate the influence of infill density on torsional behavior. The specimen geometry and dimensions are summarized in Table 5, with the corresponding technical drawing provided in Appendix B.

Table 5: Torsional specimen dimensions and calculations

Parameter	Tested value
Overall specimen length	142.0 mm (5.59 in)
Grip-section width	13.2 mm (0.52 in)
Reduced-section diameter	6.10 mm (0.24 in)
Reduced-section length	78.0 mm (3.07 in)
Gauge length	50 mm (1.97 in)
Loading rate	0.1 rev/min (36°/min)
Test temperature	21°C (69.8°F) Room Temperature
Infill densities tested	20% and 40%
Shear modulus calculation	$G = TL/(J\theta)$
Polar moment of inertia calculation	$J = \pi d^4/32$
Nominal maximum surface shear stress calculation	$\tau_{max} = Tr/J$
Nominal surface shear strain calculation	$\gamma_{max} = r\theta/L$
Apparent torsional shear modulus	$G_{app} = \Delta\tau/\Delta\gamma$

Torsion testing was conducted using the SM1 MkII torsion-testing machine pictured in Figure 13. Before testing, the machine was calibrated according to manufacturer specifications. Each specimen was secured in the grips and aligned with the axis of rotation to minimize bending and off-axis loading. Torque was applied by rotating the degree wheel at approximately 0.1 rev/min (36°/min). The applied torque and corresponding angle of twist were recorded throughout each test for subsequent determination of the shear modulus.

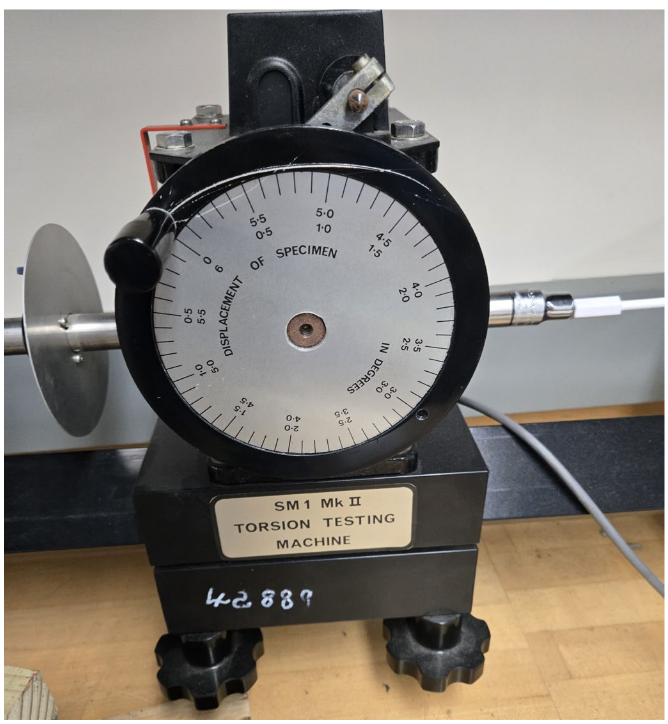

Figure 13: Torsion testing machine SM1 MkII

Table 5 summarizes the equations used to determine the torsional shear properties. The shear modulus, G, was calculated using the applied torque, T, gauge length, L, polar moment of inertia, J, and angle of twist, θ. A gauge length of 50 mm (1.97 in) was used, and the polar moment of inertia was determined from the nominal specimen diameter, d.

The nominal maximum surface shear stress and shear strain were calculated from the recorded torque and angle of twist, respectively. The apparent torsional shear modulus was determined from the slope of the initial approximately linear region of the resulting shear stress–shear strain response. Later constant-torque plateau regions, in which the specimen continued to rotate with little change in recorded torque, were excluded from the modulus calculation.

Because the specimens contained internal infill but were evaluated using equations for a solid circular cross-section, the calculated stress and strain values are reported as nominal shear properties, and the resulting modulus is reported as the apparent torsional shear modulus. These values characterize the response of the printed specimen configuration and provide a consistent basis for comparison among the tested materials and infill conditions.

3.3 Propulsion and Flight-Control Systems and Testing

3.3.1 Propulsion and Control Systems

The electronic and propulsion components were selected based on the required thrust, operating voltage, estimated UAV weight, and compatibility with the hexacopter configuration. The system consisted of six motors, six electronic speed controllers (ESCs), six propellers, a battery, a power module, a flight controller, a GPS module, and a radio-control system. The primary components and their specifications are summarized in Table 6.

The propulsion system consisted of six SunnySky V4008 380-KV brushless motors, Hobbywing Skywalker 60-A ESCs, and EOLO CN 330.2 × 127.0 mm (13 × 5 in) propellers, with one motor, ESC, and propeller installed on each arm. The motors and propellers were paired with a 6S 10,000-mAh lithium-polymer battery to provide the thrust required for the estimated takeoff mass and intended payload. The thrust, current draw, electrical power, and propulsion efficiency of this configuration were evaluated experimentally.

Table 6: UAV propulsion and control system components

Component	Manufacturer/Model	Qty	Key Specification and/or Description
Brushless motor	SunnySky V4008	6	380 KV – Rotates the propellers to generate thrust
Electronic speed controller	Hobbywing Skywalker 60A	6	60A – Regulates the speed of each motor
Propeller	EOLO CN	6	330.2 × 127.0 mm (13 × 5 in) – Converts motor rotation into thrust
Battery	6S LiPo	1	10,000 mAh (22.2 V nominal)
Flight controller	Pixhawk	1	Controls and stabilizes the UAV
Power module	PM02D, 2S–12S	1	2S–12S – Supplies regulated power and measures battery voltage and current
GPS module	Standard Pixhawk-compatible GPS	1	Provides positioning and navigation data
Radio transmitter	RadioMaster TX16S	1	Sends pilot commands to the UAV
Radio receiver	ExpressLRS ER6	1	Receives pilot commands from the transmitter

A Pixhawk flight controller was used to control and stabilize the hexacopter by processing pilot commands and adjusting the signals sent to each ESC. The 6S battery supplied power at a nominal voltage of 22.2 V through a PM02D power module rated for 2S-12S batteries, which provided regulated power to the flight controller and enabled battery voltage and current monitoring. A GPS module provided positioning and navigation information, while a RadioMaster TX16S transmitter and ExpressLRS ER6 receiver provided radio control. Before propeller installation, the motor numbering, rotational directions, and flight-controller output assignments were verified for the selected hexacopter configuration.

Figure 14 illustrates the general connection layout of the propulsion, power, and flight-control systems. The battery was connected through the PM02D power module to the power-distribution system, while the Pixhawk provided control signals to the six ESCs. Each ESC controlled its corresponding motor, and the GPS module and radio receiver were connected to the appropriate flight-controller ports.

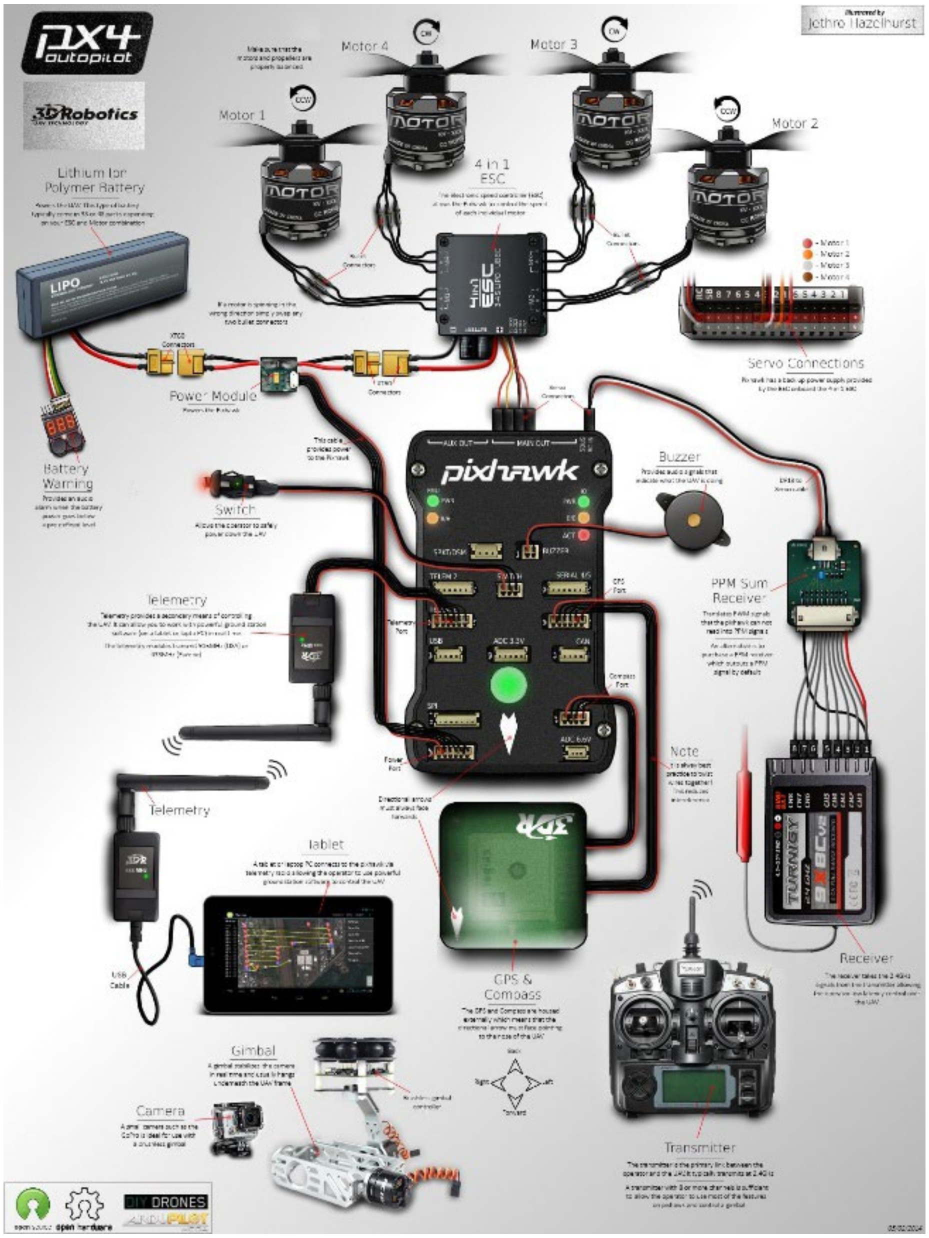

Figure 14: Pixhawk layout [45]

3.3.2 Testing: Cyclic Loading

Cyclic loading was performed to evaluate the durability of the generatively designed UAV arm under repeated motor-induced loading. During operation, UAV arms are subjected to repeated rotor forces that can contribute to fatigue damage and crack initiation, particularly near the arm-to-frame connection [46]. To represent this loading condition, the arm was mounted as a cantilever beam, with one end secured to the test frame using screws and the motor attached at the opposite end. An Arduino program controlled the motor operation by repeatedly varying the thrust to simulate cyclic loading. The Arduino code used for testing is provided in Appendix A.

A laser-based system, depicted in Figure 15 was used to estimate the vertical deflection of the arm over a thrust range from zero to approximately 15.7 N (3.53 lbf), equivalent to 1,600 gf. Before testing, the laser was aligned with the unloaded arm, and the initial laser brightness was established as the reference condition. As motor thrust increased, the arm deflected, and the laser moved from its initial alignment, reducing brightness. The laser assembly was then adjusted vertically until the reference brightness was restored. Because the assembly could be repositioned in 1 mm (0.0394 in) increments, the vertical adjustment required to restore the reference condition provided an estimate of arm deflection at the corresponding thrust level.

Figure 15: Laser deflection measuring system

The arm was repeatedly loaded using the motor and propeller to reproduce the forces expected during UAV operation. The fixed support represented the connection between the arm and the central frame, while the motor generated loading at the free end. The arm was inspected throughout testing for visible deformation, cracking, loosening near the mounting points, or other evidence of fatigue-related damage. This setup allowed the structural response of the complete arm to be evaluated under realistic motor-generated loading rather than applying a simplified force to a small material specimen as shown in Figure 16.

Figure 16: Generated-design specimen on tester

3.3.3 Testing: Propulsion Thrust and Current

A motor thrust tester was used to characterize the thrust produced by the selected motor-and-propeller combination and determine whether the propulsion system could provide sufficient lift for the UAV. The test setup, illustrated in Figure 17, consisted of a load cell connected to an HX711 amplifier and an Arduino. Before testing, the load cell was calibrated using known weights and their corresponding digital readings to establish a calibration factor. During testing, the HX711 amplified and converted the load-cell signal into digital data, which was processed by the Arduino to determine thrust as the motor speed increased from minimum to maximum throttle. The Arduino code used for data acquisition is provided in APPENDIX A.

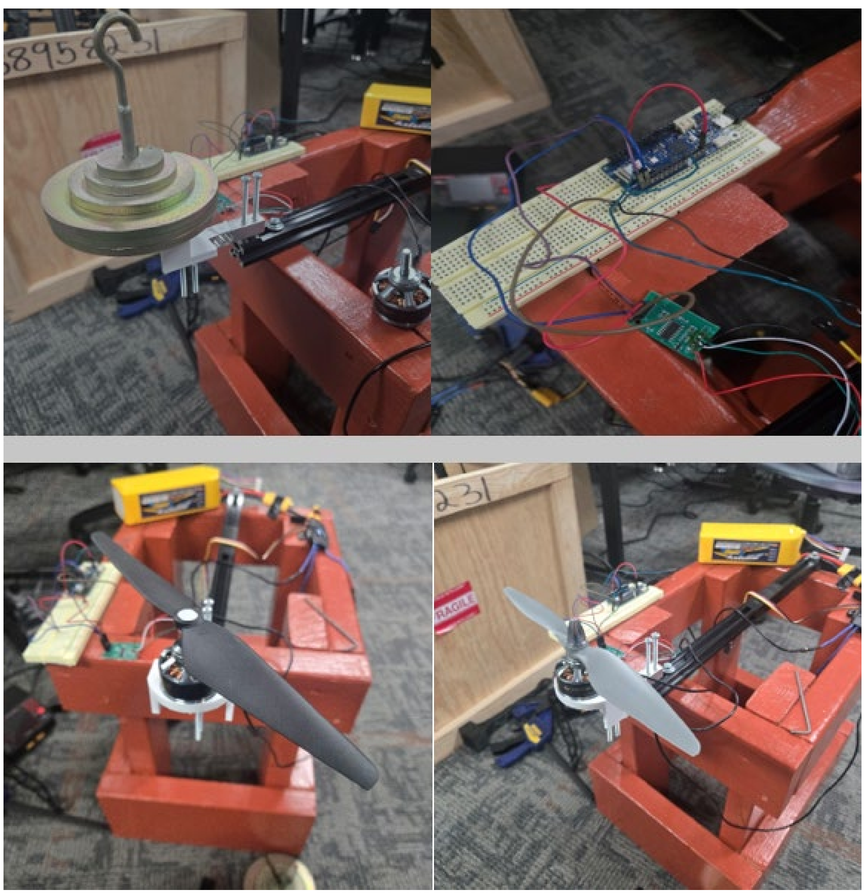

Figure 17: Arduino setup with HX711

Electrical current was measured simultaneously at different throttle settings to characterize the power requirements of the propulsion system and support subsequent battery and flight-time calculations. The current-measuring device was connected in series between the battery and electronic speed controller (ESC), allowing the DC input current to be measured on the battery side of the system. This location was selected because the connection between the ESC and brushless motor carries a three-phase, pulse-width-modulated signal that is not suitable for direct series measurement using a standard multimeter. The resulting thrust and current measurements were used to evaluate propulsion performance and determine whether the selected system could satisfy the lift and endurance requirements of the UAV.

3.3.4 Performance Analysis

The thrust and current measurements obtained from the single-motor propulsion tests were used to estimate the performance of the six-motor UAV. Measurements collected at multiple throttle settings were used to calculate total propulsion thrust, current, and electrical power, thrust-to-weight ratio, thrust-to-power ratio, and estimated flight time for the final hexacopter configuration.

The total available thrust was estimated by scaling the measured single-motor thrust to the six motors used on the UAV: $T_{total} = nT_{motor}$, where T_{total} is the estimated total thrust produced by the UAV, n is the number of motors ($n = 6$), and T_{motor} is the measured thrust produced by one motor at a given throttle setting. Similarly, the total propulsion current was estimated as $I_{prop,total} = nI_{motor}$, where I_{motor} is the measured current of one motor–ESC–propeller combination. This value represents the estimated propulsion-system current and excludes the smaller electrical loads associated with the flight controller, GPS, receiver, telemetry system, and other onboard electronics.

The corresponding electrical power supplied to the propulsion system was calculated as $P_{prop} = VI_{prop,total}$, where ($V$) is the measured battery voltage. The thrust-to-weight ratio was used to evaluate whether the propulsion system provided sufficient thrust for the total takeoff mass T/W $= T_{total}\ (kgf)/m_{TO}\ (kg)$, where m_{TO} is the total takeoff mass when thrust is expressed in kilogram-force and mass in kilograms. The same dimensionless ratio is obtained when thrust and weight are expressed consistently in U.S. customary units. A thrust-to-weight ratio of 1 represents the theoretical minimum required to support the UAV in hover and provides no reserve for takeoff, climbing, maneuvering, wind disturbances, or payload variations. A target thrust-to-weight ratio of 2 was therefore selected as the design-performance target. At this ratio, hover theoretically occurs at approximately 50% of the maximum available thrust, providing additional thrust capacity for flight maneuvers and disturbances. This value was used as a design criterion rather than a flight-certification requirement.

Based on the selected target, the required thrust per motor was calculated as $T_{req,motor} = (T/W)_{target} m_{TO}/n$, where $(T/W)_{target}$ is the total takeoff mass, and (n) is the number of motors. This relationship was used to compare the required motor thrust with the experimentally measured propulsion performance.

The thrust-to-power ratio was calculated to compare the thrust produced relative to the electrical power consumed by each motor-propeller configuration:

$$R_{T/P} = \frac{T_{motor}}{V\ I_{motor}}$$

where $R_{T/P}$ is the thrust-to-power ratio, T_{motor} is the measured thrust produced by one motor, V is the measured battery voltage, and I_{motor} is the measured motor current. In this study, thrust was recorded as a gram-force equivalent; therefore, the thrust-to-power ratio was reported in grams per watt (g/W). A higher value indicates that the motor-propeller configuration produces more thrust for each watt of electrical power consumed. This quantity is a propulsion-performance metric rather than a dimensionless energy-conversion efficiency. Because motor, electronic speed controller (ESC), and propeller performance varies with operating conditions, the throttle setting that produces the highest thrust-to-power ratio does not necessarily correspond to the maximum-thrust operating point.

Flight endurance was evaluated using both measured flight duration and a current-based estimate. The usable battery capacity was calculated as $C_{usable} = C_{rated} \times DOD$, where C_{rated} is the battery capacity and DOD is the selected allowable depth of discharge. Estimated flight time was then calculated as $t_{est} = C_{usable} / I_{flight,avg}$, where $I_{flight,avg}$ is the average current drawn by the complete UAV during flight. A usable capacity below the rated battery capacity was used to avoid fully discharging the lithium-polymer battery. Because current demand varies during takeoff, hover, maneuvering, and landing, the measured flight duration was used as the primary measure of endurance, while the calculated flight time provided a basis for comparison.

3.4 Generative Design Methodology

Autodesk Fusion 360 was used to develop lightweight generatively designed UAV arms and landing gear. Separate studies were performed for each component because of their different functions and loading conditions. The UAV arms transfer motor-generated loads to the central frame during flight, while the landing gear supports the UAV during ground contact and landing.

For each study, the design space was defined using preserved geometry, obstacle geometry, and a starting shape. Preserved geometry identified regions that were required to remain unchanged, such as mounting and attachment locations, while obstacle geometry-maintained clearance for fasteners, wiring, motors, and adjacent components. The starting shape defined the region within which material could be generated or redistributed. Loads, constraints, and symmetry conditions were then applied to represent the primary operating conditions of each component.

PETG and PAHT-CF were evaluated separately to compare a commonly used thermoplastic with a carbon-fiber-reinforced engineering material. FOS of 3 and 5 were considered to evaluate the influence of structural requirements on the resulting geometry and mass. A FOS of 3 was selected to provide a balance between structural reliability and mass reduction, while a FOS of 5 represented a more conservative design condition. These FOS also provided additional allowance for uncertainties associated with FFF, including print orientation, interlayer bonding, internal defects, and variability in mechanical properties. A minimum buckling load multiplier of 2 was specified, requiring the predicted critical buckling load to be at least twice the applied design load.

After the geometry, boundary conditions, material properties, and structural requirements were defined, Fusion 360 generated multiple design outcomes. The outcomes were evaluated based on structural performance, mass, preservation of required mounting locations and clearances, and suitability for FFF manufacturing. Designs containing excessively thin sections, complex surfaces, or other features considered impractical to manufacture were excluded from further consideration.

3.4.1 UAV Arm Design

The UAV-arm design space was established by preserving the central-frame attachment and motor-mounting regions, as shown in Figure 18. These regions maintained the original mounting-hole locations and interfaces required to connect the arm to the UAV frame and motor. The remaining geometry between these regions provided the design space for material redistribution.

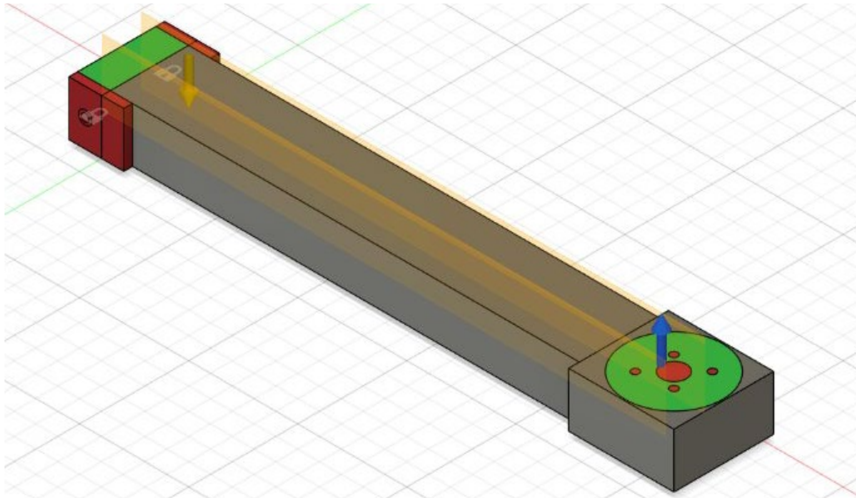

Figure 18: Generative-design space for UAV arm

Figure 19 depicts the preserved and obstacle geometries used in the arm study. The green regions represent the preserved geometry, including the frame connection and motor mount, while the red regions represent obstacle geometry used to maintain clearance for fasteners, wiring, the motor, and adjacent components. The surrounding starting shape defined the volume available for material generation.

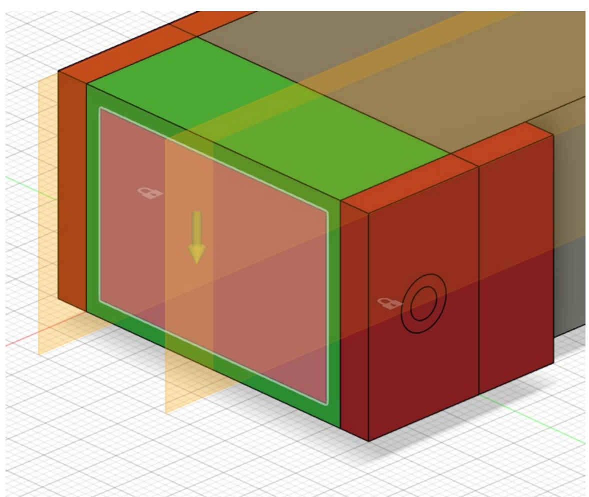

Figure 19: Preserved and obstacle geometry for UAV arm

A fixed constraint was applied to the mounting-hole surfaces at the central-frame connection to represent the bolted attachment of the arm to the UAV, as illustrated in Figure 20.

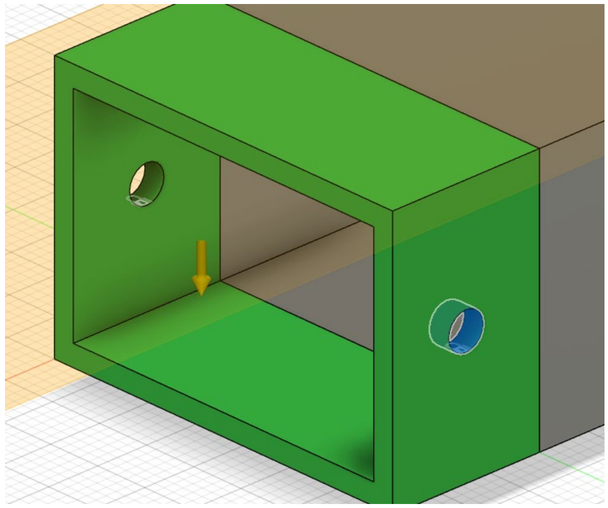

Figure 20: Fixed constraints applied to UAV arm

An upward force of 15 N (3.37 lbf) was applied at the motor-mounting region, as depicted in Figure 21, to represent the thrust generated by the motor–propeller system. This load was selected based on the experimentally measured maximum thrust of approximately 15.79 N (3.55 lbf) and was rounded to 15 N for use as a representative loading condition. Together, the fixed-frame connection and motor thrust represented the primary bending condition experienced by the arm during flight.

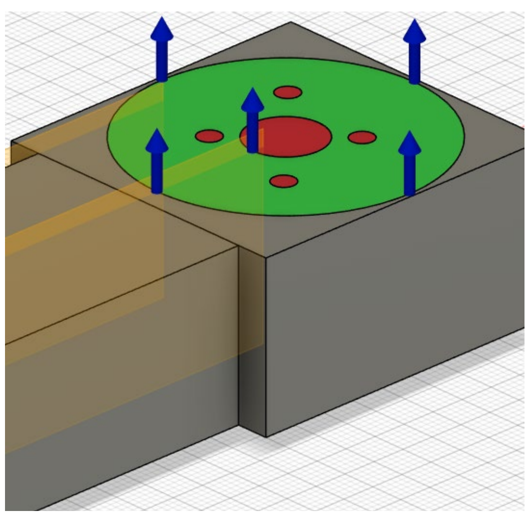

Figure 21: Motor-thrust 15 N (3.37 lb_f) load applied to UAV arm

A symmetry condition, illustrated in Figure 22, was applied to the arm to produce balanced geometry about the selected planes. With the design space, loads, constraints, and symmetry conditions established, the generative-design study was performed using the materials and structural requirements defined previously.

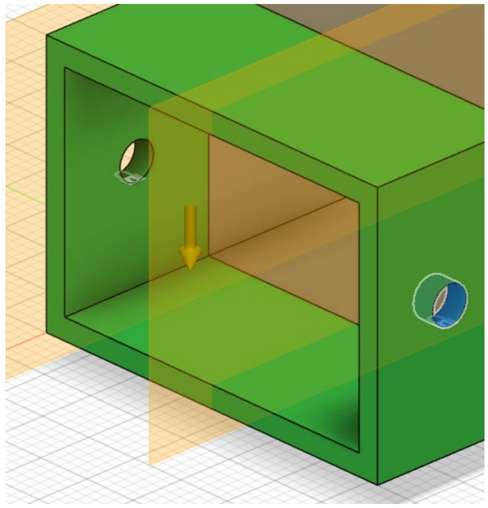

Figure 22: Symmetry conditions applied to UAV arm

3.4.2 UAV Landing-Gear Design

A separate generative-design study was performed for the landing gear to account for the loading conditions associated with supporting the UAV during ground contact and landing. The required frame-attachment locations and ground-clearance dimensions were established before defining the design space.

Figure 23 shows the geometry used for the landing-gear study. The green regions represent preserved geometry at the UAV-frame connections and lower ground-contact area, while the red cylindrical regions represent obstacle geometry used to maintain clearance around the fasteners. The starting shape between the preserved regions defined the volume available for material redistribution.

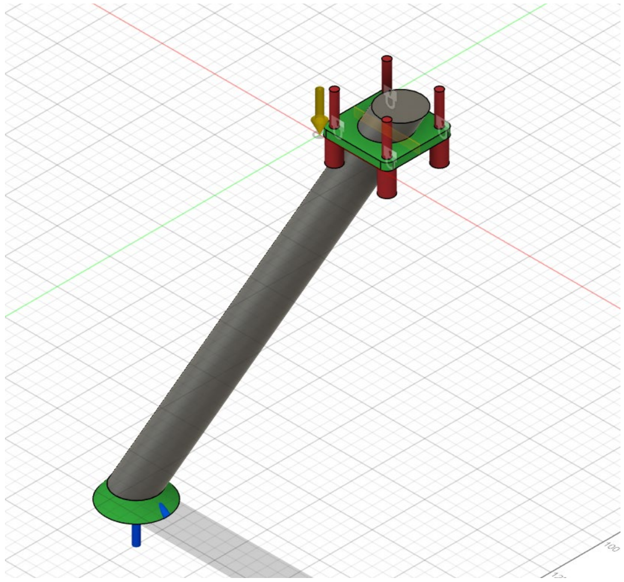

Figure 23: Generative design space for UAV landing gear

A fixed constraint was applied to the four mounting-hole surfaces on the upper portion of the landing gear to represent its attachment to the UAV frame, as depicted in Figure 24. A symmetry condition was also applied about the center plane to maintain balanced geometry while preserving the required attachment and ground-contact regions.

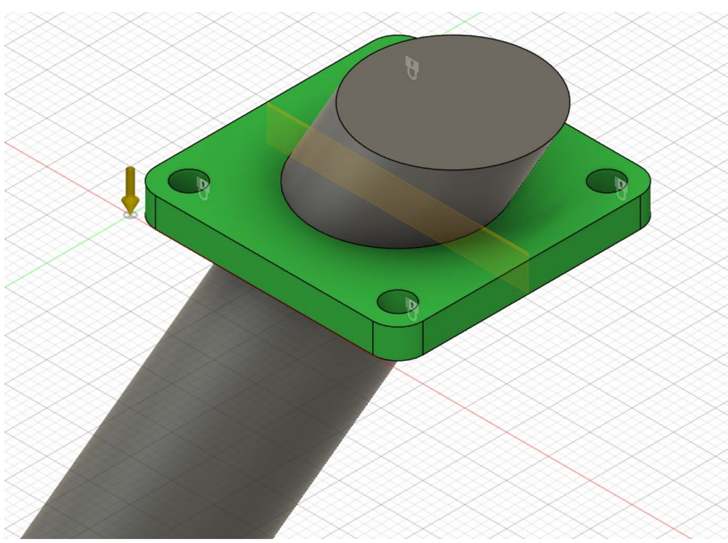

Figure 24: Fixed constraints and symmetry condition for UAV landing gear

The average vertical landing-impact force carried by each landing-gear member was estimated using an energy-based relationship:

$$F_{\text{vertical}} = \frac{mg}{3}(1 + \frac{h}{s})$$

where F_{vertical} is the average vertical force carried by each of the three landing-gear members, m is the 3.814 kg (8.408 lb) aircraft mass, g is gravitational acceleration, h is the assumed landing drop height, and s is the stopping or landing-gear deformation distance. Substitution of h = 0.052 m (52 mm) and s = 0.010 m (10 mm) yielded approximately 77.3 N (17.38 lbf) per landing-gear member, which was represented as 77 N (17.31 lbf) in the design analysis. The 52 mm drop height corresponded to an impact velocity of approximately 1.01 m/s (3.31 ft/s) and was selected to represent a minor hard landing rather than a severe impact. The force was applied vertically at the contact region shown in Figure 25, while the angled member geometry produced the corresponding axial and bending responses.

Two forces were applied to the lower contact region of the landing gear. The 77 N (17.31 lbf) vertical force represented the primary landing-impact load. A second force of 30 N (6.74 lbf), oriented at 120° within the Fusion 360 load definition, represented off-axis loading associated with uneven ground contact or a slightly tilted landing. The nonvertical load was approximately 39% of the vertical load:

The 30 N force was an assumed comparative design load rather than an experimentally measured impact force. It was included to prevent the generative-design process from producing a landing-gear component suited only to ideal vertical landings. Together, the two applied forces allowed the landing gear to be evaluated under both vertical and nonvertical loading conditions, as depicted in Figure 25.

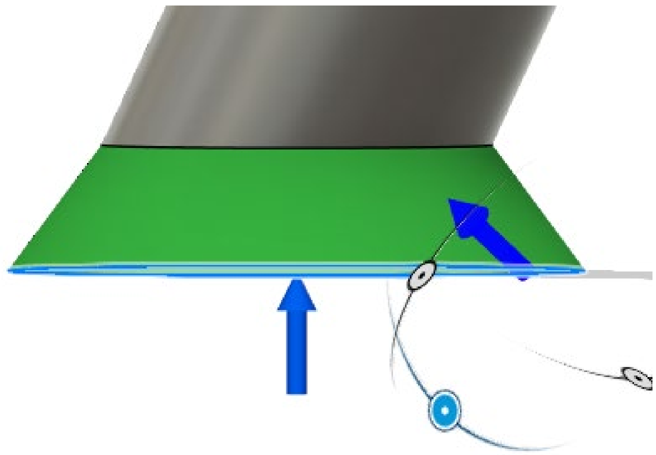

Figure 25: Loading conditions applied to UAV landing gear

The landing-gear generative-design study was then performed using the same material options, FOS, buckling requirement, and outcome-selection criteria established for the UAV-arm study. Using consistent design requirements allowed the effects of component geometry and loading conditions to be evaluated without repeating the overall generative-design procedure.

3.5 Finite Element Analysis

Following the generative-design studies, finite element analysis (FEA) was performed in Fusion 360 to evaluate the structural performance of the selected UAV-arm and landing-gear outcomes. Static stress analyses were performed for both the arm and landing gear to determine the von Mises stress, displacement, FOS, and buckling behavior of each component. The UAV arm and landing gear were analyzed separately because of their different geometries, constraints, and loading conditions; however, the mesh parameters were kept the same.

The finite element mesh used parabolic elements with curved mesh elements enabled. The average element size was specified as 10% of the model size, with a minimum element size of 20% of the average size. The maximum adjacent mesh-size ratio and maximum aspect ratio were set to 1.5 and 10, respectively, and the maximum turn angle on curved surfaces was 60°.

Adaptive mesh refinement was not applied. A contact tolerance of 0.10 mm was used, and automatic removal of rigid body modes was disabled.

The material response was assumed to be linear elastic, and geometric nonlinearity was not included. Where applicable, experimentally determined mechanical properties, such as elastic modulus, apparent Poisson's ratio, yield strength, and shear modulus, were used to represent the additively manufactured materials. These material properties are described in the results section in Chapter IV.

3.5.1 UAV Arm Model and Boundary Conditions

FEA was performed on four UAV-arm outcomes representing combinations of PETG and PAHT-CF with required FOS of 3 and 5, as summarized in Table 7. Each generated geometry was imported into the simulation workspace and analyzed using the corresponding material properties.

The UAV arm was modeled as a cantilever structure to represent its attachment to the central frame. A fixed constraint was applied to the frame-attachment region where the arm was secured to the frame by screws. The constraint restricted translation in all three directions U_x, U_y, and U_z, representing the restraint provided by the mechanical connection.

Table 7: UAV-arm finite element analysis cases

Case	Material	FOS
1	PETG	3
2	PETG	5
3	PAHT-CF	3
4	PAHT-CF	5

A force of 15 N (3.37 lbf) was applied to the upper surface of the motor-mounting region to represent the thrust generated by the motor and propeller. The force was applied in the positive z-direction and distributed across the motor-mount surface. Gravitational loading was also included using an acceleration of 9.807 m/s^2 in the negative z-direction.

Bonded contact was assumed between the arm and the adjoining attachment section. The screws and other attachment hardware were not explicitly modeled; instead, their restraining effect was represented by the fixed constraint applied at the frame-attachment region.

(a) (b)

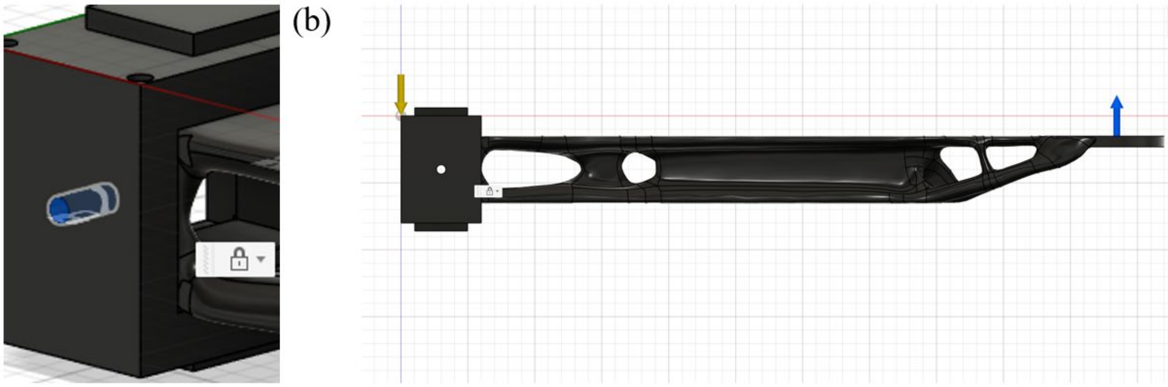

Figure 26: Boundary conditions of UAV arm analysis(a) fixed condition on screw hole (b) forces applied to the cantilever beam configuration

A finite element mesh was generated independently for each arm geometry. The models were discretized using a solid element type, with a global element size of approximately 10% of the model size. A total of 36739 elements and 62687 nodes were used in the study. The maximum von Mises stress, maximum displacement, and minimum FOS were recorded for each arm configuration. The locations of maximum stress and displacement were also examined to identify critical regions of the generated geometry.

3.5.2 UAV Landing Gear Model and Boundary Conditions

FEA was similarly performed on the selected landing-gear outcomes using the material properties associated with each generative-design case. As stated previously, fixed constraints were applied to the ends at the upper frame-attachment locations to represent the connection between the landing gear and UAV frame. A vertical force of 77 N (17.3 lbf) was applied vertically to represent the primary load transferred through the landing gear. An additional force of 30 N (6.75 lbf) was applied at an angle of 120° to represent off-axis loading associated with uneven ground contact or an angled landing. Chapter IV presents and discusses the numerical findings.

(a) (b)

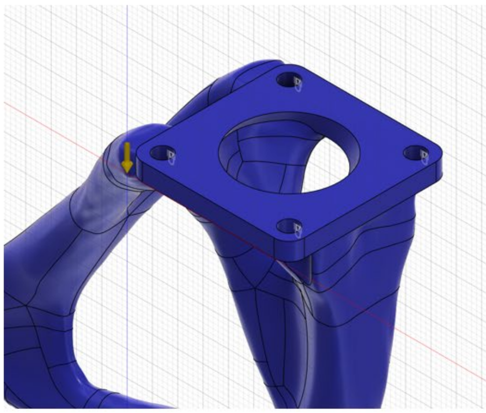

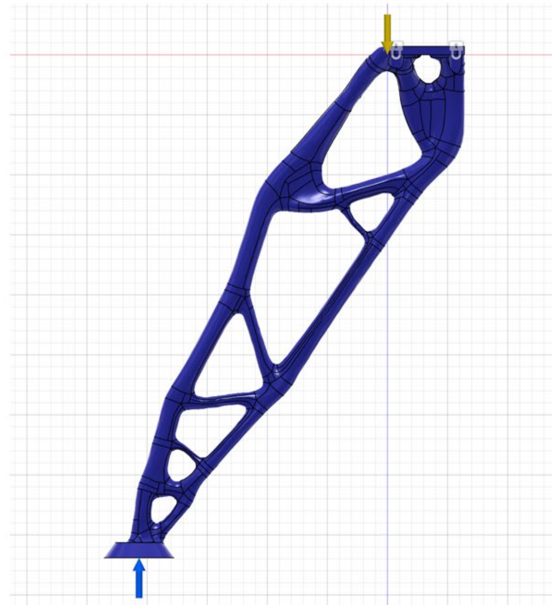

Figure 27: Boundary conditions of UAV landing-gear analysis(a) fixed condition on screw hole (b) forces applied to the beam configuration

3.6 3D-Printed Component Manufacturing

Following finite element analysis, the UAV-arm and landing-gear designs that satisfied the established structural and manufacturability requirements were selected for fabrication. The final geometries were prepared in Fusion 360 and exported as STL files for processing in Bambu Studio. Each component was positioned on the build plate according to the selected print orientation, and support structures were added where required to accommodate overhanging features. Figure 28 shows the UAV arm positioned and sliced in Bambu Studio with the required support structures.

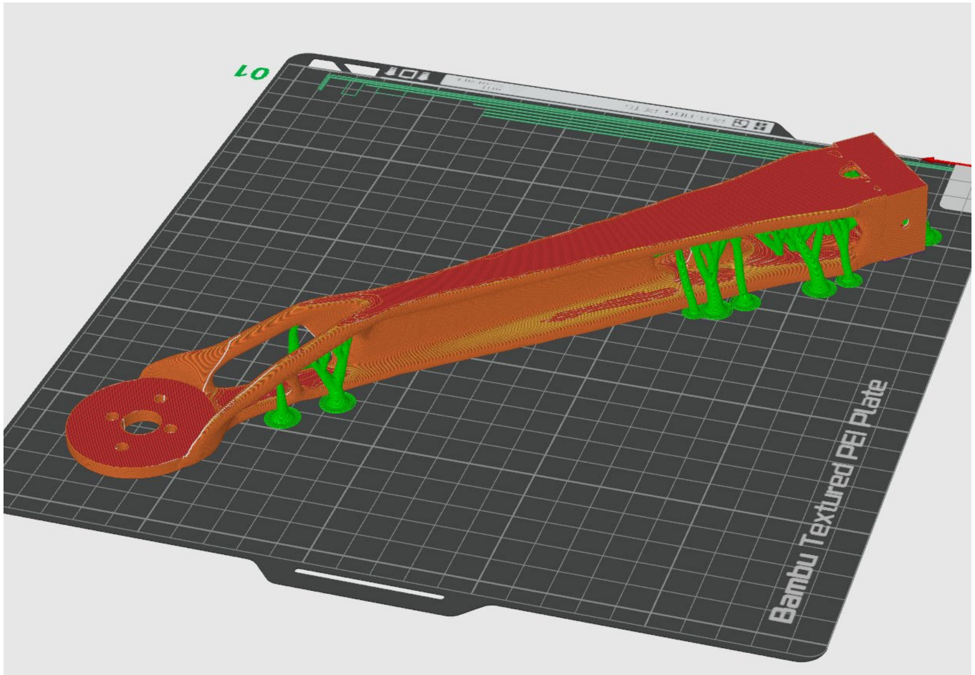

Figure 28: UAV arm prepared for additive manufacturing in Bambu Studio

Printing parameters were assigned according to the selected material and were maintained between the UAV arm and landing gear when the same material was used. Table 8 summarizes the primary printing parameters used for PAHT-CF and PETG.

Table 8: 3D printing parameters

Parameter	PAHT-CF	PETG
Print Orientation	X, Y, Z	X, Y, Z
Infill Density	20%	50%
Infill Pattern	Rectilinear	Rectilinear
Layer height	0.24 mm (0.0094 in)	0.16 mm (0.0063 in)
Wall loops	4	4
Nozzle Diameter	0.60 mm (0.024 in)	0.40 mm (0.016 in)
Nozzle Temperature	290°C (554°F)	255°C (491°F)
Bed Temperature	100°C (212°F)	70°C (158°F)
Dry Time	16 hrs	N/A
Dry Temperature	70°C (158°F)	N/A

After slicing, the files were transferred to the 3D printer for fabrication. Upon completion, the components were removed from the build plate, and support material was removed where necessary. Each component was visually inspected for warping, inadequate layer bonding, incomplete features, and other observable printing defects before assembly and subsequent evaluation.

3.7 Chapter Summary

Chapter III described the experimental and computational methodology used to develop the proposed hexacopter UAV. The methodology began with the selection, fabrication, and mechanical characterization of candidate 3D-printing materials through tensile, compression, and torsion testing under selected manufacturing and post-processing conditions. The resulting material properties provided experimental inputs for the structural design and analysis of the UAV components. Propulsion and control components were then selected, and thrust and current testing was performed to evaluate the propulsion system and establish the performance requirements of the hexacopter.

Using the material properties and UAV loading requirements, generative-design studies were performed to develop lightweight UAV arms and landing gear while maintaining the required mounting interfaces, clearances, and structural criteria. The selected outcomes were subsequently evaluated through finite element analysis to assess stress, displacement, FOS, and buckling behavior. Cyclic loading was also used to experimentally evaluate the UAV arm under repeated motor-induced loading. Finally, the selected components were prepared and manufactured using material-specific FFF parameters. Together, these methods provided the experimental, numerical, and manufacturing framework used to evaluate the proposed UAV design. The results obtained from these procedures are presented and discussed in Chapter IV.

CHAPTER IV

EXPERIMENTAL AND SIMULATION RESULTS

4.1 Material Testing Results

4.1.1 Tensile Test Results

Tensile testing was conducted to compare the mechanical behavior of the investigated materials under the manufacturing conditions described in Chapter III. The results were evaluated based on engineering stress–strain behavior, ultimate tensile strength, elastic modulus, and strain at failure. Because testing was completed in multiple experimental stages, not every material was evaluated at every infill density, print orientation, or post-processing condition. Comparisons were therefore made at matching conditions where possible, while trends within individual materials were evaluated using their respective test conditions.

Table 9 summarizes the tensile properties obtained at the investigated infill densities – each containing a total of 3-5 specimens depending on the set. Most materials were evaluated at 20%, 40%, and 60% infill, whereas PETG-CF was tested at 20%, 50%, and 70% as part of the staged experimental program.

Table 9: Mean mechanical properties of tensile experiments

Material	Number of Specimens	Infill Density (%)	Mean Elastic Modulus (MPa)	Mean Ultimate Tensile Strength (MPa)	Mean Elongation at Failure (%)
PETG	5	20	487	32.3	8.83
PETG	5	40	511	34	9.54
PETG	5	60	542	36.8	8.81
PLA-CF	5	20	753	23.5	5.28
PLA-CF	5	40	820	25.4	6.25
PLA-CF	5	60	843	27.7	6.41
PA6	5	20	1050	44.5	17.7
PA6	5	40	1110	46.5	18.8
PA6	5	60	1130	49.6	18.4
PCTG	5	20	422	25.5	13.2
PCTG	5	40	427	25.9	11.1
PCTG	5	60	457	28.4	11.6
PAHT-CF	5	20	1230	47.3	11.1
PAHT-CF	5	40	1370	52.5	11.3
PAHT-CF	5	60	1490	56.7	11.5
PETG-CF	5	20	594	27	13.7
PETG-CF	5	50	619	27.3	20.4
PETG-CF	5	70	625	27.3	16

Figure 29 compares representative engineering stress–strain curves at 20% infill. PAHT-CF exhibited the highest ultimate tensile strength, with a mean of 47.3 MPa, followed closely by PA6 with a mean of 44.5 MPa. PA6 had the greatest strain before failure, indicating greater ductility under the tested conditions. PETG achieved a mean yield strength of 32.3 MPa, while PETG-CF, PCTG, and PLA-CF had means of 27.0, 25.5, and 23.5 MPa, respectively. Thus, the 20% infill comparison identified PAHT-CF as the strongest material and PA6 as the most ductile among the configurations presented.

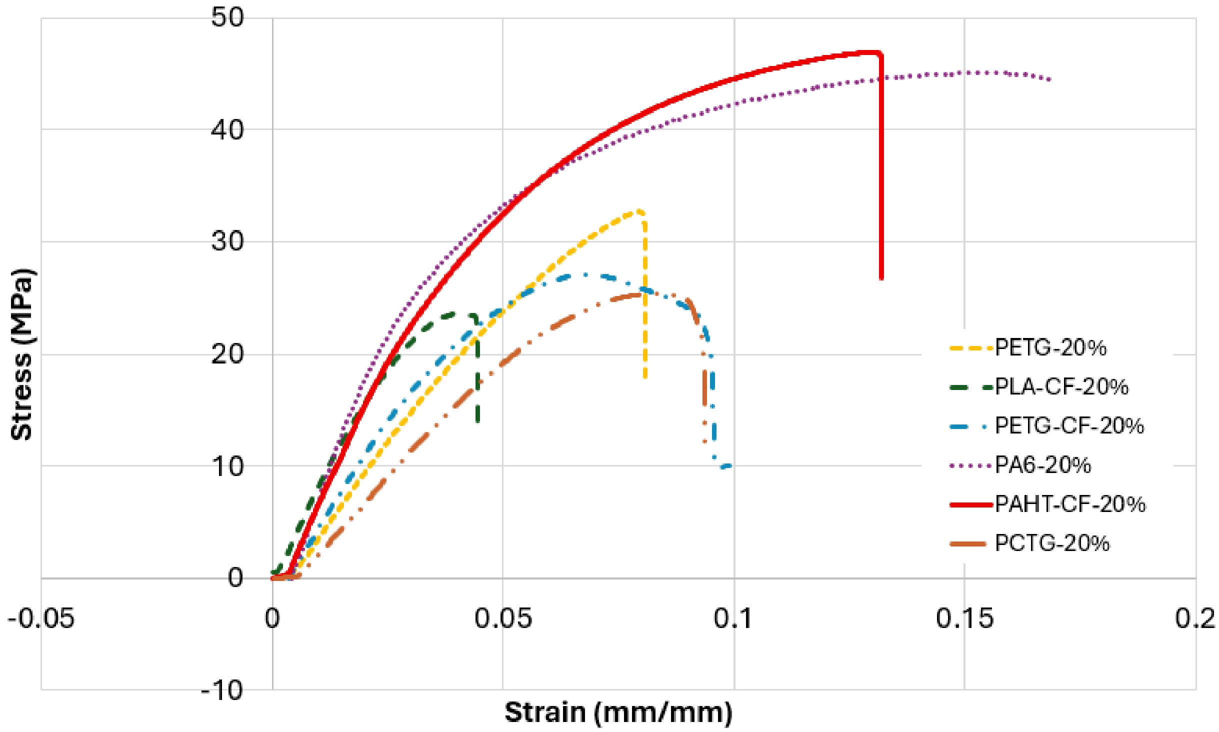

Figure 29: Engineering Stress–Strain response for selected specimens at 20% infill

The influence of infill density on ultimate tensile strength is shown in Figure 30. PAHT-CF increased from a mean of 47.3 MPa at 20% infill to a mean of 56.7 MPa at 60%, corresponding to an increase of approximately 20%. PA6 similarly increased from a mean of 44.5 to 49.6 MPa, while PETG, PLA-CF, and PCTG exhibited smaller increases over the same infill range. In contrast, PETG-CF remained nearly constant with an approximate mean of 27 MPa between 20% and 70% infill. Increasing infill density therefore generally increased tensile strength, although the magnitude of the effect was material-dependent.

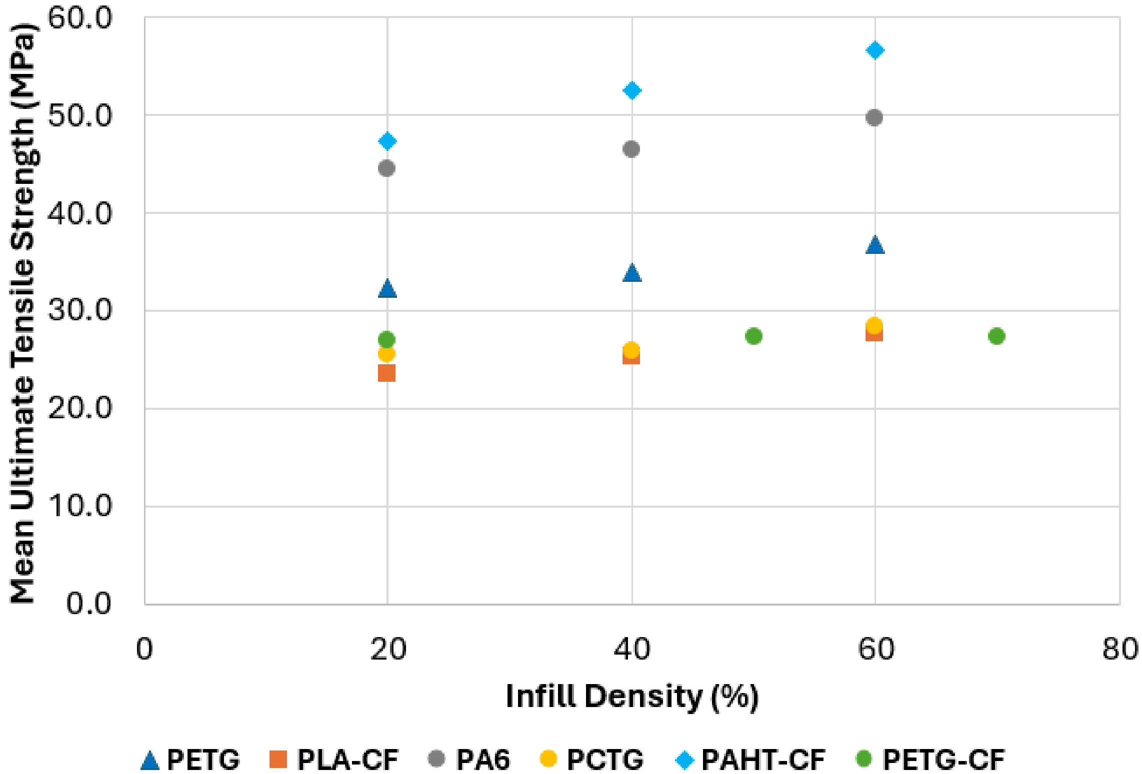

Figure 30: Mean ultimate tensile strength as a function of infill density

A similar trend was observed for elastic modulus, as shown in Figure 31. PAHT-CF exhibited the highest stiffness at each evaluated infill density, increasing from a mean of 1230 MPa at 20% infill to a mean of 1490 MPa at 60%, an increase of approximately 21%. PA6 exhibited the second-highest mean modulus, followed by PLA-CF. PETG-CF showed comparatively little change despite the increase from 20% to 70% infill. These results indicate that both material selection and infill density influenced tensile stiffness.

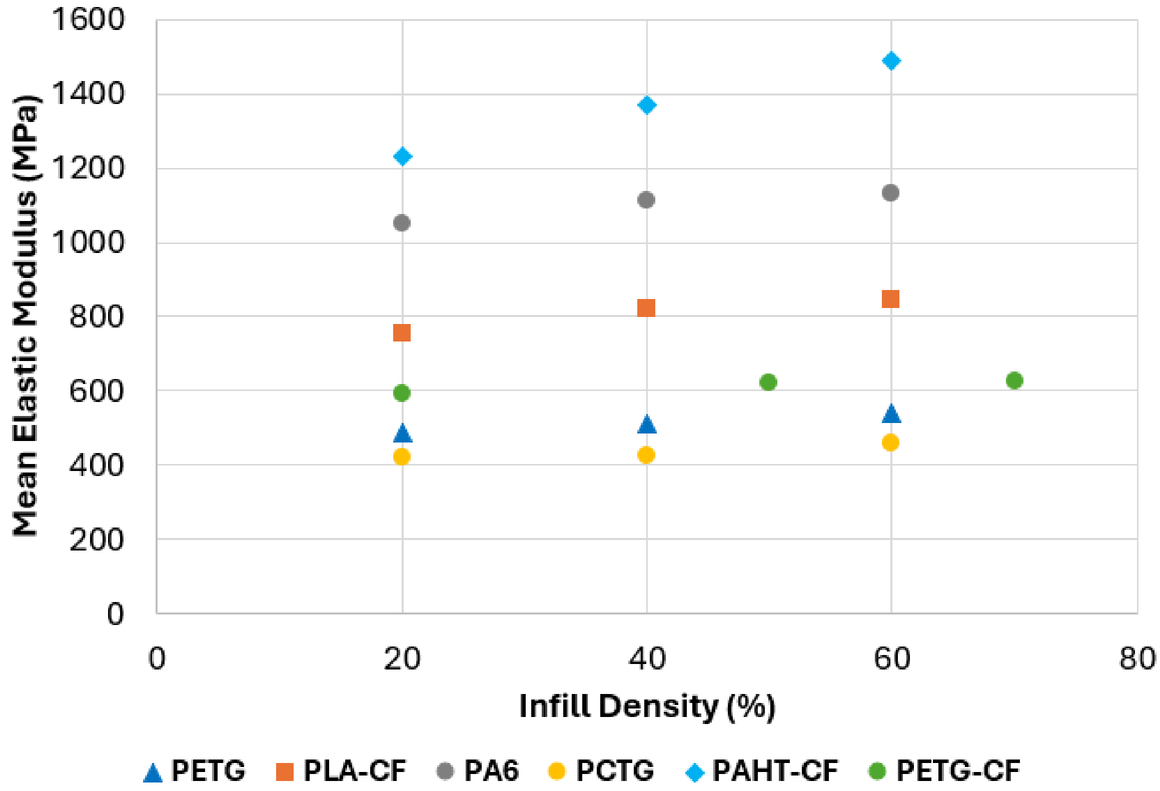

Figure 31: Mean elastic modulus as a function of infill density

Following the material and infill-density comparisons, the effect of annealing on PAHT-CF was evaluated at 20% infill. As shown in Figure 32, annealing at 90°C for 16 h produced little change relative to the unannealed condition. Increasing the annealing temperature to 110°C for 16 h increased the mean ultimate tensile strength from an approximate mean of 47.3 to 52 MPa, corresponding to an improvement of approximately 10–11%. Under the conditions investigated, the higher annealing temperature therefore produced a measurable improvement in tensile strength.

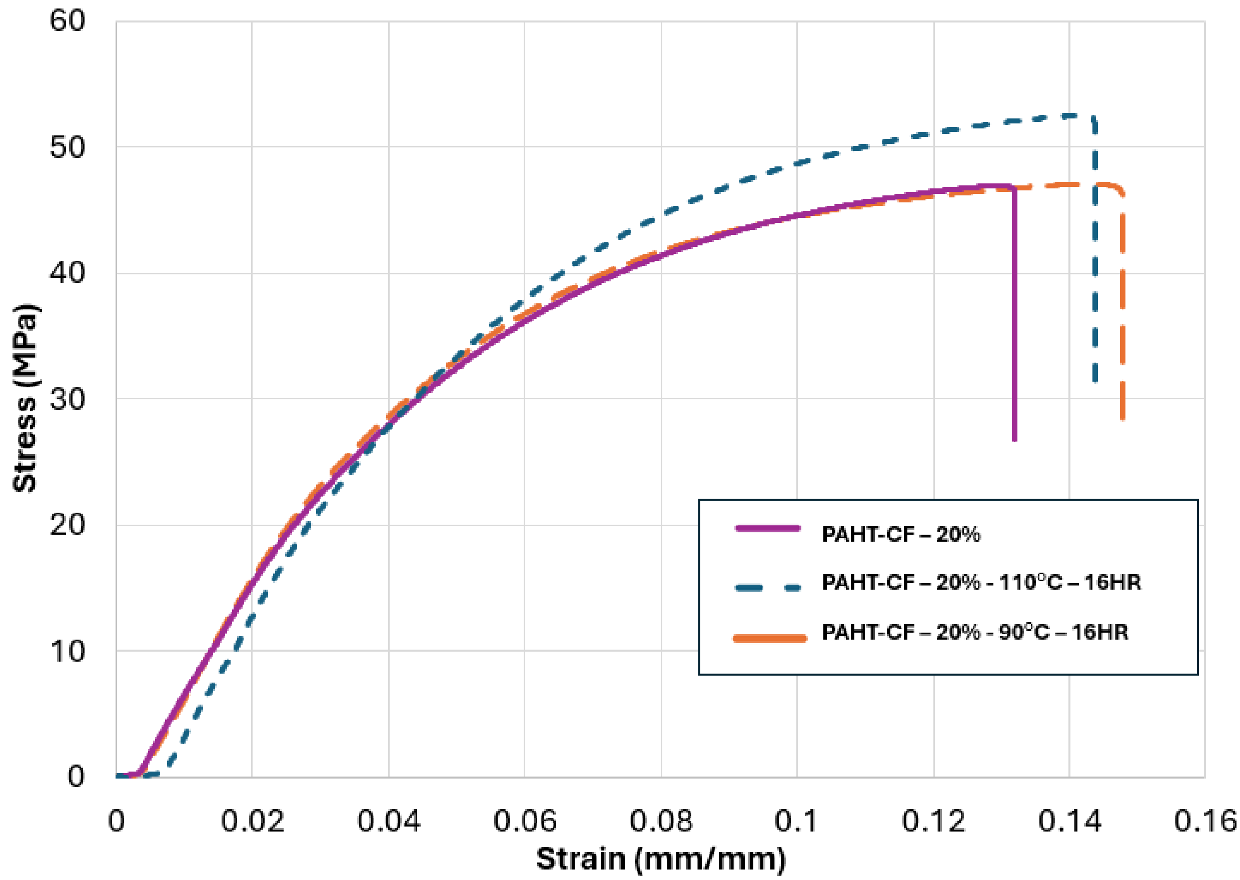

Figure 32: Effects of annealing on PAHT-CF specimens at 20% infill

Figure 33 compares selected PAHT-CF specimens manufactured using different print orientations and processing conditions. The side-oriented specimen produced the highest ultimate tensile strength, while the upright-oriented specimen produced the lowest. However, the standard, normal-oriented specimen was annealed at 110°C for 16 hours. Consequently, the observed differences in tensile behavior cannot be attributed solely to print orientation. The comparison nevertheless demonstrates that the manufacturing configuration influenced the tensile response and highlights the need to consider print orientation when applying measured properties to structural design. A controlled orientation comparison would require specimens produced using identical infill, annealing, and printing parameters.

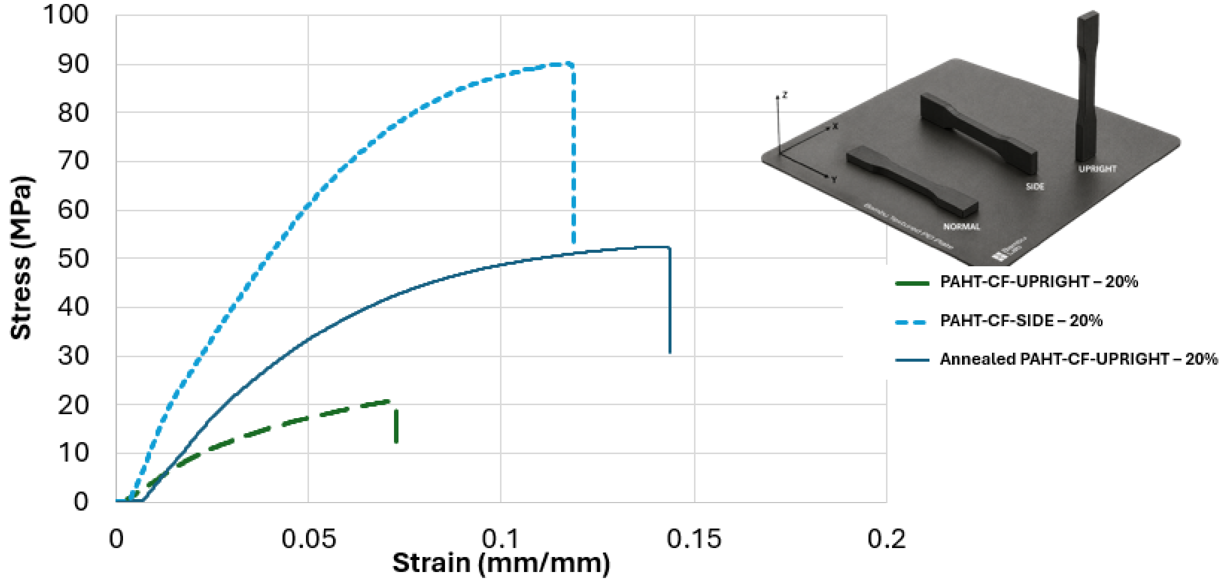

Figure 33: Tensile response of different print orientations for selected PAHT-CF specimens

Overall, PAHT-CF exhibited the highest tensile strength and elastic modulus among the investigated configurations, while PA6 exhibited greater elongation before failure. Increasing infill density generally improved tensile strength and stiffness, although the magnitude of the improvement varied by material. Annealing PAHT-CF at 110°C for 16 h further increased its tensile strength under the conditions investigated. The orientation results demonstrated the importance of deposited-layer alignment. Based on its combination of tensile strength and stiffness, PAHT-CF was selected for further structural characterization and evaluation in the generatively designed UAV components.

4.1.2 Compression Mechanical Properties

Compression testing was conducted to characterize the mechanical behavior of the investigated materials under compressive loading. Material type and infill density were evaluated based on compressive stress–strain behavior, compressive strength, compressive modulus, and apparent Poisson's ratio. Each experimental result included three samples per set or print configuration. The resulting properties were used to compare the tested material configurations and provide additional mechanical-property data for evaluating the UAV structural components.

Increasing the infill density increased the maximum recorded compressive stress from an approximate mean of 24.84 MPa to 42.31 MPa, as illustrated in Figure 34. The 80% infill maintained a higher compressive stress throughout most of the experiment. Figure 35 depicts the effect of infill density on the compressive behavior of selected PLA specimens. Increasing infill density raised the compressive mean stress from ~24.31 MPa to ~76.50 MPa. The significant separation between the curves demonstrates the strong influence of infill density on the compressive response of PLA. Overall, increasing infill density considerably improves compressive performance on both PETG and PLA under the testing conditions.

4.1.3 Effect of Infill Density on PLA and PETG

The compressive stress–strain behavior of PETG at 50% and 80% infill is presented in Figure 34. Increasing the infill density from 50% to 80% increased the maximum recorded compressive stress from approximately 24.84 MPa to 42.31 MPa. As shown by the curves in Figure 34, the 80% infill configuration maintained a higher compressive stress than the 50% configuration throughout most of the test.

The effect of infill density on the compressive behavior of PLA is presented in Figure 35. Increasing the infill density from 50% to 100% increased the maximum recorded compressive stress from approximately 24.31 MPa to 76.50 MPa. The substantial separation between the curves in Figure 35 demonstrates the strong influence of infill density on the compressive response of PLA. Together, they show that increasing infill density considerably improved the compressive performance of both PETG and PLA

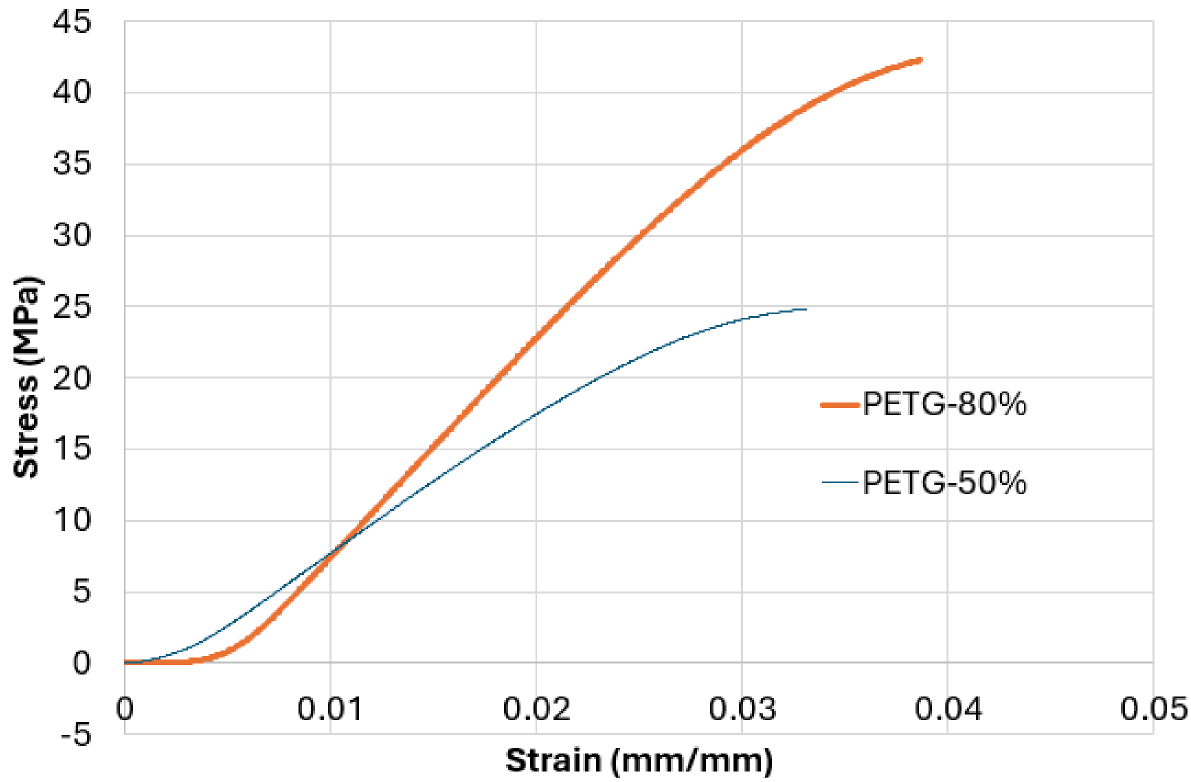

Figure 34: Effect of infill on compressive behavior of selected PETG specimens

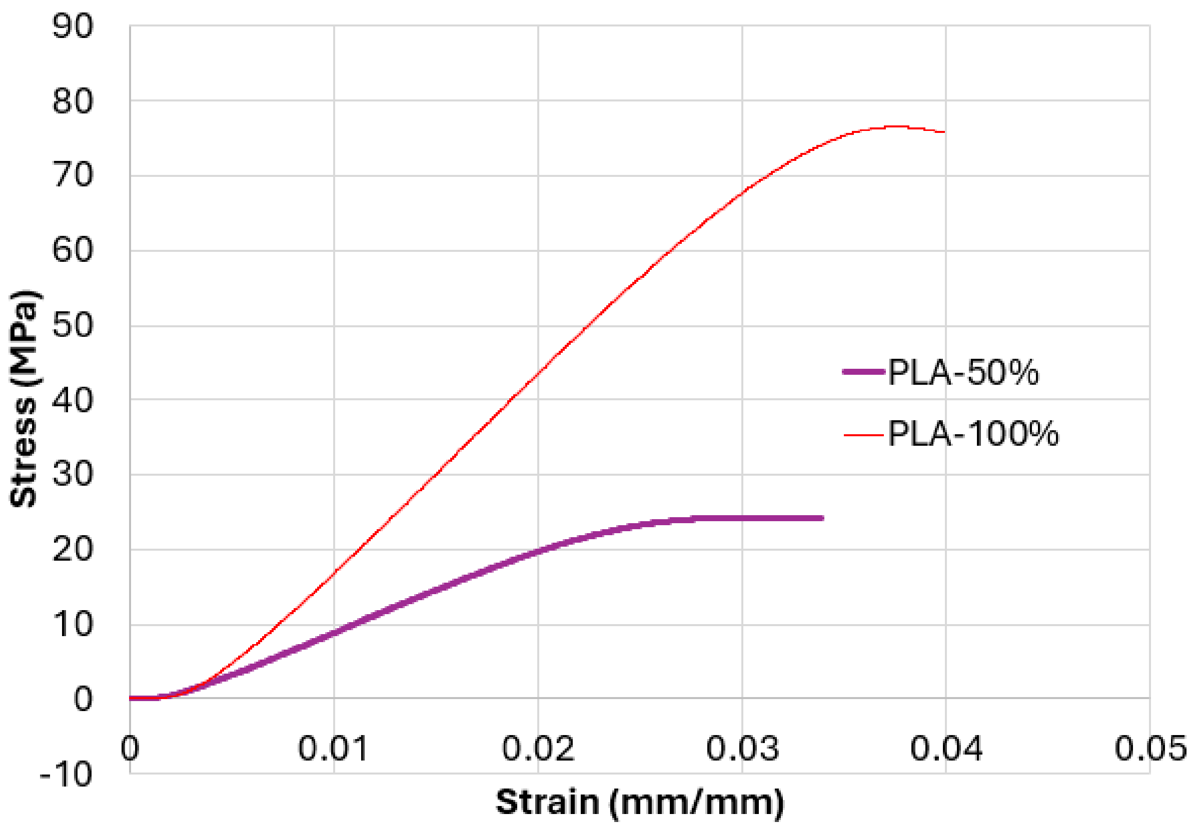

Figure 35: Effect of infill on compressive behavior of selected PLA specimens

The baseline material configurations are compared in Table 10. PLA at 100% infill had the highest recorded mean compressive stress (76.50 MPa), followed by PETG at 80% infill (42.31 MPa). However, untreated PAHT-CF had a mean of 32.74 MPa at only 20% infill, exceeding PLA and PETG at 50% infill (24.31 and 24.84 MPa, respectively). Although the configurations in Table 10 were not manufactured at identical infill densities, the results show that PAHT-CF provided favorable compressive resistance at a substantially lower infill density. This behavior is advantageous for weight-sensitive UAV components because lower infill can reduce material usage and structural mass.

Table 10: Maximum mean compressive stress for different material configurations

Material	Infill Density (%)	Processing Treatment	Maximum Mean Compressive Stress (MPa)
PLA	50	Standard	24.31
PLA	100	Solid	76.50
PETG	50	Standard	24.84
PETG	80	Standard	42.31
PAHT-CF	20	Untreated	32.74

The maximum recorded mean compressive stresses of the thermally treated PAHT-CF configurations are summarized in Table 11, while the stress–strain responses for selected specimens are presented in Figure 36. The specimens treated at 90°C for 12 hours and 120°C for 9 hours produced the highest mean maximum recorded stresses of 35.81 and 35.88 MPa, respectively. Compared with the untreated mean value of 32.74 MPa reported in Table 10.

As shown in Figure 36, treatment at 50°C for 5 hours had the lowest mean maximum recorded stress (29.77 MPa). Treatments at 120°C for 5 hours and 150°C for 5 hours produced mean values of 34.52 and 33.99 MPa, respectively. The results for the current testing configurations indicate that the 90°C–12-hour and 120°C–9-hour treatments produced the most favorable compressive responses under the investigated conditions. However, because treatment duration and cooling method were not held constant, the results represent a preliminary trend rather than confirmation of an optimum annealing temperature.

Table 11: Maximum mean compressive stress of annealed PAHT-CF specimens

Material	Infill Density (%)	Annealing Heat Process	Maximum Mean Compressive Stress (MPa)
PAHT-CF	20	50°C for 5 hours	29.77
PAHT-CF	20	90°C for 12 hours	35.81
PAHT-CF	20	120°C for 5 hours	34.52
PAHT-CF	20	120°C for 9 hours	35.88
PAHT-CF	20	150°C for 5 hours	33.99

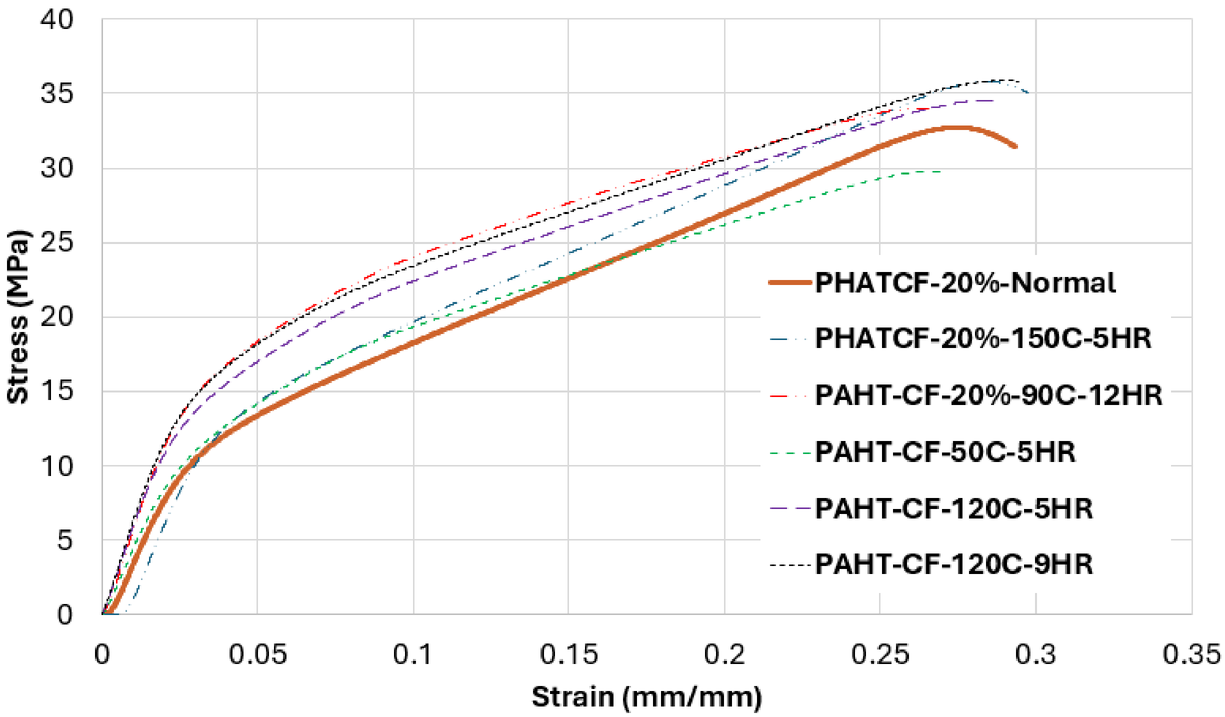

Figure 36: Annealing effect on heat treated specimens

The effect of print orientation on the compressive behavior of PAHT-CF is presented in Figure 37. Three specimens were printed at 60°, 45°, and normal orientations. Specimens printed at 60° exhibited a mean maximum compressive stress of 24.01 MPa, approximately 10% higher than the 21.84 MPa measured for specimens printed at 45°. The relatively small standard deviations, with the highest being 0.105 MPa for the 45° orientation, indicate consistent behavior within each orientation group. These results demonstrate that print orientation affected the compressive performance of PAHT-CF, which may be attributed to differences in the alignment of the deposited layers relative to the applied load.

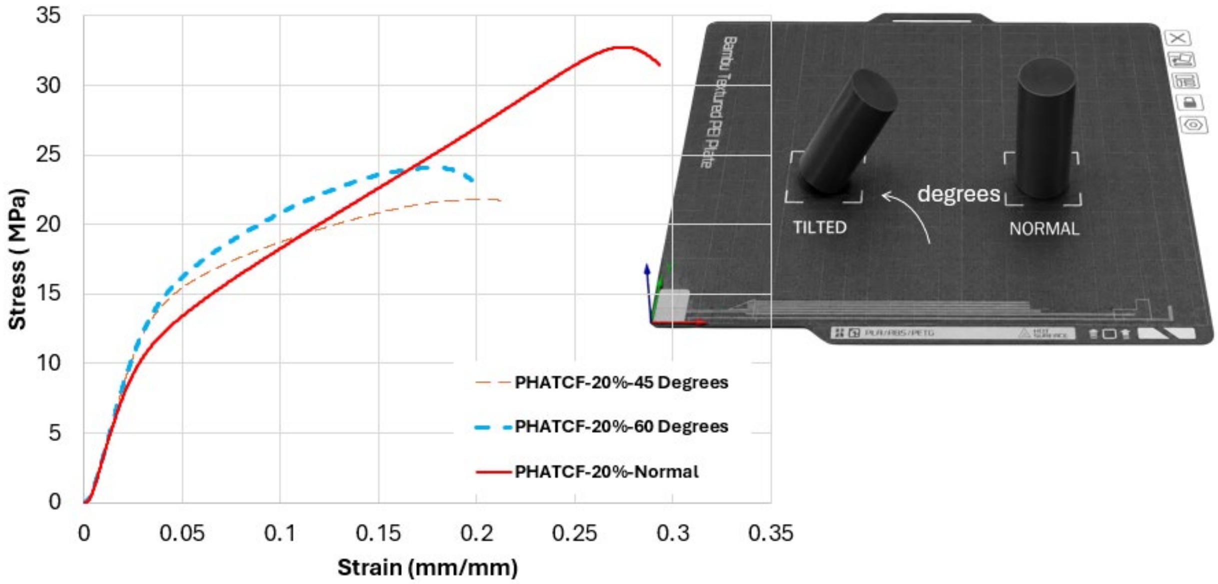

Figure 37: Effect of orientation on the compressive stress-strain behavior of PAHT-CF-20% at 20% infill

Figure 38 compares the apparent Poisson’s ratio values for three PAHT-CF heat-treated and untreated specimens. The thermally treated specimens at 90°C for 12 hours produced a higher apparent Poisson’s ratio than the untreated specimens. The heat-treated specimens were also more consistent, with a standard deviation of 0.012 compared with 0.026 for the untreated specimens. However, because the values were determined from specimen dimensions measured before and after compression, they characterize the overall deformation of the printed specimens and may include permanent deformation, barreling, and internal infill collapse. Therefore, as previously stated, the results should not be interpreted as intrinsic values, but rather apparent Poisson’s ratio values.

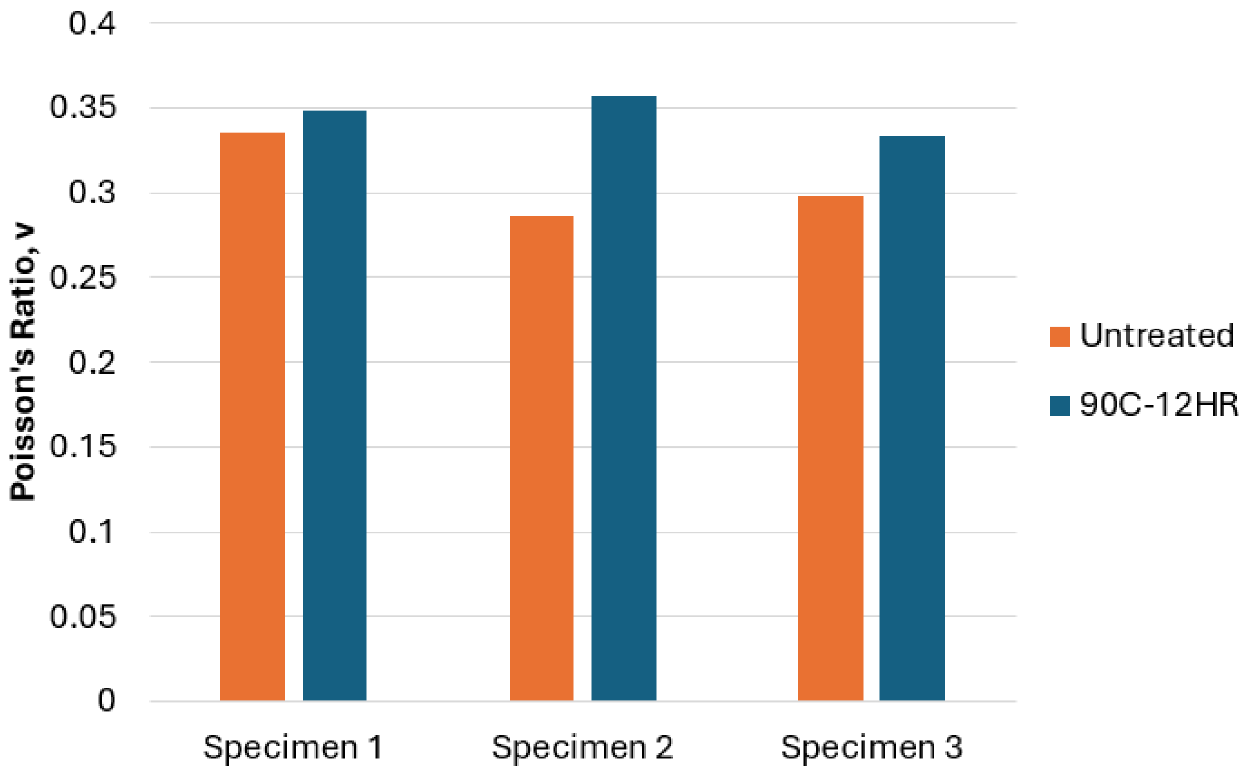

Figure 38: Effect of heat treatment on apparent Poisson's ratio for PAHT-CF

Overall, the compression results demonstrate that material selection, infill density, thermal treatment, and print orientation influenced the mechanical response of the tested specimens. Increasing infill density improved the compressive performance of PETG and PLA, with PLA at 100% infill producing the highest mean maximum compressive stress. However, PAHT-CF at only 20% infill exceeded the performance of both PLA and PETG at 50% infill, demonstrating favorable compressive performance at a substantially lower infill density. Selected thermal-treatment conditions further improved the response of PAHT-CF, while the orientation results confirmed that its compressive behavior was dependent on print direction. The apparent lateral-to-axial deformation measurements provided additional characterization of the printed material response. Combined with the tensile results, these findings support PAHT-CF as a suitable material for the lightweight UAV structure due to its favorable mechanical performance at relatively low infill density.

4.1.4 Torsion Experimental Results

Torsion testing was conducted to compare the shear response of PETG and PAHT-CF specimens manufactured at 20% infill. Nominal maximum surface shear stress and nominal shear strain were calculated from the measured torque and angle of twist using solid circular-specimen relationships. As previously stated, the reported shear modulus values are considered apparent torsional shear moduli because the specimens contained internal infill and the torque reader recorded in 0.1-N·m increments. They represent the response of the printed specimen configuration rather than the intrinsic bulk-material shear modulus.

As shown in Figure 39, PETG reached a maximum nominal shear stress of 18.92 MPa. The specimen underwent substantial torsional deformation, reaching a high shear strain before its recorded torque decreased near the end of the test. The apparent torsional shear modulus of PETG was approximately 190 MPa, calculated from the initial loading response. This value is consistent with the tensile-based estimate of approximately 183 MPa, calculated from the measured tensile modulus of 487 MPa using a Poisson's ratio of 0.33. The stepped portions of the curve resulted from the 0.1-N·m torque resolution of the torsion-testing machine and do not represent elastic behavior.

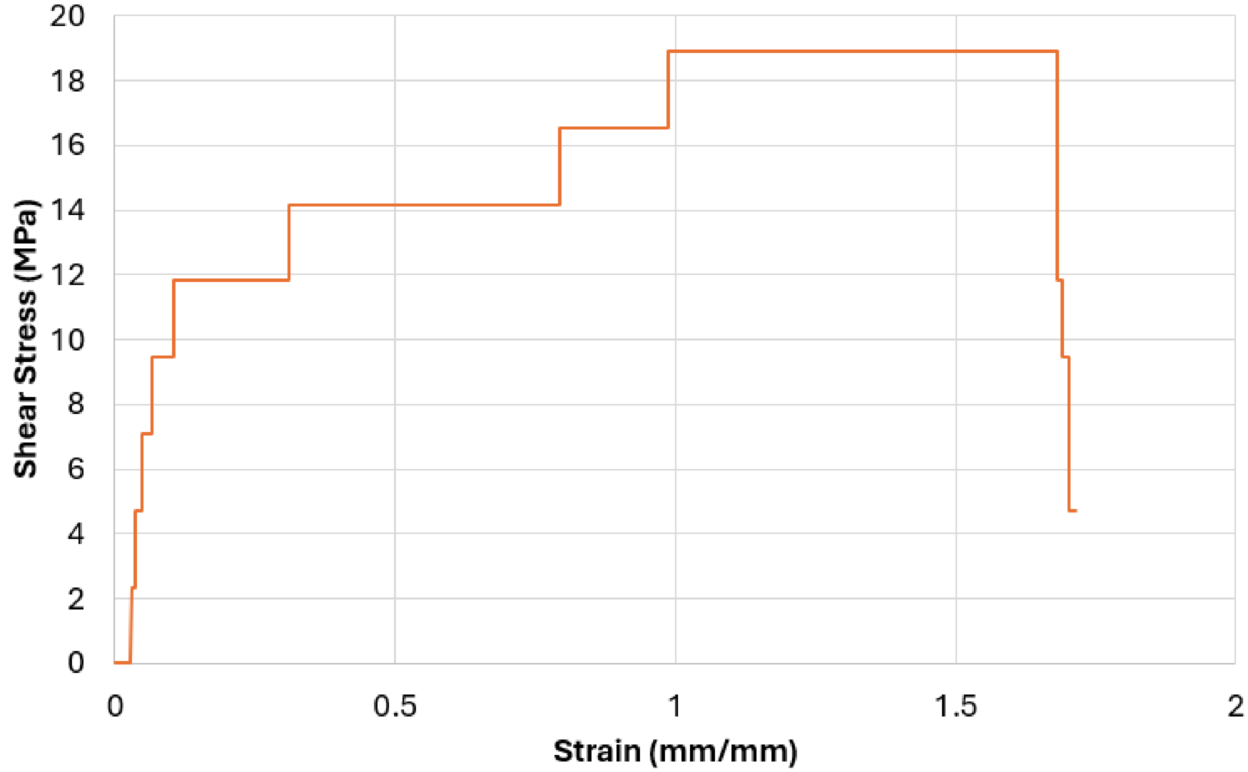

Figure 39: Torsion test results for a PETG – 20% infill specimen

Figure 40 shows that PAHT-CF reached a maximum nominal shear stress of 33.10 MPa. The apparent torsional shear modulus was approximately 599 MPa, obtained from the initial rising portion of the response using linear regression. PAHT-CF reached a higher torsional stress at a lower strain than PETG, indicating greater resistance to twisting deformation. The constant-stress region represents continued rotation while the recorded torque remained approximately constant; therefore, it was excluded from the shear-modulus calculation.

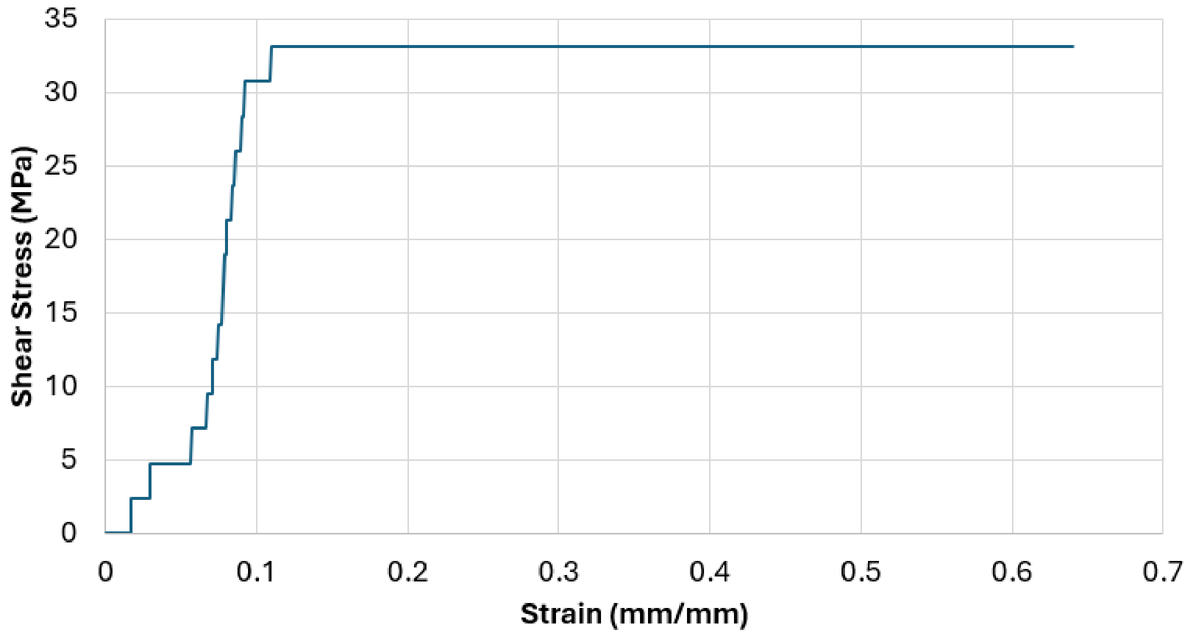

Figure 40: Torsion test results for a PAHT-CF – 20% infill specimen

Table 12 summarizes the tensile and torsional properties of the PETG and PAHT-CF specimens manufactured at 20% infill. PAHT-CF reached a maximum nominal shear stress of 33.10 MPa, compared with 18.92 MPa for PETG. This corresponds to about 75% increase in torsional stress capacity for the tested PAHT-CF configuration. PAHT-CF also produced an apparent torsional shear modulus of approximately 599 MPa, which was almost 215% greater than the 190 MPa measured for PETG. The higher apparent torsional stiffness and shear-stress capacity agree with the tensile results, in which PAHT-CF showed greater tensile strength and tensile modulus than PETG. Therefore, for the tested 20% infill specimens, PAHT-CF provided greater resistance to twisting deformation and is the more suitable material for the UAV arm application, where motor torque and maneuvering can introduce torsional loading.

Table 12: Summary of results for PETG and PAHT-CF at 20% infill

Material	Tensile Strength (MPa)	Tensile Modulus (MPa)	Maximum Shear Stress (MPa)	Apparent Torsional Shear Modulus (MPa)
PETG	32.3	487	18.92	190
PAHT-CF	47.3	1230	33.1	599

4.2 Propulsion Experiment Results

4.2.1 Thrust Performance

The single-motor thrust tests evaluated the thrust capability of the final six-motor hexacopter configuration. Thrust was measured at increasing throttle signals using the calibrated load-cell test stand described in Section 3.3. Figure 41 illustrates the thrust vs. throttle results for a measured single motor for each tested propeller configuration.

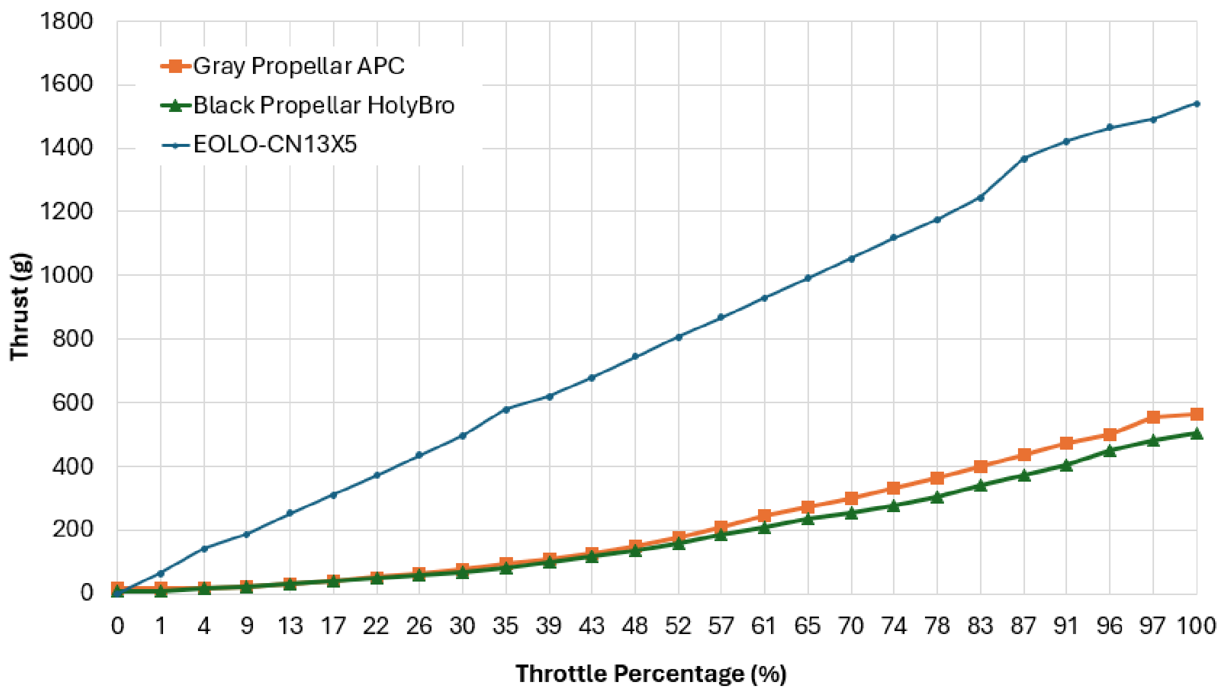

Figure 41: Measured thrust and propulsion-system performance

The measured single-motor thrust was multiplied by six to estimate the total thrust available from the hexacopter propulsion system. Using the baseline UAV mass of 3.814 kg, the total available thrust was used to calculate the thrust-to-weight ratio at each tested operating condition. A ratio of approximately 1 represents the minimum thrust required to maintain hover, whereas higher ratios provide additional thrust capacity for takeoff, climbing, maneuvering, and responding to disturbances. A thrust-to-weight ratio of 2 was used as the target design condition to provide adequate thrust reserve. The estimated six-motor thrust and corresponding thrust-to-weight ratios are summarized in Table 13.

Table 13: Estimated hexacopter thrust and thrust-to-weight ratios

Propeller	Current per Motor (A)	Thrust per Motor (g)	Estimated Total Thrust, 6 Motors (kgf)	T/W Ratio (Baseline Mass = 3.814 kg)	Meets T/W = 2?
Gray APC	9.16	556.18	3.34	0.87	No
Black Holy	7.00	480.73	2.88	0.76	No
EOLO CN 13 x 5	11.20	1610.00	9.66	2.53	Yes

The gray APC propeller generated 556.18 g of thrust per motor, corresponding to an estimated total hexacopter thrust of 3.34 kgf and a thrust-to-weight ratio of 0.88. The black Holy propeller generated 480.73 g per motor, resulting in an estimated total thrust of 2.88 kgf and a thrust-to-weight ratio of 0.76. Because both ratios were below 1, neither configuration provided sufficient thrust to support the baseline UAV mass of 3.814 kg.

In comparison, the EOLO CN 13 × 5 propeller generated 1,610 g of thrust per motor at full throttle, corresponding to an estimated total thrust of 9.66 kgf and a thrust-to-weight ratio of 2.53. Of the configurations tested, the EOLO CN 13 × 5 was the only propeller to exceed the target thrust-to-weight ratio of 2 and was therefore selected for the final hexacopter.

Although the EOLO CN 13 × 5 propeller provided the required thrust reserve, propulsion-system performance also depends on the electrical power required to generate that thrust. Therefore, current draw, power consumption, and thrust-to-power ratio were evaluated to determine the electrical performance of the selected propulsion configuration, as discussed in the following section.

4.2.2 Propulsion System Performance

The electrical performance of the selected EOLO CN 13 × 5 propeller configuration was evaluated at 50%, 80%, and 100% throttle. As depicted in Figure 42, the measured current increased with throttle, from 4.0 A per motor at 50% throttle to 11.2 A at 100%. The increase became more pronounced at higher throttle settings as additional electrical power was required to increase propeller speed and thrust.

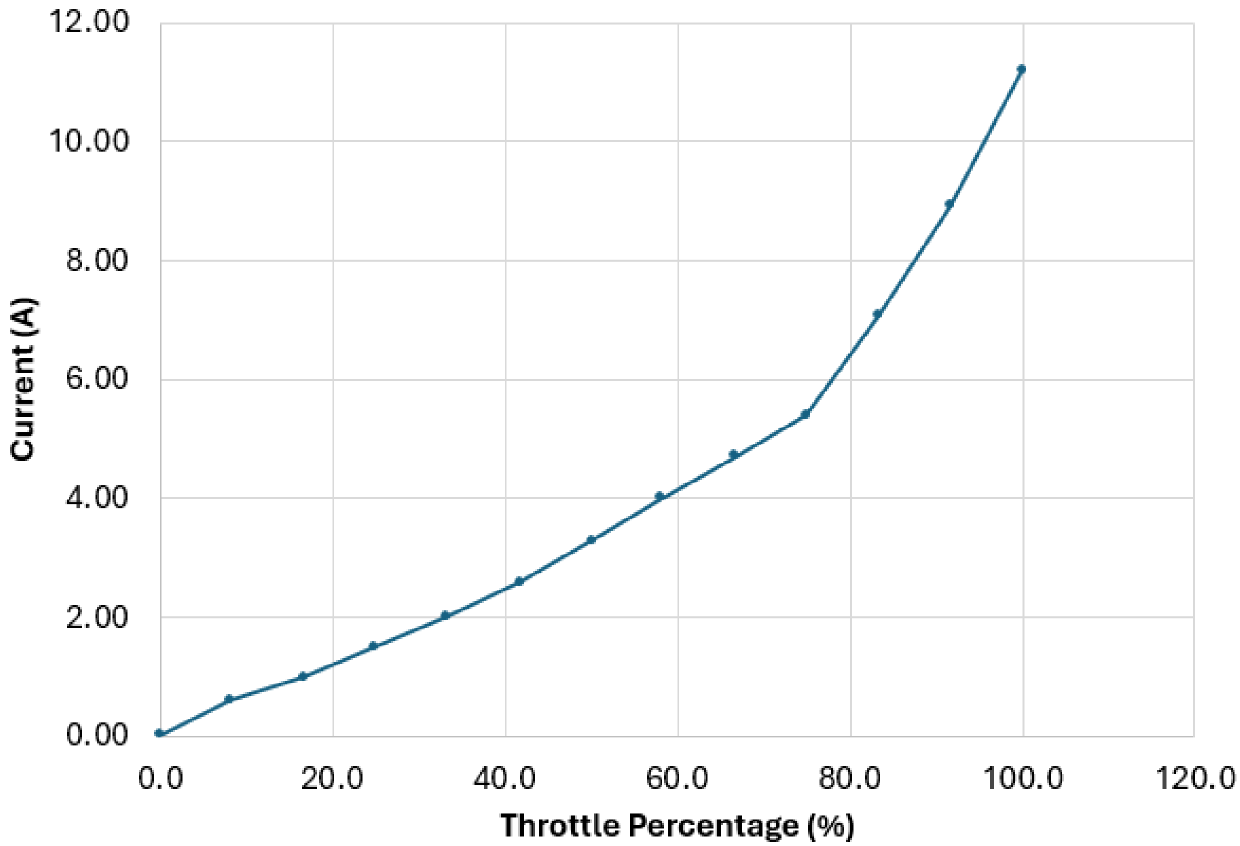

Figure 42: Measured current as a function of throttle

The corresponding thrust measurements are presented in Figure 43. Thrust increased from 800 g per motor at 50% throttle to 1,275 g at 80% and 1,610 g at 100%. The measured single-motor current was multiplied by six to estimate the total propulsion current of the hexacopter, and the corresponding electrical power and thrust-to-power ratio were calculated at each operating condition. These results are summarized in Table 14.

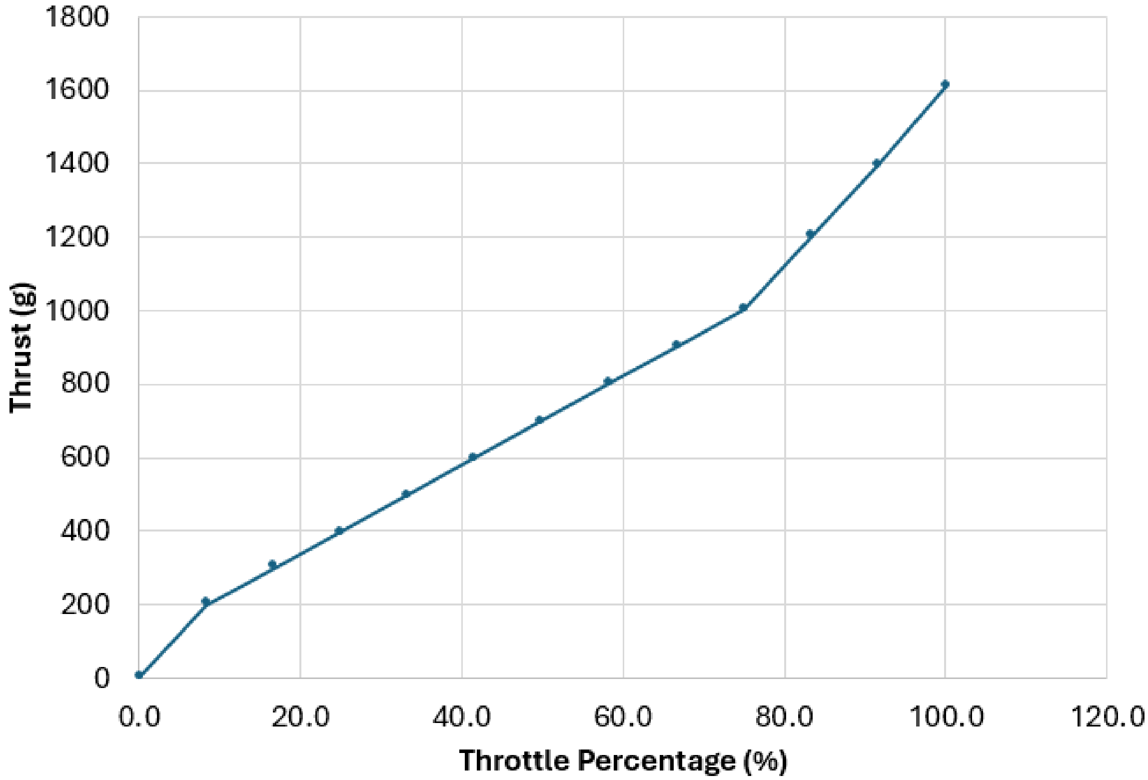

Figure 43: Measured thrust as a function of throttle

The thrust results followed a similar increasing trend. At the highest operating point, the configuration produced 1,610 g of thrust while drawing 11.20 A. The single-motor current was multiplied by six to estimate the total propulsion current of the hexacopter. Electrical power and thrust-to-power ratio were then calculated for each operating point. These results are summarized in Table 14.

Table 14: Electrical and thrust performance of the EOLO CN 13 × 5 propeller configuration

Throttle	Current per motor (A)	Estimated total propulsion current (A)	Total power (W)	Thrust per motor (g)	Thrust-to-power ratio (g/W)
50%	4.0	24.0	532.8	800	9.01
80%	8.2	49.2	1,092.2	1,275	7.00
100%	11.2	67.2	1,491.8	1,610	6.48

At full throttle, each motor generated 1,610 g of thrust while drawing 11.2 A. For the six-motor system, these values correspond to an estimated total thrust of 9.66 kgf, total propulsion current of 67.2 A, and electrical power of approximately 1.49 kW. The estimated current and power represent the propulsion system only and exclude the electrical demands of the flight controller, receiver, GPS, telemetry system, sensors, and other onboard electronics.

Although thrust increased with throttle, thrust-to-power ratio decreased from 9.01 g/W at 50% throttle to 7.00 g/W at 80% and 6.48 g/W at 100%. Thus, the highest tested throttle condition provided the greatest available thrust but required more electrical power per unit of thrust produced. Continuous operation at higher throttle settings would therefore increase battery demand and reduce flight endurance.

The EOLO CN 13 × 5 configuration provided the thrust required for the hexacopter while demonstrating the tradeoff between available thrust and electrical efficiency. The effect of this electrical demand on battery utilization and UAV endurance is evaluated in the following section.

4.2.3 Flight Endurance

Flight testing was conducted using the assembled hexacopter equipped with a 4S lithium-polymer battery. The designation 4S indicates that four battery cells were connected in series, producing a nominal battery voltage of 14.8 V. The battery had a rated capacity of 6,200 mAh, equivalent to 6.2 Ah, and a discharge rating of 100C. Battery capacity describes the amount of electrical charge available, whereas the C-rate describes how quickly the battery is theoretically capable of delivering that charge. A discharge rate of 1C would theoretically use the full battery capacity in 1 h, while a rate of 0.5C would require approximately 2 h. For the 6.2-Ah battery, a 100C rating corresponds to a theoretical maximum discharge current of 620 A. If this maximum current were drawn continuously, the battery would theoretically discharge in 1/100 of an hour, or 36s.

However, the 36-s value does not represent the UAV's expected flight time. It describes an extreme theoretical condition in which the battery continuously supplies its maximum rated current. During normal operation, the battery supplies only the current required by the motors, electronic speed controllers, flight controller, and other onboard components. This operating current is substantially lower than the battery's theoretical maximum current. Therefore, the 100C rating indicates the battery's ability to support high current demand and does not mean that the battery normally discharges at 620 A.

The hexacopter successfully remained operational throughout the approximately 15-min flight test. The test was manually terminated while the battery remained above the selected low-voltage limit; therefore, the battery was not depleted during testing. The recorded duration represents a demonstrated flight time of at least 15 min under the evaluated conditions rather than the aircraft's maximum endurance. Because the test ended before the low-voltage limit was reached, the UAV retained sufficient battery capacity to continue operating beyond the test period. Figure 44 depicts the assembled UAV operating in indoor and outdoor environments.

The demonstrated 15-min flight-test duration was subsequently compared with the calculated hover endurance for the proposed 6S lithium-polymer battery configuration, which has a nominal voltage of 22.2 V and a rated capacity of 10,000 mAh. Unlike the flight-test duration, the calculated value estimates how long the UAV could theoretically remain in hover when using the proposed battery configuration. The tested and proposed operating conditions are summarized in Table 15.

Table 15: Measured and proposed flight results

Case	Battery specification	Result classification	Flight time
Measured test	4S, 14.8 V, 6.2 Ah, 100C	Demonstrated minimum	Approx. 15 min
Proposed model	6S, 22.2 V, 10.0 Ah, 15C	Theoretical hover estimate	28.1 min

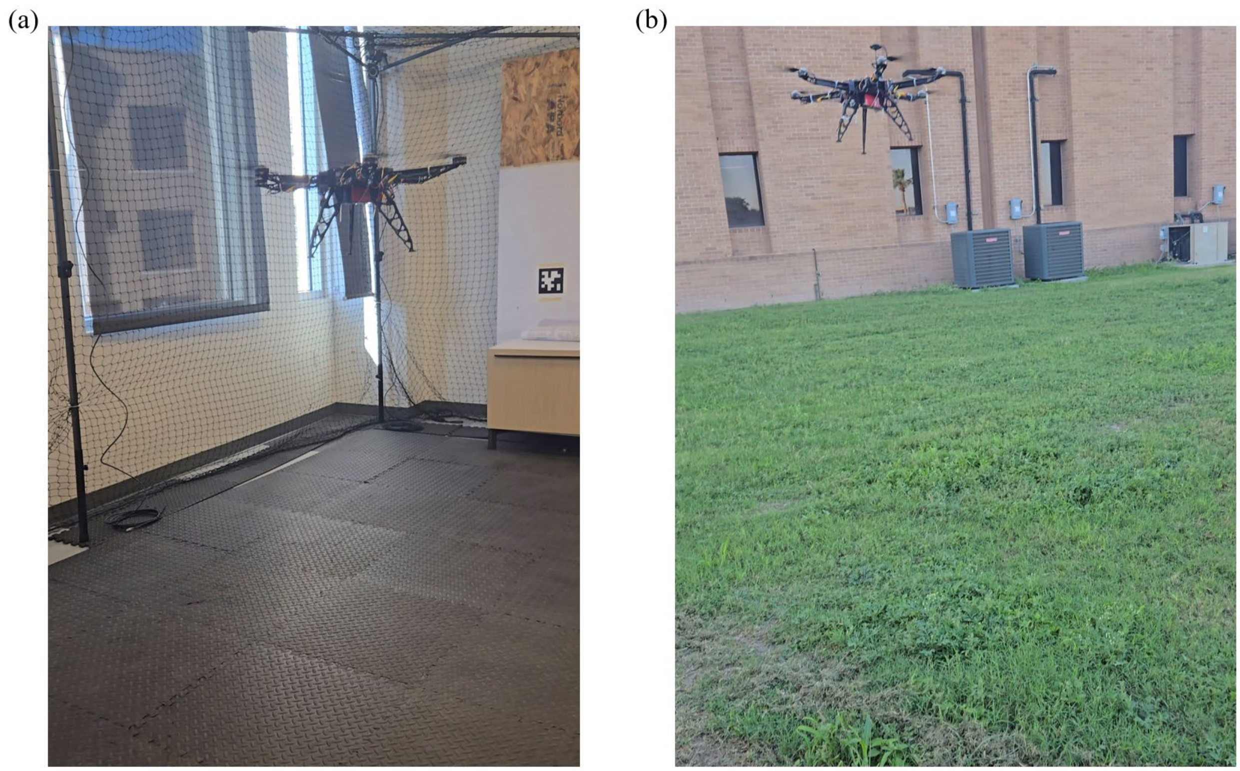

Figure 44: UAV in flight in a controlled indoor (a) and outdoor (b) environment

The theoretical endurance of the proposed battery configuration was estimated from the propulsion current required to maintain steady hover. For the baseline UAV mass of 3.814 kg, the six motors were assumed to share the required thrust equally, resulting in a required thrust of approximately 635.7 g per motor.

The measured EOLO CN 13 × 5 propulsion data included operating points of 600 g at 2.60 A and 700 g at 3.30 A. Because the required hover thrust of 635.7 g lies between these values, linear interpolation was used to estimate a current draw of approximately 2.85 A per motor. The corresponding total propulsion current for six motors was approximately 17.10 A.

An 80% usable-capacity limit was applied to the proposed 10.0 Ah battery to avoid assuming complete discharge during routine operation. This provided an estimated usable capacity of 8.0 Ah and, at the nominal battery voltage of 22.2 V, approximately 177.6 Wh of usable energy. Using the estimated hover current, the theoretical hover endurance was calculated as approximately 28.1 min. The values used in this calculation are summarized in Table 16.

Table 16: Calculation for theoretical hover-endurance estimate

Quantity	Value	Basis
UAV mass used in model	3.814 kg	Measured aircraft mass
Required thrust per motor	635.7 g	3.814 kgf divided among six motors
Interpolated current per motor	2.85 A	Linear interpolation between measured propulsion data between 600 g and 700 g
Total hover current	17.10 A	2.85 A × 6 motors
Rated battery capacity	10.0 Ah	Proposed battery
Usable capacity	8.0 Ah	80% of rated capacity
Nominal hover power	379.6 W	22.2 V × 17.10 A
Usable battery energy	177.6 Wh	22.2 V × 8.0 Ah
Estimated hover endurance	28.1 min	8.0 Ah / 17.10 A × 60

Because the theoretical endurance depends directly on the assumed usable battery capacity, additional estimates were calculated for usable capacities ranging from 70% to 100%, as shown in Table 17.

Table 17: Effect of usable battery capacity on theoretical hover endurance

Usable capacity	Available capacity (Ah)	Estimated endurance (min)	Interpretation
70%	7.0	24.6	More conservative usable-capacity limit
80%	8.0	28.1	Selected estimate
90%	9.0	31.6	Greater battery utilization
100%	10.0	35.1	Ideal theoretical upper bound

The 15C discharge rating of the proposed battery affects its current-delivery capability rather than its calculated endurance. For a 10.0 Ah battery, this rating corresponds to a theoretical maximum continuous current of 150 A. This value exceeds both the estimated hover current of 17.10 A and the maximum estimated propulsion current of 67.20 A, indicating that the stated battery discharge capability is sufficient for the calculated propulsion demand. However, the current capacities of the wiring, connectors, power-distribution system, ESCs, and motors must also be considered.

The estimated 28.1-min hover endurance should be interpreted as a theoretical value rather than an expected flight duration. The calculation assumes a 3.814 kg takeoff mass, an 80% usable battery capacity, and that the interpolated current of 2.85 A per motor is representative of operation with the proposed 6S battery. Additional power demands from avionics and sensors, as well as maneuvering, wind, battery-voltage variation, and other flight conditions, were not included. Therefore, full-duration flight testing is required to establish the actual endurance of the proposed configuration.

4.3 Generative Design Outcomes

Generative design was used to develop lightweight structural concepts for the UAV arms and landing gear. The generated outcomes were evaluated based on predicted mass, maximum von Mises stress, minimum FOS, maximum displacement, print orientation, and, when available, buckling FOS. Because the studies were conducted using different optimization criteria and FOS requirements, each outcome set was evaluated separately rather than compared directly across all studies.

The UAV-arm studies were based on the design space established in Chapter III, which defined the preserved mounting regions, obstacle geometry, loads, and structural constraints used by Fusion 360. The initial geometry served only as the allowable design space and was not a functional UAV arm; therefore, its mass was not used as a baseline for calculating mass reduction.

4.3.1 UAV-Arm Generative-Design Outcomes

The preliminary UAV-arm study used a minimum FOS requirement of 2 and evaluated PAHT-CF, PAHT, and an experimental PETG material definition at multiple additive-manufacturing orientations. The resulting outcomes 1 and 9 are shown in Figure 45 – the rest can be found in Appendix C; they are summarized in Table 18. Values identified as NR were not available in the recorded generative-design results.

(a)

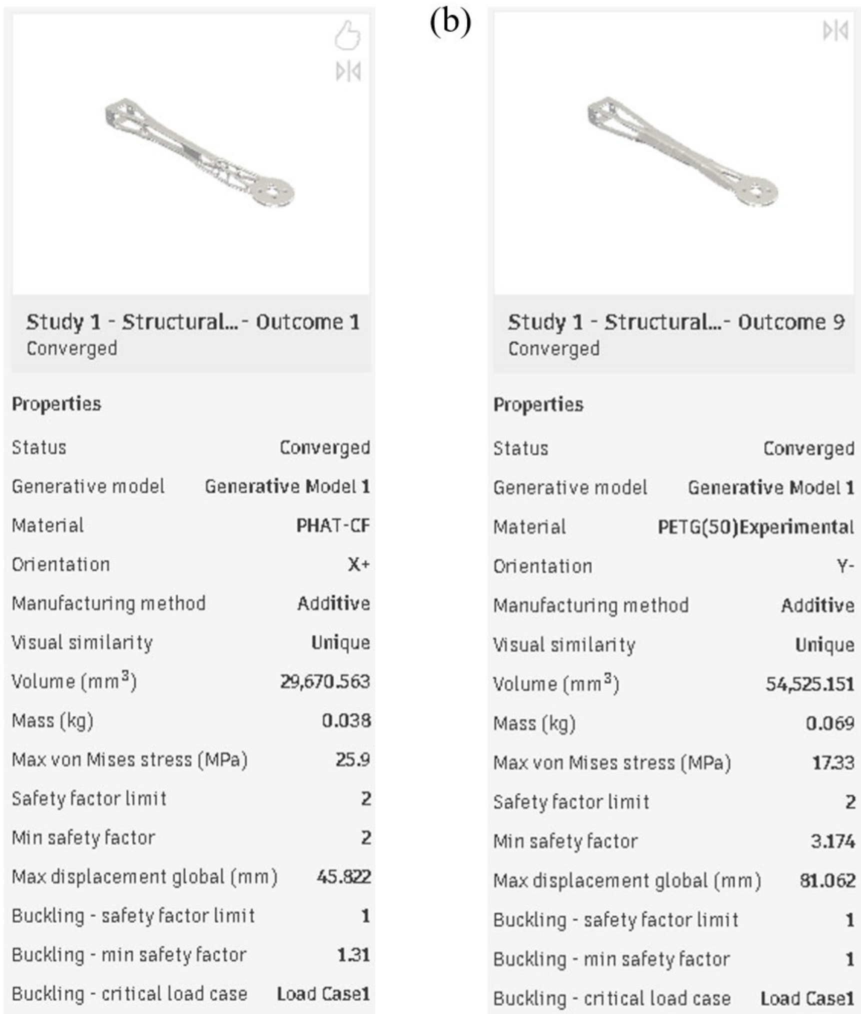

Figure 45: UAV-arm generative-design outcomes 1 and 9 for a minimum FOS of 2

Table 18: Generative-design results for UAV-arm outcomes using a FOS of 2

Outcome	Material	Orient.	Mass (g)	Stress (MPa)	Min. FOS	Disp. (mm)	Buckling FOS
1	PAHT-CF	X+	38	25.900	2.000	45.822	1.310
2	PAHT-CF	X−	38	25.900	2.000	NR	NR
3	PAHT-CF	Y−	58	19.574	2.646	54.184	1.000
4	PAHT	X+	28	30.698	1.792	NR	NR
5	PAHT	X−	30	27.500	2.000	31.513	1.603
6	PAHT	Y−	35	25.466	2.160	NR	NR
7	PETG exp.	X+	43	24.988	2.201	72.947	1.005
8	PETG exp.	X−	44	24.913	2.208	73.002	1.002
9	PETG exp.	Y−	69	17.330	3.174	81.062	1.000

The preliminary outcomes ranged in predicted mass from 28 to 69 g. Although Outcome 4 produced the lowest mass, its minimum FOS of 1.792 did not satisfy the specified requirement of 2. Among the outcomes with available displacement results, Outcome 5 produced the lowest maximum displacement at 31.513 mm. Several designs also exhibited buckling FOS near 1, indicating little predicted reserve against buckling. These results demonstrated that satisfying a stress-based FOS requirement alone did not necessarily produce a sufficiently stiff or buckling-resistant arm.

Based on the preliminary results, a refined study increased the minimum FOS requirement from 2 to 3. The resulting outcomes 1 and 7 are presented in Figure 46 and Table 19, additional resulting outcomes can be found in Appendix C.

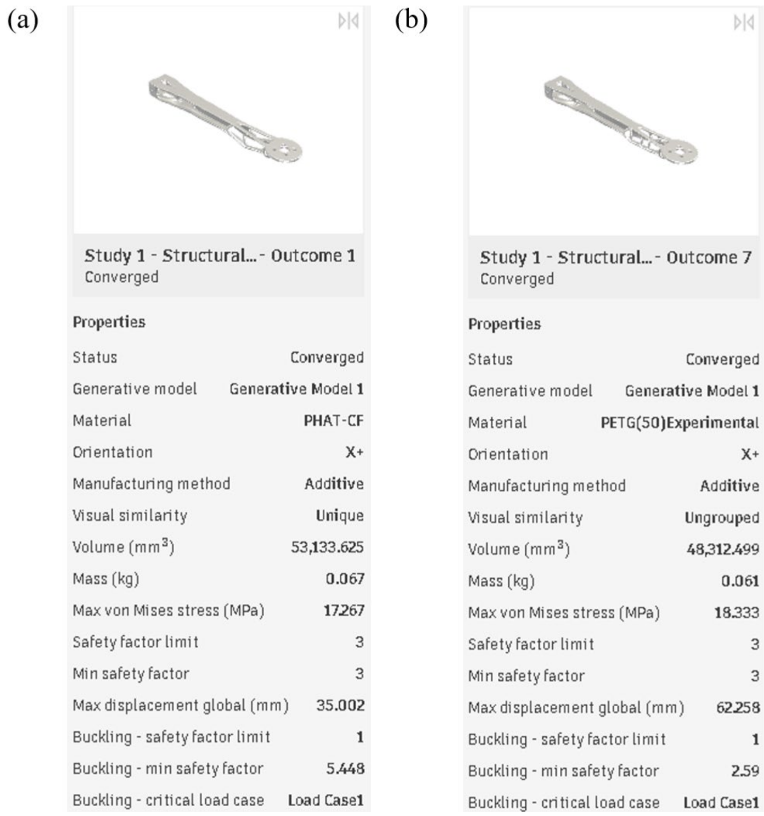

Figure 46: UAV-arm generative-design outcomes 1 and 7 for a minimum FOS of 3

Table 19: UAV-arm generative-design outcomes for a minimum FOS of 3

Outcome	Material	Orient.	Mass (g)	Stress (MPa)	Min. FOS	Disp. (mm)	Buckling FOS
1	PAHT-CF	X+	67	17.267	3.000	35.002	5.448
2	PAHT-CF	X−	67	17.267	3.000	34.945	5.562
3	PAHT-CF	Y−	70	17.027	3.042	46.393	1.799
4	PAHT	X+	51	18.333	3.000	23.799	6.658
5	PAHT	X−	51	18.333	3.000	23.723	6.773
6	PAHT	Y−	54	18.156	3.029	32.042	2.271
7	PETG exp.	X+	61	18.333	3.000	62.258	2.590

Increasing the FOS requirement generally produced heavier but stiffer geometries for comparable material and orientation combinations. For PAHT-CF in the X+ orientation, the predicted mass increased from 38 to 67 g, while maximum displacement decreased from 45.822 to 35.002 mm and the buckling FOS increased from 1.310 to 5.448. A similar trend was observed for PAHT in the X− orientation, where mass increased from 30 to 51 g, and displacement decreased from 31.513 to 23.723 mm. These results illustrate the trade-off between structural mass and stiffness as the design requirements became more restrictive.

Print orientation also influenced the generated geometry. The PAHT-CF X+ and X− outcomes produced nearly identical masses and structural responses, whereas the Y− outcome was slightly heavier, exhibited greater displacement, and had a substantially lower buckling FOS. A similar trend was observed for PAHT, for which the Y− orientation produced greater displacement and a lower buckling margin than the X-oriented outcomes.

An additional optimization study produced the three lightweight outcomes shown in Figure 47 and summarized in Table 20. These designs exhibited lower predicted masses and displacements than several outcomes from the preceding study; however, their buckling FOS were approximately 1.

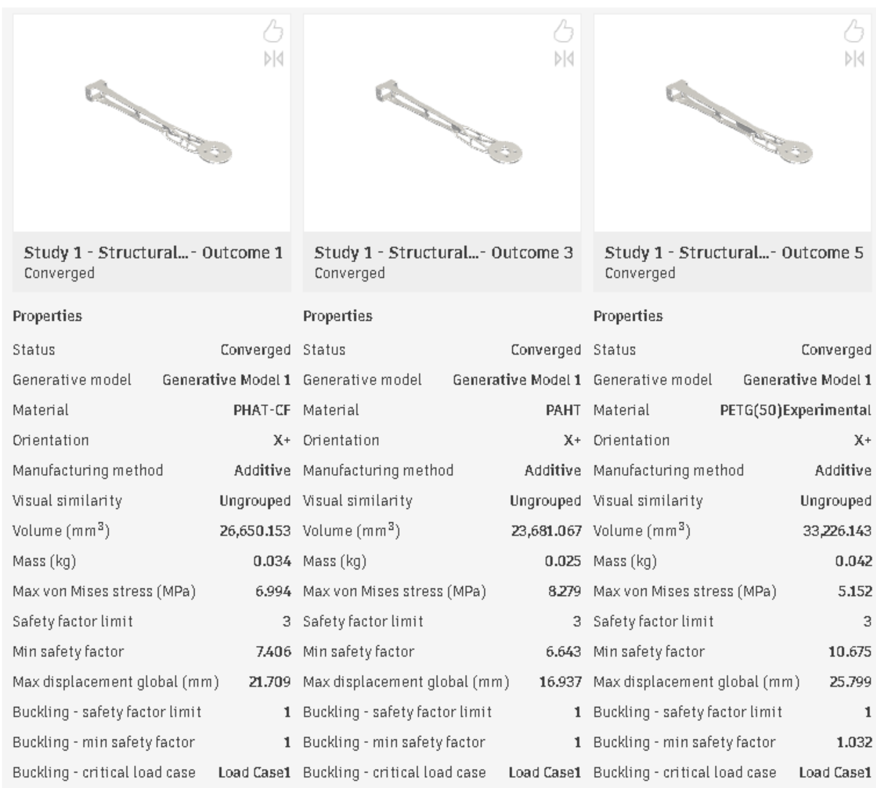

Figure 47: Additional UAV-arm outcomes using generative design

Table 20: Results for additional UAV-arm outcomes using generative design

Outcome	Material	Orient.	Mass (g)	Stress (MPa)	Min. FOS	Disp. (mm)	Buckling FOS
1	PAHT-CF	X+	34	6.994	7.406	21.709	1.000
3	PAHT	X+	25	8.279	6.643	16.937	1.000
5	PETG exp.	X+	42	5.152	10.675	25.799	1.032

The PAHT outcome produced the lowest predicted mass and displacement in this study, at 25 g and 16.937 mm, respectively, while the experimental PETG outcome produced the highest stress-based FOS at 10.675. Despite these favorable values, the PAHT-CF and PAHT outcomes both had buckling FOS of 1.000, while the PETG outcome provided only a slightly higher value of 1.032. Buckling therefore governed the acceptability of these lightweight designs and prevented their selection based solely on mass, stress, or displacement.

Because the optimization studies were performed under different design conditions, quantitative comparisons between outcome sets were limited to cases with equivalent loads, constraints, material properties, obstacle geometry, and manufacturing requirements. The studies were instead used progressively to identify the influence of material, print orientation, FOS requirement, and buckling constraints on the resulting arm geometry.

4.3.2 UAV Landing-Gear Generative-Design Outcomes

Generative design was also applied to the UAV landing gear using the experimental PETG material definition. Three converged additive-manufacturing outcomes were generated in the X+, Z+, and X− orientations, as shown in Figure 48 and summarized in Table 21. A minimum FOS of 5 was specified for these outcomes.

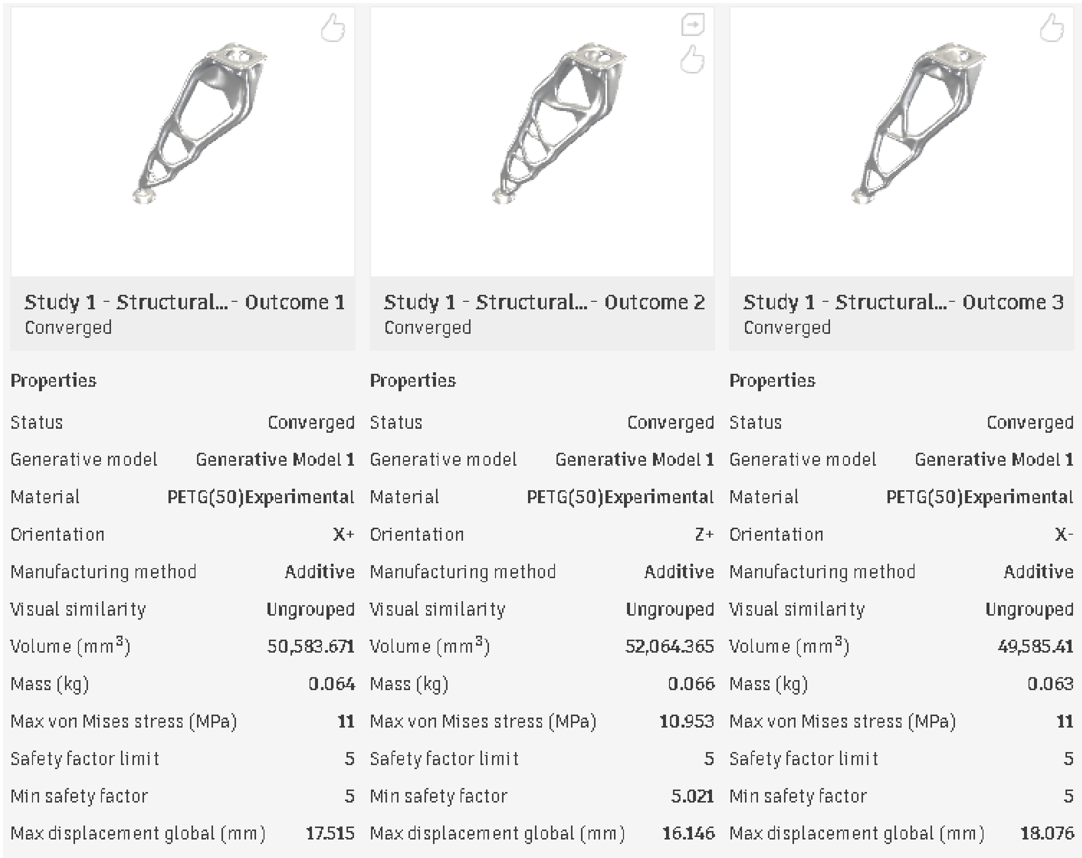

Figure 48: PETG landing gear generative-design outcomes for a minimum FOS of 5

Table 21: PETG landing gear generative-design outcomes for a minimum FOS of 5

Outcome	Material	Orient.	Mass (g)	Stress (MPa)	Min. FOS	Disp. (mm)	Buckling FOS
1	PETG exp.	X+	50,583.671	64	11.000	5.000	17.515
2	PETG exp.	Z+	52,064.365	66	10.953	5.021	16.146
3	PETG exp.	X−	49,585.410	63	11.000	5.000	18.076

All three landing-gear outcomes satisfied the specified FOS requirement and produced similar maximum stresses of approximately 11 MPa. The predicted masses ranged from 63 to 66 g, while maximum displacement ranged from 16.146 to 18.076 mm. The Z+ outcome produced the lowest displacement at 16.146 mm but had the highest mass at 66 g. In comparison, the X− outcome produced the lowest mass at 63 g but the highest displacement at 18.076 mm. These differences demonstrate a modest tradeoff between mass and stiffness among the evaluated print orientations.

Buckling results were not available for the landing-gear outcomes; therefore, the designs could not be compared on buckling resistance using the available generative-design results. Final selection also considered manufacturability, print orientation, mounting requirements, and the expected loading conditions of the landing gear.

Overall, the generative-design studies demonstrated the influence of material definition, print orientation, structural requirements, and buckling constraints on the geometry and predicted performance of the UAV components. Increasing the required FOS generally increased structural mass while improving stiffness and buckling resistance, whereas designs optimized primarily for low mass could provide insufficient buckling reserve. The generative-design results were therefore used to identify promising geometries rather than as final structural validation. The selected UAV-arm and landing-gear outcomes were subsequently evaluated through independent finite element analysis, as presented in the following section.

4.4 Finite Element Analysis Results

Following the generative-design outcome selection, the selected UAV-arm geometry was exported directly into Fusion 360 Simulation for static stress analysis. The geometry was not reconstructed or intentionally modified before analysis. Two material configurations were evaluated using the same arm geometry: experimental PETG at 50% infill and PAHT-CF at 20% infill. Both models used the same frame-attachment constraints, a 15 N vertical force applied at the motor mount, gravitational loading, and parabolic solid-element mesh settings. The material properties and principal FEA results are summarized in Table 22.

Table 22: Static FEA results for the selected UAV arm

Parameter	PETG 50%	PAHT-CF 20%
Material	Experimental PETG	PAHT-CF
Infill	50%	20%
Young's modulus	530 MPa	891 MPa
Yield strength	55.0 MPa	51.8 MPa
Applied motor force	15.00 N	15.00 N
Maximum von Mises stress	12.136 MPa	13.854 MPa
Minimum FOS	4.532	3.739
Maximum total displacement	12.989 mm	7.816 mm

4.4.1 PETG 50% Results

The PETG 50% model produced a maximum von Mises stress of 12.136 MPa, with the highest stress concentrated near the constrained frame-attachment region where the motor-induced bending load was transferred into the UAV frame, as shown in Figure 49. The maximum stress remained well below the assigned PETG yield strength of 55.0 MPa.

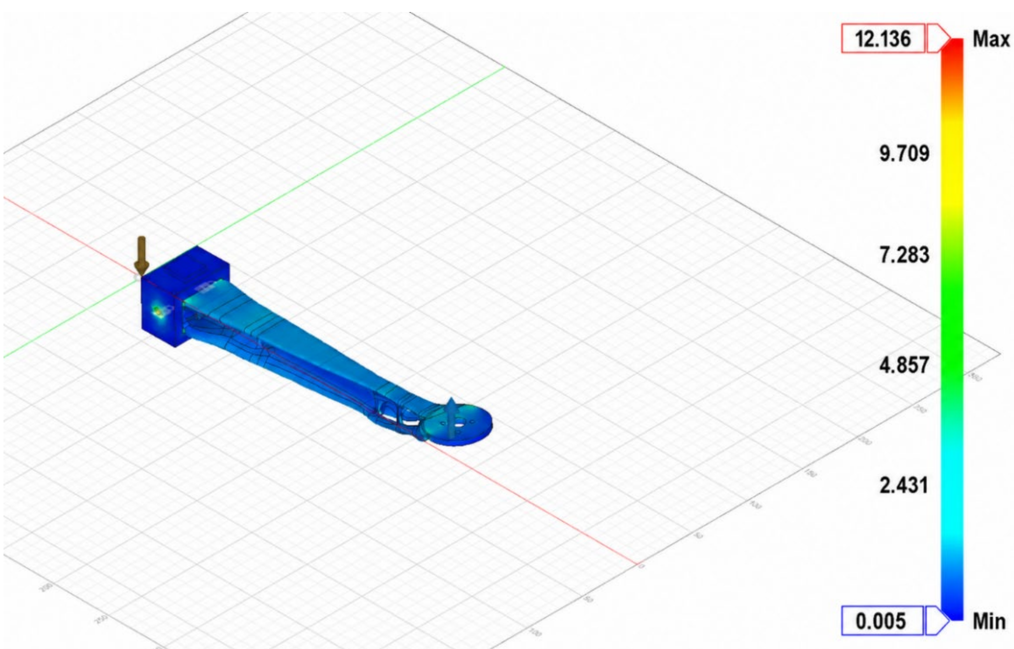

Figure 49: Von Mises stress distribution of the PETG 50% UAV arm under 15 N of thrust

The minimum FOS was 4.532, as can be seen in Figure 50, indicating that yielding was not predicted under the applied loading condition.

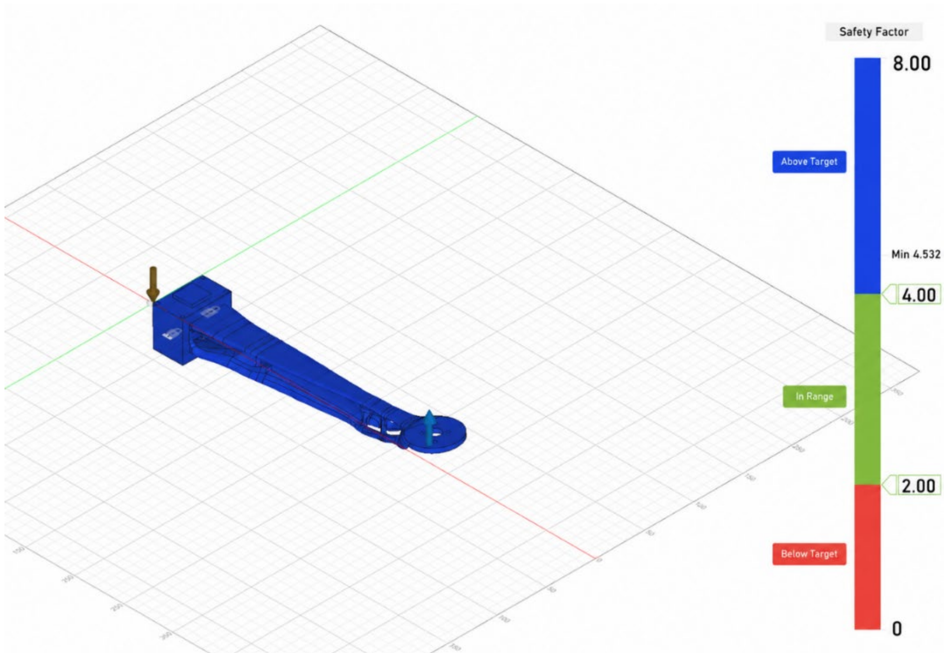

Figure 50: FOS distribution of the PETG 50% UAV arm under 15 N of thrust

Maximum total displacement was 12.989 mm and occurred at the motor-mount end of the arm, as shown in Figure 51. Displacement progressively increased from the constrained frame attachment toward the motor mount, consistent with the expected response of a cantilevered arm under bending. Although the stress and FOS results indicated adequate strength, the magnitude of the predicted displacement identified stiffness as an important consideration for this configuration.

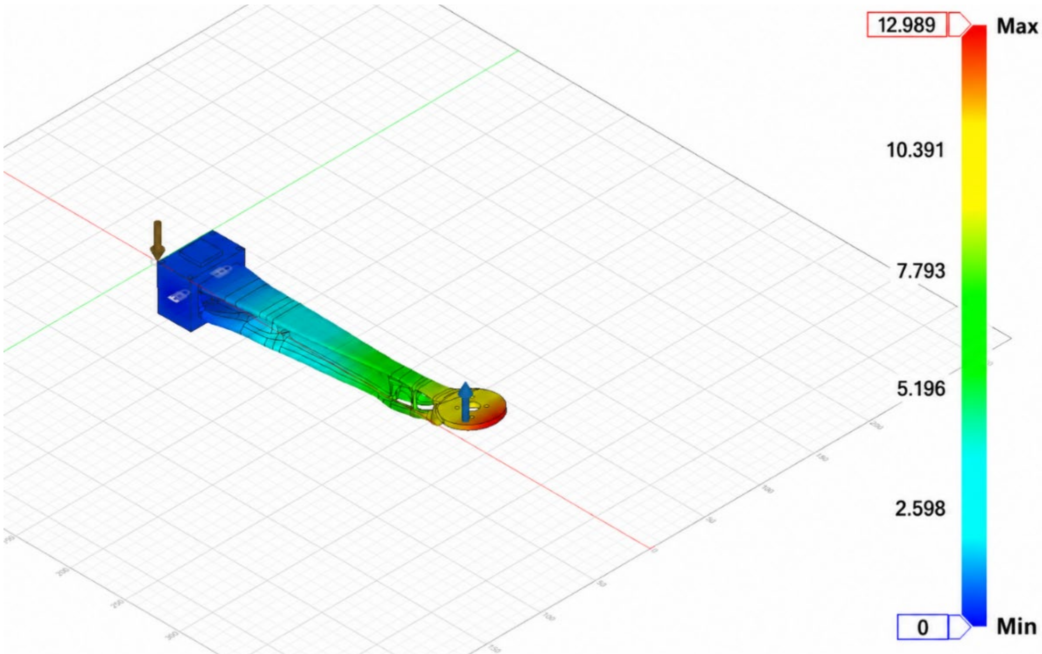

Figure 51: Total displacement distribution of the PETG 50% UAV arm under 15 N of thrust

4.4.2 PAHT-CF 20% Results

The PAHT-CF 20% model produced a maximum von Mises stress of 13.854 MPa, with the highest stress again concentrated near the frame-attachment region, as shown in Figure 52. This value remained below the assigned yield strength of 51.8 MPa.

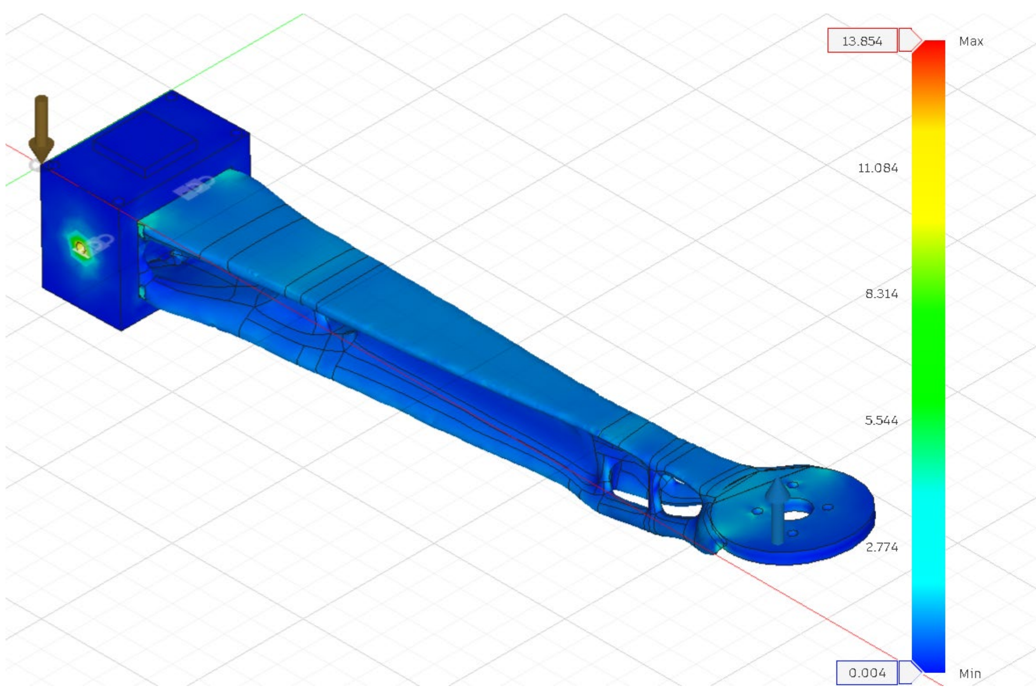

Figure 52: Von Mises stress distribution of the PAHT-CF 20% UAV arm under 15 N of thrust

The corresponding minimum FOS was 3.739, as shown in Figure 53. Although lower than that of the PETG configuration, the value remained greater than 3, and yielding was not predicted under the applied load.

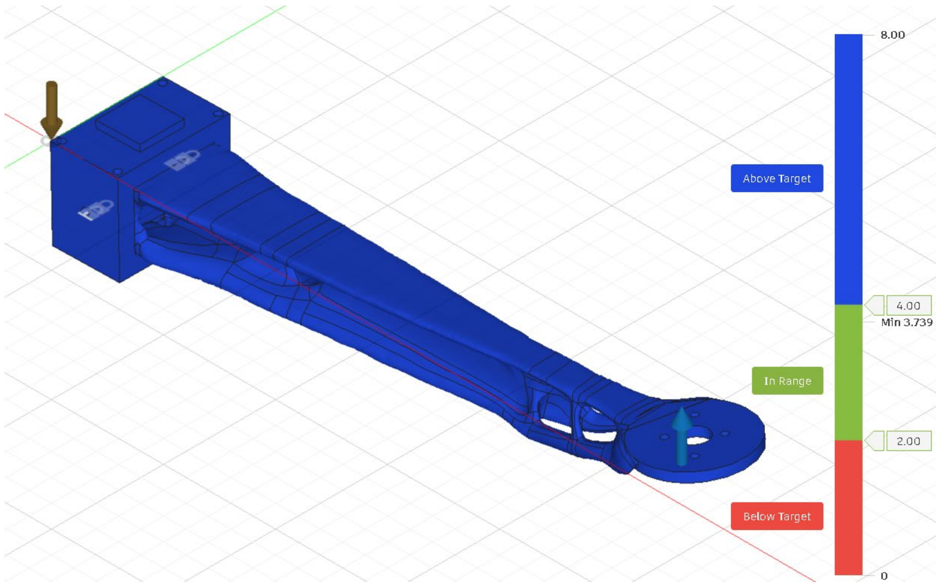

Figure 53: FOS distribution of the PAHT-CF 20% UAV arm under 15 N of thrust

Maximum total displacement was 7.816 mm and occurred at the motor-mount end of the arm, as shown in Figure 54. The displacement distribution followed the same general bending pattern observed for PETG but exhibited a substantially lower maximum value.

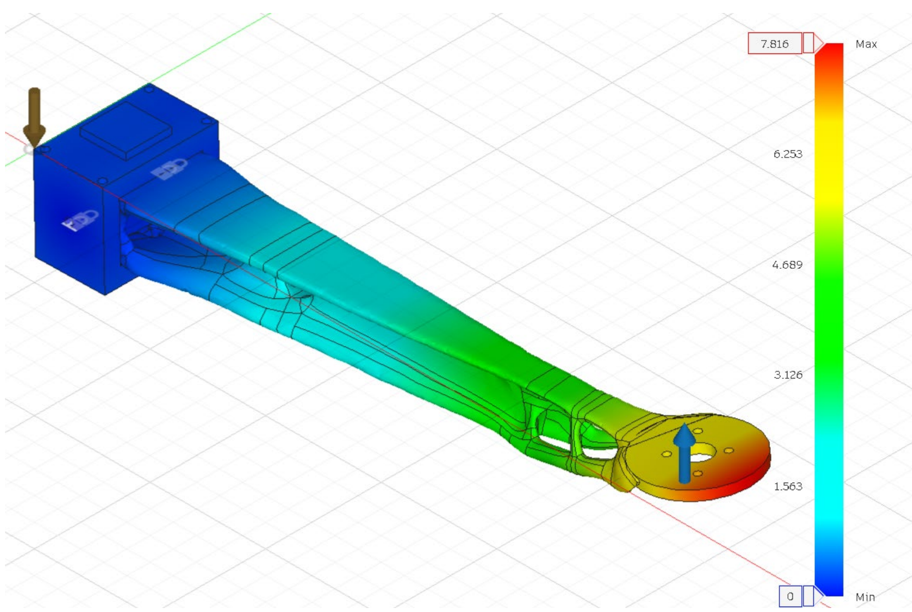

Figure 54: Total displacement distribution of the PAHT-CF 20% UAV arm under 15 N of thrust

4.4.3 Comparison of the FEA Results

Both material configurations satisfied the structural strength criterion under the applied 15 N motor load. PAHT-CF at 20% infill produced a 39.8% lower maximum displacement than PETG at 50% infill, despite its lower infill density. However, the PAHT-CF model exhibited a 14.2% higher maximum von Mises stress and a 17.5% lower minimum FOS. Nevertheless, both configurations remained below their assigned yield strengths and maintained minimum FOS greater than 3.

The lower displacement of the PAHT-CF configuration is consistent with its higher assigned elastic modulus of 891 MPa compared with 530 MPa for PETG. The results therefore indicate a trade-off between the two configurations: PETG provided the larger predicted FOS, whereas PAHT-CF provided greater structural stiffness at a substantially lower infill density.

The generative-design stage predicted a maximum displacement of 35.002 mm for the selected outcome, compared with 12.989 mm and 7.816 mm obtained from the subsequent PETG and PAHT-CF static analyses, respectively. Although the same exported geometry was used for the static analyses, the generative-design and FEA results were obtained from different analysis stages and should not be interpreted as directly equivalent displacement predictions.

Overall, the static FEA indicated that both material configurations could resist the modeled motor load without predicted yielding. PAHT-CF at 20% infill provided the lower predicted displacement, while PETG at 50% infill provided the greater FOS. The numerical displacement predictions were not directly validated through physical deflection measurements; therefore, they are used primarily to compare the relative structural response of the two material configurations.

4.5 Experimental Deflection Results

The displacement predictions presented in 4.4.1 and 4.4.2 were compared with physical measurements obtained from the manufactured PETG 50% and PAHT-CF 20% UAV arms under maximum-thrust loading. Arm deflection was measured using the laser-based system described in Chapter III and shown in Figure 15. The measured values were then compared with the maximum total displacements predicted by the corresponding static finite element analyses.

The PETG 50% arm exhibited a maximum measured deflection of approximately 8–10 mm, compared with an FEA prediction of 12.989 mm. The predicted displacement was therefore approximately 3.0–5.0 mm greater than the measured response. The PAHT-CF 20% arm exhibited a maximum measured deflection of approximately 6 mm, compared with a predicted displacement of 7.816 mm, corresponding to a difference of approximately 1.8 mm. The results are summarized in Table 23.

Table 23: Comparison of FEA-predicted and experimentally measured UAV-arm deflection

Arm configuration	FEA-predicted displacement (mm)	Laser-measured displacement (mm)	Difference (mm)
PETG 50%	12.989	8-10	3.0-5.0
PAHT-CF 20%	7.816	6	1.8

Although the FEA overpredicted the measured deflection for both configurations, the numerical and experimental results exhibited the same relative trend. PAHT-CF 20% produced less deflection than PETG 50% in both cases, indicating greater structural stiffness. The measured PETG deflection was approximately 23–38% lower than the predicted value, while the PAHT-CF measurement was approximately 23% lower.

Differences between the numerical and experimental results may be attributed to the idealized boundary conditions, material-property assumptions, representation of the internal infill, load application, and resolution of the experimental measurement system. Despite these limitations, the agreement in the relative response supports the use of the FEA models for comparing the stiffness of the PETG 50% and PAHT-CF 20% arm configurations.

4.6 UAV Flight Testing and Operational Validation

Following the component-level analyses and deflection measurements, the completed hexacopter was evaluated through operational flight testing with the generatively designed PETG 50% arms installed. Approximately five to six flights were conducted, consisting primarily of takeoff and hovering. The aircraft maintained stable flight, and no arm cracking, permanent deformation, connection failure, or other observable structural issues occurred during normal operation. Figure 55 illustrates the completed UAV during flight testing.

Figure 55: Hexacopter equipped with generatively designed PETG 50% arms during flight

During the testing program, the UAV also experienced several unintended crashes. The aircraft remained operational after at least three falls from estimated heights of 2–3 m and two falls from approximately 5 m, with no observed arm fracture following these events. The recorded flight and crash events are summarized in Table 24.

Table 24: Summary of UAV flight testing and unintended crash events

Operating event	Approximate count	Observed outcome
Hover and short flight tests	5-6 flights	No structural or flight issues were observed.
Unintended falls from 2-3 m	At least 3	The UAV remained operational; no arm fracture was observed.
Unintended falls from approximately 5 m	2	The UAV remained operational; no arm fracture was observed.
Subsequent unintended crash	1	One printed arm fractured and required replacement.

One PETG arm eventually fractured during a subsequent unintended crash after completion of the flight trials and survival of the earlier impacts, as shown in Figure 56. Because the arm was designed as a modular, additively manufactured component, the damaged arm could be replaced without replacing the motor, avionics, or central frame.

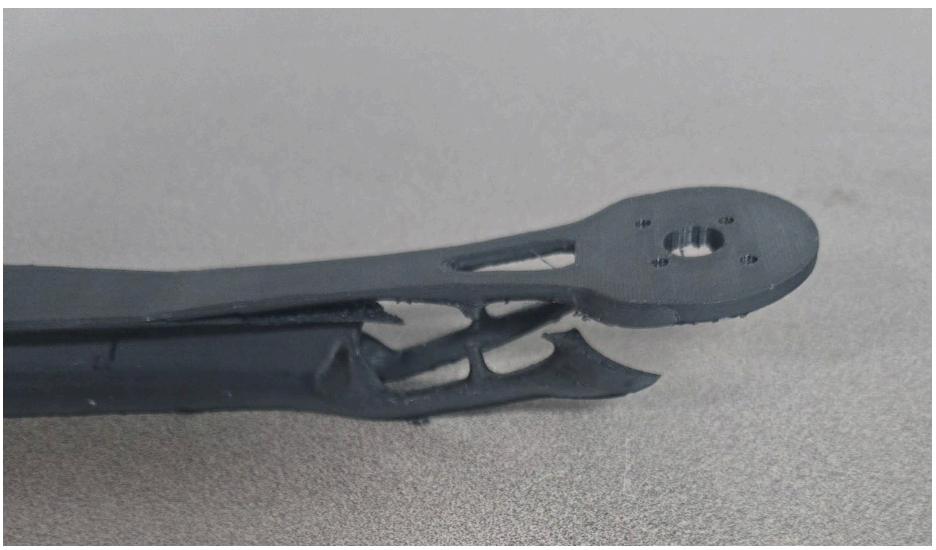

Figure 56: Fractured generatively designed PETG 50% UAV arm following an unintended crash

The unintended crashes were not controlled impact tests because the impact orientation, contact conditions, and drop heights were not instrumented. Therefore, these events cannot be used to quantify the impact strength or durability of the printed arms. However, the successful flight trials and continued operation following several unintended impacts provide qualitative evidence of the operational feasibility and replaceability of the generatively designed PETG arm.

4.7 Summary of Results

The experimental and numerical results demonstrated the feasibility of using additive manufacturing and generative design to produce lightweight, customizable structural components for the proposed hexacopter. Material characterization identified PAHT-CF as a favorable candidate because of its comparatively high strength and stiffness at low infill density. The generative-design studies further demonstrated that minimizing mass while satisfying a stress-based FOS was not sufficient to ensure acceptable structural performance; displacement, buckling resistance, printability, and component integration also influenced design selection.

Finite element analysis predicted that both PETG 50% and PAHT-CF 20% UAV arms would remain below their respective yield strengths under the modeled motor load, with minimum FOS greater than 3. PAHT-CF exhibited lower predicted and experimentally measured deflection, confirming its greater stiffness relative to PETG under the evaluated conditions. Although the FEA overpredicted the measured deflections, the numerical and experimental results produced the same relative trend, supporting the use of the models for comparative structural evaluation.

Operational testing further demonstrated that the generatively designed PETG arms could support the assembled hexacopter during takeoff and hovering without observable structural failure. The UAV also remained operational following several unintended impacts before one arm eventually fractured during a subsequent crash. Although these events were not controlled impact tests, they demonstrated the practical advantage of a modular additively manufactured structure in which a damaged arm could be readily replaced.

Overall, PAHT-CF 20% provided the more favorable configuration when structural stiffness and reduced infill were prioritized, while PETG 50% provided a lower-cost alternative that successfully supported operational flight. Together, the material characterization, structural optimization, numerical analysis, experimental measurements, and flight testing support the feasibility of generatively designed FFF components for customizable UAV structures.

CHAPTER V

SUMMARY AND CONCLUSIONS

5.1 Principal Conclusions

The research presented in this thesis investigated whether generative design, experimentally characterized material properties, and material-extrusion additive manufacturing could be combined to produce functional structural components for a customizable hexacopter. Seven unreinforced thermoplastics and short-carbon-fiber-reinforced materials were evaluated. The study also included propulsion testing, generative design, finite element analysis, physical arm deflection measurements, and operational flight testing. Based on the completed work, the following conclusions can be drawn.

1. PAHT-CF provided the most favorable overall mechanical response among the materials investigated for the UAV structure. At 20% infill, PAHT-CF reached an ultimate tensile strength of approximately 47.3 MPa and an elastic modulus of approximately 1,230 MPa, which were the highest tensile values at the baseline infill condition. Its maximum nominal shear stress of 33.10 MPa exceeded the PETG value of 18.92 MPa by approximately 75%, while its apparent torsional shear modulus of approximately 599 MPa was about 215% greater than the PETG value of 190 MPa. Untreated PAHT-CF at 20% infill also reached a maximum recorded compressive stress of 32.74 MPa, exceeding the tested PLA and PETG specimens at 50% infill. These results identify PAHT-CF as the preferred material when strength, stiffness, torsional resistance, and low-infill construction are considered together.

2. The mechanical performance of the printed materials depended strongly on manufacturing conditions. Increasing infill density generally increased tensile stiffness, tensile strength, and compressive resistance, although the magnitude of the improvement varied by material. PAHT-CF tensile strength increased from approximately 47.3 MPa at 20% infill to 56.7 MPa at 60% infill, while its tensile modulus increased from approximately 1,230 to 1,490 MPa. Thermal treatment and print orientation also changed the PAHT-CF response. Annealing at 110ºC for 16 hours increased tensile strength by approximately 11% relative to the untreated condition, and selected thermal treatments improved compressive resistance by approximately 9-10%. Because orientation, temperature, treatment duration, and cooling method were not always held constant, these results establish useful trends rather than a single universal optimum processing condition.

3. The generative-design studies produced manufacturable arm and landing-leg concepts while preserving the required frame and motor attachment regions. The outcome comparisons demonstrated that a stress-based FOS target alone was not sufficient for selecting a UAV component. Several lightweight arm outcomes met their stress limits but retained high predicted displacement or buckling FOS near 1.0. Increasing the target FOS generally increased mass and improved stiffness or buckling reserve, confirming a tradeoff between structural mass and rigidity. The original arm model was a design-space template rather than a complete solid baseline; therefore, a percentage mass reduction relative to that template could not be established. The outcomes were instead used for relative comparison and geometry selection.

4. The separate finite element analyses predicted that both selected arm configurations would remain below their assigned yield strengths under the 15 N motor load. PETG 50% produced a maximum von Mises stress of 12.136 MPa, a minimum FOS of 4.532, and a maximum displacement of 12.989 mm. PAHT-CF 20% produced a maximum stress of 13.854 MPa, a minimum FOS of 3.739, and a maximum displacement of 7.816 mm. Although PAHT-CF had the lower FOS, both values remained greater than 3, and PAHT-CF reduced the predicted displacement by 39.8% relative to PETG. These results show that stiffness, rather than yielding, was the more restrictive response for the selected arm geometry.
5. The physical deflection measurements supported the relative stiffness trend predicted by the simulations. Under maximum-thrust operation, the PETG 50% arm deflected approximately 8-10 mm and the PAHT-CF 20% arm deflected approximately 6 mm. The finite element analyses conservatively overpredicted both measured responses but correctly identified PAHT-CF as the stiffer configuration. The numerical models can therefore support comparative material and design decisions, but their absolute displacement values should be interpreted in view of the idealized constraints, homogeneous material definitions, and simplified representation of the printed infill.
6. The EOLO CN 13 x 5 propeller was the only tested propulsion configuration that supplied the required thrust reserve for the 3.814 kg baseline aircraft. At the maximum tested operating point, each motor produced approximately 1,610 g of thrust, corresponding to an estimated total thrust of 9.66 kgf and a baseline thrust-to-weight ratio of 2.53. The estimated maximum propulsion current was 67.20 A for six motors. The aircraft completed approximately 15 minutes of flight using the tested 4S, 6,200 mAh

battery before the test was manually stopped, so this value represents a demonstrated minimum rather than maximum endurance. The calculated 28.1-minute hover endurance for a proposed 6S, 10,000 mAh battery remains a theoretical propulsion-only estimate that requires full-duration experimental verification.

7. The completed hexacopter demonstrated the operational feasibility of the printed structural system. The UAV completed approximately five to six flights, primarily takeoff and hovering, without observed arm cracking, permanent deformation, or connection failure during normal operation. It also remained operational after several unintended falls before one PETG arm fractured in a later crash. Although these events were not controlled impact tests, they showed that the printed structure tolerated multiple accidental impacts before arm failure. The fractured arm was a modular and comparatively inexpensive component that could be replaced without discarding the motors, avionics, or central frame.

Overall, the study demonstrates that experimentally informed generative design and material-extrusion additive manufacturing can produce functional structural components for a larger custom hexacopter. PAHT-CF 20% was the preferred arm material when stiffness and mechanical performance were prioritized, whereas PETG 50% remained a practical low-cost material that supported full-thrust operation and repeated flight. The work developed and component-level validated the UAV structure and established a propulsion configuration with sufficient thrust for the baseline aircraft. However, operation with the complete proposed inspection-sensor payload was not experimentally demonstrated and remains necessary before the system can be considered validated for its intended infrastructure-inspection mission.

5.2 Study Limitations

The experimental program was conducted in multiple stages, and not every material was tested under every infill density, orientation, annealing condition, or loading mode. Some comparisons therefore involved different manufacturing conditions, and the influence of an individual variable could not always be isolated. The compression Poisson's ratio values also represented overall specimen deformation after loading and may have included permanent deformation, barreling, and internal infill collapse; they should not be interpreted as intrinsic elastic constants.

The generative-design and finite element models used simplified material definitions and boundary conditions. The printed components were represented using effective material properties rather than a detailed orthotropic model of deposited roads, layer interfaces, shells, and internal infill. The static analyses did not reproduce motor vibration, repeated cyclic loading, fatigue, temperature changes, moisture exposure, or transient impact loading. Consequently, the simulations were most reliable for comparing the selected configurations under consistent assumptions rather than predicting every aspect of in-flight behavior.

The laser-deflection measurements were approximate, and the unintended crashes were not controlled experiments. Impact velocity, orientation, contact surface, and exact height were not instrumented. Flight testing was primarily limited to takeoff and hovering, and the demonstrated 15-minute duration did not continue to the selected battery cutoff. In addition, the complete 1.5-3 kg inspection payload and its thermal, gas, and crack-detection sensors were not evaluated during a representative inspection mission.

5.3 Recommendations for Future Work

1. Conduct a controlled material-testing program with additional replicates and identical infill, orientation, annealing, cooling, and environmental conditions. Statistical analysis should be used to quantify variability and separate the effects of each manufacturing parameter.
2. Develop orthotropic or anisotropic numerical material models based on the measured print directions, shell thickness, layer interfaces, and infill architecture. Mesh-convergence studies should be completed, and the static analyses should be expanded to include modal, vibration, transient, buckling, fatigue, and impact evaluations.
3. Refine the UAV arm near the frame attachment and open lattice regions to reduce motor-end deflection and improve buckling and impact resistance without adding unnecessary mass. The revised geometry should be evaluated using controlled full-thrust, torsional, cyclic, and drop tests before flight.
4. Instrument the UAV during flight with accelerometers, strain or displacement sensors, current monitoring, and battery-voltage logging. These measurements would allow the vibration environment, structural response, power consumption, and actual endurance to be compared directly with the analytical and bench-test predictions.
5. Integrate the intended thermal, gas, and crack-detection sensors and conduct progressively loaded flight tests using the proposed battery. Final validation should include hovering, maneuvering, outdoor wind disturbances, maximum safe payload determination, full-duration endurance testing, and a representative infrastructure-inspection mission.

REFERENCES

[1] H. I. McHenry and R. Reed, Fracture and Deformation, U.S. Department of Commerce: National Bureau of Standards, 1987.

[2] D. Gregory, "From a View to a Kill: Drones and Late Modern War," *Theory, Culture & Society,* vol. 28, no. 7-8, pp. 188-215, 2011.

[3] M. Idrissi, M. Salami and F. Annaz, "A Review of Quadrotor Unmanned Aerial Vehicles: Applications, Architectural Design and Control Algorithms," *Journal of Intelligent & Robotic Systems,* vol. 104, no. 2, p. 22, 2022.

[4] H. Kitonsa and S. V. Kruglikov, "Significance of Drone Technology for Achievement of the United Nations Sustainable Development Goals," *R-Economy,* vol. 4, no. 3, pp. 115-120, 2018.

[5] S. Ibrahim, B. Alkali, A. Oyewole, S. Bala Alhaji, A. A. Abdullahi and A. G. Ibrahim, "Structural Integrity Study for a Quadcopter Frame to Be Deployed for Pest Control," *EVERGREEN Joint Journal of Novel Carbon Resource Sciences & Green Asia Strategy,* vol. 8, no. 3, pp. 667-672, 2021.

[6] S. Barua, M. S. S. Tanjim, A. N. Oishi, S. C. Das, M. A. Basar and S. A. Rafi, "Design and Implementation of Fire Extinguishing Ball Thrower Quadcopter," in *2020 IEEE Region 10 Symposium (TENSYMP)*, Dhaka, Bangladesh, 2020.

[7] A. Mahmud, "Development of Collision Resilient Drone for Flying in Cluttered Environment," Master's thesis, West Virgina University, 2021.

[8] A. Borik, A. Kallangodan, W. Farhat, A. Abougharib, M. A. Jaradat, S. Mukhopadhyay and M. Abdel-Hafez, "Caged Quadrotor Drone for Inspection of Central HVAC Ducts," in *2019 Advances in Science and Engineering Technology International Conferences (ASET)*, Dubai, United Arab Emirates, 2019.

[9] B. Hardy, "Slipped through the Cracks: How Highway Authorities Missed the Flaw That Nearly Brought Down the I-40 Bridge," Arkansas Nonprofit News Network, 20 February 2022. [Online]. Available: https://arknews.org/index.php/2022/02/20/slipped-through-the-cracks-how-state-

highway-authorities-missed-the-defect-that-nearly-brought-down-the-i-40-bridge/. [Accessed 21 August 2026].

[10] M. A. Boon, A. P. Drijfhout and S. Tesfamichael, "Comparison of a Fixed-Wing and Multi-Rotor UAV for Environmental Mapping Applications: A Case Study," *The International Archives of the Photogrammetry, Remote Sensing and Spatial Information Sciences,* Vols. XLII-2/W6, pp. 47-54, 2017.

[11] V. Aswin Kumar, M. Sivaguru, B. Rohini Janaki, K. S. Sumanth Eswar, P. Kiran and R. Vijayanandh, "Structural Optimization of Frame of the Multi-Rotor Unmanned Aerial Vehicle through Computational Structural Analysis," *Journal of Physics: Conference Series,* vol. 1849, no. 1, p. 012004, 2021.

[12] J. Peksa and D. Mamchur, "A Review on the State of the Art in Copter Drones and Flight Control Systems," *Sensors,* vol. 24, no. 11, p. 3349, 2024.

[13] F. H. Wen, F. Y. Hsiao and J. K. Shiau, "Analysis and Management of Motor Failures of Hexacopter in Hover," *Actuators,* vol. 10, no. 3, p. 48, 2021.

[14] A. Balayan, R. Mallick, S. Dwivedi, S. Saxena, B. Haorongbam and A. Sharma, "Optimal Design of Quadcopter Chassis Using Generative Design and Lightweight Materials to Advance Precision Agriculture," *Machines,* vol. 12, no. 3, p. 187, 2024.

[15] A. Vedrtnam, P. Ghabezi, D. Gunwant, Y. Jiang, O. Sam-Daliri, N. Harrison, J. Goggins and W. Finnegan, "Mechanical Performance of 3D-Printed Continuous Fibre Onyx Composites for Drone Applications: An Experimental and Numerical Analysis," *Composites Part C: Open Access,* vol. 12, p. 100418, 2023.

[16] M.-R. Condruz, A. Paraschiv, T.-A. Badea, D. Useriu, T.-F. Frigioescu, G. Badea and G. Cican, "A Study on Mechanical Properties of Low-Cost Thermoplastic-Based Materials for Material Extrusion Additive Manufacturing," *Polymers,* vol. 15, no. 14, p. 2981, 2023.

[17] K. V. Wong and A. Hernandez, "A Review of Additive Manufacturing," *ISRN Mechanical Engineering,* vol. 2012, 2012.

[18] O. Abdulhameed, A. Al-Ahmari, W. Ameen and S. H. Mian, "Additive Manufacturing: Challenges, Trends, and Applications," *Advances in Mechanical Engineering,* vol. 11, no. 2, 2019.

[19] N. Shahrubudin, T. C. Lee and R. Ramlan, "An Overview on 3D Printing Technology: Technological, Materials, and Applications," *Procedia Manufacturing,* vol. 35, pp. 1286-1296, 2019.

[20] M. Raths, L. Bauer, A. Kuettner, S. Fischer and T. Laumer, "Gradual Error Detection Technique for Non-Destructive Assessment of Density and Tensile Strength in Fused Filament Fabrication Processes," *The International Journal of Advanced Manufacturing Technology,* vol. 131, no. 7-8, pp. 4149-4163, 2024.

[21] R. B. Kristiawan, F. Imaduddin, D. Ariawan, Ubaidillah and Z. Arifin, "A Review on the Fused Deposition Modeling (FDM) 3D Printing: Filament Processing, Materials, and Printing Parameters," *Open Engineering,* vol. 111, no. 1, pp. 639-649, 2021.

[22] M. K. Satra and S. Shetty, "Design Optimization and Manufacturing of Quadcopter Using 3D Printing," in *International Conference on Advances in Thermal Systems, Materials and Design Engineering (ATSMDE2017)*, Mumbai, India, 2017.

[23] L. Frizziero, A. Liverani, G. Donnici, E. Conti, B. Dello Preite, U. Lamanna, C. Leon-Cardenas and M. Garulli, "GD (Generative Design) Applied to a Plastics Recovery Drone (PRD) Using IDeS (Industrial Design Structure)," *Inventions,* vol. 6, no. 4, p. 82, 2021.

[24] S. Çaşka, K. Gök, M. Aydın and İ. Özdemir, "Finite Element Method Based Structural Analysis of Quadcopter UAV Chassis Produced with 3D Printer," *Journal of Science and Technology of Dumlupınar University,* no. 044, pp. 24-32, 2020.

[25] U. Sharma, V. Singh, B. Haorongbam, A. Sharma and R. Mallick, "Industry 4.0 and Advanced Manufacturing, Volume 2," in *International Conference on Industry 4.0 and Advanced Manufacturing (I-4AM 2024)*, Singapore, 2025.

[26] J. Bright, R. Suryaprakash, S. Akash and A. Giridharan, "Optimization of Quadcopter Frame Using Generative Design and Comparison with DJI F450 Drone Frame," *IOP Conference Series: Materials Science and Engineering,* vol. 1012, no. 1, p. 012019, 2021.

[27] B. Aman, "Generative Design for Performance Enhancement, Weight Reduction, and Its Industrial Implications," arXiv, 2020.

[28] B. Bay and M. Eryıldız, "Design and Analysis of a Topology-Optimized Quadcopter Drone Frame," *Gazi University Journal of Science Part C: Design and Technology,* vol. 12, no. 2, pp. 427-437, 2024.

[29] Y. L. Yap, W. Toh, A. Giam, F. R. Yong, K. I. Chan, J. W. S. Tay, S. S. Teong, R. Lin and T. Y. Ng, "Topology Optimization and 3D Printing of Micro-Drone: Numerical Design with Experimental Testing," *International Journal of Mechanical Sciences,* vol. 237, 2023.

[30] E. Natarajan, C. T. Ang, W. H. Lim, G. Kosalishkwaran, C. K. Ang and S. Parasuraman, "Design Topology Optimization and Kinematics of a Multi-Modal Quadcopter and

Quadruped," in *2019 IEEE Student Conference on Research and Development (SCOReD)*, Seri Iskandar, Malaysia, 2019.

[31] L. A. Al-Haddad, A. A. Jaber, W. Giernacki, Z. H. Khan, K. M. Ali, M. A. Tawafik and A. J. Humaidi, "Quadcopter Unmanned Aerial Vehicle Structural Design Using an Integrated Approach of Topology Optimization and Additive Manufacturing," *Designs,* vol. 8, no. 3, p. 58, 2024.

[32] Y. Sayyed, N. Patil, N. Solanki, B. Patil, S. Kale and N. Padawale, "Design and Development of Multipurpose Quadcopter Using Fused Deposition Modeling," in *2nd International Conference on Smart Sustainable Materials and Technologies (ICSSMT 2023)*, Cham, Switzerland, 2024.

[33] J. Chen, X. Liu, Y. Tian, W. Zhu, C. Yan, Y. Shi, L. B. Kong, H. J. Qi and K. Zhou, "3D-Printed Anisotropic Polymer Materials for Functional Applications," *Advanced Materials,* vol. 34, no. 5, p. 2102877, 2022.

[34] M. M. Prabhakar, A. K. Saravanan, A. Haiter Lenin, I. Jerin Leno, K. Mayandi and P. Sethu Ramalingam, "A Short Review on 3D Printing Methods, Process Parameters and Materials," *Materials Today: Proceedings,* vol. 45, pp. 6108-6114, 2021.

[35] J. Wu, "Study on Optimization of 3D Printing Parameters," *IOP Conference Series: Materials Science and Engineering,* vol. 392, no. 6, p. 062050, 2018.

[36] M. A. Pop, S. M. Zaharia, L. A. Chicos, C. Lancea, V. M. Stamate, G. R. Buican and I. S. Pascariu, "Effect of the Infill Patterns on the Mechanical Properties of the Carbon Fiber 3D Printed Parts," *IOP Conference Series: Materials Science and Engineering,* vol. 1235, no. 1, p. 012006, 2022.

[37] M. M. M. Haque, S. R. Dhrubo, A.-F. Z. Pranto, A. Ahmed, M. M. Arefin, M. Arifuzzaman and M. S. Islam, "Impact of Process Parameters and Material Selection on the Mechanical Performance of FDM 3D-Printed Components," *Hybrid Advances,* vol. 10, p. 100502, 2025.

[38] S. Valvez, P. N. B. Reis and J. A. M. Ferreira, "Effect of Annealing Treatment on Mechanical Properties of 3D-Printed Composites," *Journal of Materials Research and Technology,* vol. 23, pp. 2101-2115, 2023.

[39] W. Yu, X. Wang, X. Yin, E. Ferraris and J. Zhang, "The Effects of Thermal Annealing on the Performance of Material Extrusion 3D Printed Polymer Parts," *Materials & Design,* vol. 226, p. 111687, 2023.

[40] A. Szust and G. Adamski, "Using Thermal Annealing and Salt Remelting to Increase Tensile Properties of 3D FDM Prints," *Engineering Failure Analysis,* vol. 132, p. 105932, 2022.

[41] D. C. Wijnbergen, M. van der Stelt and L. M. Verhamme, "The Effect of Annealing on Deformation and Mechanical Strength of Tough PLA and Its Application in 3D Printed Prosthetic Sockets," *Rapid Prototyping Journal,* vol. 27, no. 11, pp. 81-89, 2021.

[42] S. Valvez, A. P. Silva, P. N. B. Reis and F. Berto, "Annealing Effect on Mechanical Properties of 3D Printed Composites," *Procedia Structural Integrity,* vol. 37, pp. 738-745, 2022.

[43] T. Šančić, M. Brčić, D. Kotarski and A. Łukaszewicz, "Experimental Characterization of Composite-Printed Materials for the Production of Multirotor UAV Airframe Parts," *Materials,* vol. 16, no. 14, p. 5060, 2023.

[44] Á. D. Virág, Z. Juhász, A. Kossa and K. Molnár, "Combining Oscillatory Shear Rheometry and Dynamic Mechanical Analysis to Obtain Wide-Frequency Master Curves," *Polymer,* vol. 295, p. 126742, 2024.

[45] PX4, "Pixhawk Wiring Quick Start," PX4, [Online]. Available: https://docs.px4.io/main/en/assembly/quick_start_pixhawk. [Accessed 12 August 2026].

[46] M. R. M. Asyraf, M. R. Ishak, S. M. Sapuan, N. Yidris and R. A. Ilyas, "Woods and Composites Cantilever Beam: A Comprehensive Review of Experimental and Numerical Creep Methodologies," *Journal of Materials Research and Technology,* vol. 9, no. 3, pp. 6759-6776, 2020.

[47] Y. Huang, X. Tian, W. Li, S. He, P. Zhao, H. Hu, Q. Jia and M. Luo, "3D Printing of Topologically Optimized Wing Spar with Continuous Carbon Fiber Reinforced Composites," *Composites Part B: Engineering,* vol. 272, p. 111166, 2024.

APPENDIX A

APPENDIX A

TESTING CODE AND RESULTS

```
#include "HX711.h"
#include <Servo.h>
const int LOADCELL_DOUT_PIN = 7;
const int LOADCELL_SCK_PIN = 6;
int ESCvalue = 1165;  // Start at actual minimum throttle
const int ESC_MIN = 1165;
const int ESC_MAX = 1815;  // Updated max throttle value 1730
const int FULL_THROTTLE_DURATION = 5000; // Hold max throttle for 5 seconds
HX711 scale;
Servo ESC;
void setup() {
    Serial.begin(115200);
    scale.begin(LOADCELL_DOUT_PIN, LOADCELL_SCK_PIN);
    ESC.attach(1, ESC_MIN, ESC_MAX);
    Serial.println("Initializing ESC...");
    // **ESC Arming Sequence**
    ESC.writeMicroseconds(ESC_MIN);
    delay(5000);
    Serial.println("ESC Ready!");
}
void loop() {
    if (ESCvalue < ESC_MAX) {
        // Increase throttle gradually
        ESC.writeMicroseconds(ESCvalue);
        Serial.print("ESC Signal: ");
        Serial.print(ESCvalue);
        Serial.print(" | Scale Reading: ");
        Serial.println(scale.read_average(5));
        ESCvalue += 25;
        delay(3000);
    }
    else {
        Serial.println("Max throttle reached. Holding for 5 seconds...");
        // Hold max throttle for 5 seconds
        ESC.writeMicroseconds(ESC_MAX);
        delay(FULL_THROTTLE_DURATION);
        // Stop the motor
        Serial.println("Stopping ESC.");
        ESC.writeMicroseconds(ESC_MIN);
        while (true); // Halt program permanently
    }
}
```

Figure 57: Arduino code for fatigue testing

Table 25: Compression tests conducted

Material	Infill (%)	Orientation	Annealing Time (hr)	Annealing Temp. (°C)	Cooling Method	Number of Samples (n)
PETG	50	90	None	None	SC	3
PETG	80	90	None	None	SC	3
PAHT-CF	20	0	None	None	SC	3
PAHT-CF	20	45	None	None	SC	3
PAHT-CF	20	60	None	None	SC	3
PAHT-CF	20	90	5	110	SC	3
PAHT-CF	20	90	12	90	QC	3
PAHT-CF	20	90	5	90	SC	5
PAHT-CF	20	90	None	None	SC	3
PAHT-CF	40	90	5	110	SC	3
PAHT-CF	40	90	5	90	SC	3
PLA	100	90	None	None	SC	3
PLA	50	90	None	None	SC	3
PLA	80	90	None	None	SC	3
PAHTCF	20	90	5	120	SC	3
PAHTCF	20	90	9	120	SC	3
PAHT-CF	20	90	5	60	SC	3
PAHT-CF	20	90	5	150	SC	3

Table 26: Tensile test conducted

Material	Infill (%)	Orientation	Annealing Time (hr)	Annealing Temp. (°C)	Cooling Method	Number of Samples (n)
PA6-CF	20-80	0	None	None	SC	5
PCTG	20-80	0	None	None	SC	5
PETG	20-100	0	None	None	SC	5
PETG-CF	10-90	0	None	None	SC	5
PAHT-CF	20	0	16	110	SC	3
PAHT-CF	20	0	16	90	SC	3
PAHT-CF	20	Side	None	None	SC	3
PAHT-CF	20	Top	None	None	SC	3
PAHT-CF	40	0	16	110	SC	3
PAHT-CF	40	0	16	90	SC	3
PLA-CF	10-100	0	None	None	SC	5

Table 27: Shear test conducted

Material	Infill (%)	Orientation	Annealing Time (hr)	Annealing Temp. (°C)	Cooling Method	Number of Samples (n)
PETG	50	0	None	None	SC	3
PAHT-CF	20	0	4	110	SC	3
PLA-CF	100	0	None	None	SC	3

```
#include <Stepper.h>

const int STEPS_PER_REV = 2048;
// 28BYJ-48 + ULN2003
Stepper myStepper(STEPS_PER_REV, 8, 10, 9, 11);
// Calibration:
// 200 motor steps = 6.8 mm of slider travel
const float STEPS_PER_MM = 200.0 / 6.8;
const int MOTOR_SPEED = 15; // RPM
void setup() {
  Serial.begin(9600);
  myStepper.setSpeed(MOTOR_SPEED);
  Serial.println("=== Slider Controller ===");
  Serial.println("Enter distance in mm.");
  Serial.println("Positive = UP");
  Serial.println("Negative = DOWN");
  Serial.println("Example: 10 or -5");
}
void loop() {
  if (Serial.available()) {
    float distanceMM = Serial.parseFloat();
    int stepsToMove = round(-distanceMM * STEPS_PER_MM);

    Serial.print("Moving ");
    Serial.print(distanceMM);
    Serial.print(" mm (");
    Serial.print(stepsToMove);
    Serial.println(" steps)");

    myStepper.step(stepsToMove);

    Serial.println("Done.");
  }
}
```

Figure 58: Laser deflection code

APPENDIX B

APPENDIX B

Specimen Technical Drawings

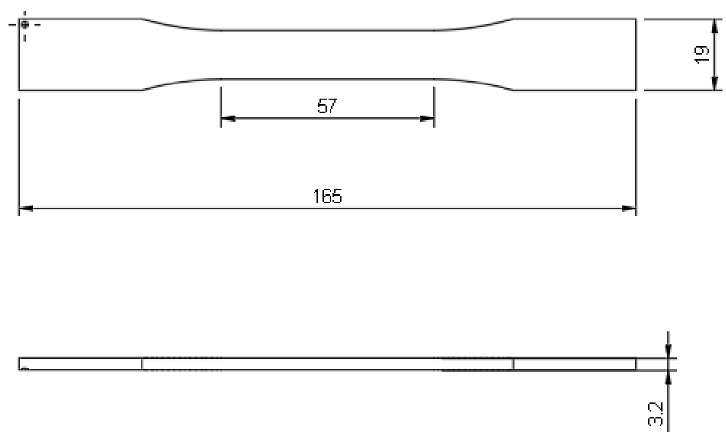

Figure 59: Tensile testing type I specimen technical drawing

(a) (b)

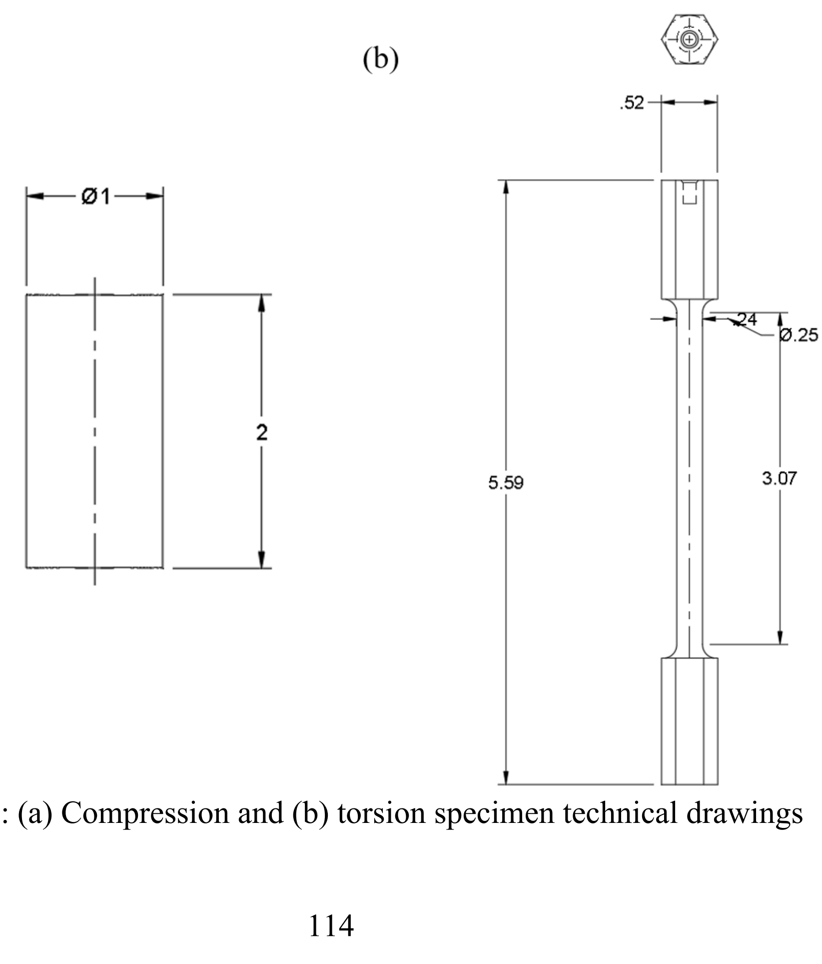

Figure 60: (a) Compression and (b) torsion specimen technical drawings

APPENDIX C

APPENDIX C

GENERATIVE DESIGN OUTCOMES

	Study 1 - Structural...- Outcome 1 (Converged)	Study 1 - Structural...- Outcome 3 (Converged)	Study 1 - Structural...- Outcome 5 (Converged)	Study 1 - Structural...- Outcome 7 (Converged)	Study 1 - Structura... - Outcome 8 (Converged)	Study 1 - Structural...- Outcome 9 (Converged)
Properties						
Status	Converged	Converged	Converged	Converged	Converged	Converged
Generative model	Generative Model 1	Generative Model 1	Generative Model 1	Generative Model 1	Generative Model 1	Generative Model 1
Material	PHAT-CF	PHAT-CF	PAHT	PETG(50)Experimental	PETG(50)Experimental	PETG(50)Experimental
Orientation	X+	Y-	X-	X+	X-	Y-
Manufacturing method	Additive	Additive	Additive	Additive	Additive	Additive
Visual similarity	Unique	Unique	Unique	Unique	Ungrouped	Unique
Volume (mm^3)	29,670.563	45,595.527	28,613.352	33,920.592	34,682.137	54,525.151
Mass (kg)	0.038	0.058	0.03	0.043	0.044	0.069
Max von Mises stress (MPa)	25.9	19.574	27.5	24.988	24.913	17.33
Safety factor limit	2	2	2	2	2	2
Min safety factor	2	2.646	2	2.201	2.208	3.174
Max displacement global (mm)	45.822	54.184	31.513	72.947	73.002	81.062
Buckling - safety factor limit	1	1	1	1	1	1
Buckling - min safety factor	1.31	1	1.603	1.005	1.002	1
Buckling - critical load case	Load Case1	Load Case1	Load Case1	Load Case1	Load Case1	Load Case1

Figure 61: UAV-arm generative-design outcomes for a minimum FOS of 2

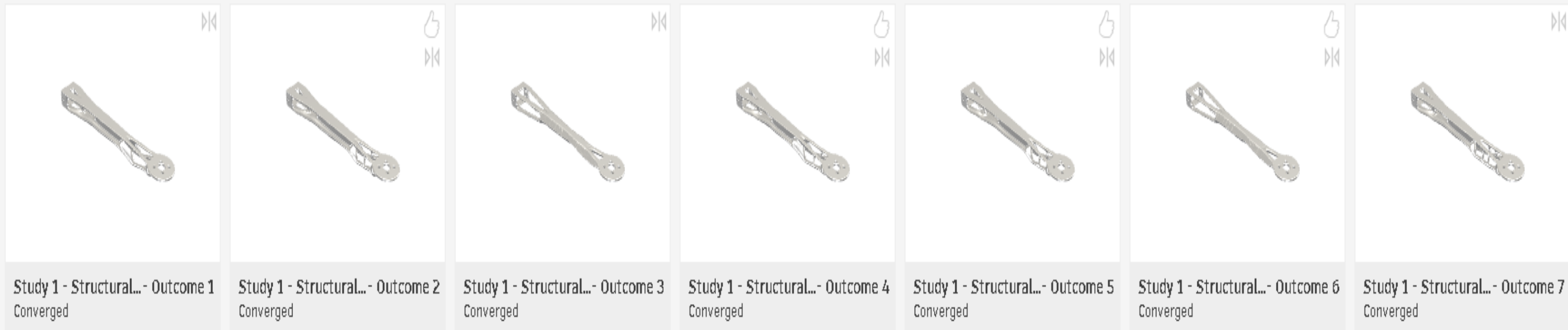

Properties	Outcome 1	Outcome 2	Outcome 3	Outcome 4	Outcome 5	Outcome 6	Outcome 7
Status	Converged	Converged	Converged	Converged	Converged	Converged	Converged
Generative model	Generative Model 1	Generative Model 1	Generative Model 1	Generative Model 1	Generative Model 1	Generative Model 1	Generative Model 1
Material	PHAT-CF	PHAT-CF	PHAT-CF	PAHT	PAHT	PAHT	PETG(50)Experimental
Orientation	X+	X-	Y-	X+	X-	Y-	X+
Manufacturing method	Additive	Additive	Additive	Additive	Additive	Additive	Additive
Visual similarity	Unique	Unique	Unique	Unique	Unique	Unique	Ungrouped
Volume (mm^3)	53,133.625	53,108.313	55,403.893	48,088.907	48,322.543	51,169.693	48,312.499
Mass (kg)	0.067	0.067	0.07	0.051	0.051	0.054	0.061
Max von Mises stress (MPa)	17.267	17.267	17.027	18.333	18.333	18.156	18.333
Safety factor limit	3	3	3	3	3	3	3
Min safety factor	3	3	3.042	3	3	3.029	3
Max displacement global (mm)	35.002	34.945	46.393	23.799	23.723	32.042	62.258
Buckling - safety factor limit	1	1	1	1	1	1	1
Buckling - min safety factor	5.448	5.562	1.799	6.658	6.773	2.271	2.59
Buckling - critical load case	Load Case1	Load Case1	Load Case1	Load Case1	Load Case1	Load Case1	Load Case1

Figure 62: UAV-arm generative-design outcomes for a minimum FOS of 3

VITA

Darren Espinoza attended the Science Academy of South Texas within the South Texas Independent School District and graduated in 2021. He attended The University of Texas Rio Grande Valley (UTRGV), where he received his Bachelor of Science in Mechanical Engineering in May 2024. Darren conducted research through the Center for Research Excellence in Science and Technology (CREST) from 2024 to 2026, focusing on additive manufacturing, material characterization, generative design, and the development of customizable unmanned aerial vehicle structures. He continued his studies at UTRGV and completed his Master of Science in Mechanical Engineering in 2026. Darren may be reached by email at DarrenEspinoza2717@gmail.com.